STUDIES OF CHROMOSPHERIC ACTIVITY OBSERVED IN Hα AND D_3.

Thesis by
Barry James LaBonte

In Partial Fulfillment of the Requirements
for the Degree of
Doctor of Philosophy

California Institute of Technology
Pasadena, California

1979

(Submitted June 23, 1978)

ACKNOWLEDGEMENTS

A thesis can be completed only with the support and encouragement of many people. It is my pleasure to thank here those whose help has made this work possible:

above all, my parents, William and Evelyn LaBonte;

my advisor, Harold Zirin;

the solar post-docs, Gordon Hurford, Ken Marsh and especially Ron Moore;

the staff of the solar group, Rich Goeden, Simon Groesz, Jeff Nenow, Frances Tang, Dave Thompson, and Ruth Weaver;

the staff at the Big Bear Solar Observatory, Alberta Altman, Jack Klemroth, Gene Longbrake, Mitch Nagao, Alan Patterson, and Owen Phairis;

former members of the solar group, Bill Adams, John Cowley, Jan Groesz, Peter Kupferman, Fred Mason, Gary Phillis, Dick Prout, and Juan Sanchez;

others in the solar physics community, Dick Canfield, Sara Martin, and Katsuo Tanaka;

the typists, Ruth, Alberta, and Barbara Moore;

and finally, under the philosophy that you are what you eat, Harry and Gary at the "Burger Continental".

To those people, and to others who have assisted in incidental ways, I offer my sincerest appreciation.

I also thank those organizations which have provided financial support for this work: the Air Force through contract F19628-76-C-055; the California Institute of Technology through a Graduate Research Assistantship; the National Aeronautics and Space Administration through grant NGR-05-002-034; and the National Science Foundation through a Graduate Traineeship and grants ATM74-13849 and ATM76-21132.

ABSTRACT

Several studies of chromospheric activity as observed in Hα and D_3 have been made. These are: Hα Observations of the August 12, 1975 Type III-RS Bursts (Solar Physics, 50, 201, 1976); A Measurement of the Helium D_3 Profile with a Birefringent Filter (Solar Physics, 53, 369, 1977); The Properties of Macrospicules Observed in Hα and D_3 (Big Bear Solar Observatory Preprint No. 0171); Polar Flares with D_3 Emission: November 15, 1974 (Big Bear Solar Observatory Preprint No. 0170); and Thick Target Models of Impulsive Chromospheric Flares (Big Bear Solar Observatory Preprint No. 0173).

TABLE OF CONTENTS

INTRODUCTION

Improvements in facilities and techniques at optical observatories in recent years have significantly increased the spatial and temporal resolution with which the solar chromosphere is observed. As a result, many details of the structure of the quiet sun, the evolution of active regions, and the generation of flares have been studied.

One example of the kind of work that can be done is the report in Chapter 1. The resolution and sensitivity of the optical data allow it to reveal the pattern of activity and suggest a physical model for the production of the observed anomolous radio bursts.

To obtain maximum sensitivity, the chromosphere is generally studied in Hα, as this line shows some response to virtually every phenomenon. This high sensitivity implies that Hα does not always discriminate between events. In the activity described in Chapter 1 for example, the differences between the events producing radio bursts and those not, although noticeable, were not great. If only the Hα data were available, it is not clear that a physically meaningful distinction between the groups of events would be made.

A complement to Hα is He I D_3. Because He I is the only abundant element with first excitation and ionization potentials much larger than hydrogen, its response in the chromosphere is unique. D_3 often is better able to

discriminate high energy phenomena than Hα.

Compared to Hα, relatively little work has been done with D_3, and it is useful to concentrate on some of the simpler questions. One is the state of the nonflare chromosphere. The D_3 line profile measurement in Chapter 2 confirms and extends other work showing large nonthermal gas motions, but at a lower altitude than previous measurements. This result has been verified by a Kitt Peak group, using the He I 10830 Å line.

The simplest type of activity is the macrospicule. Chapter 3 is a study of macrospicules as observed in Hα and D_3. The basic topics addressed are the optical appearance of macrospicules, the analysis of the optical data in terms of the physical conditions in macrospicules, and explanation of the differences between the optical and extreme ultraviolet properties. This is the first such analysis of the optical data, and D_3 is central to the results.

During the search for other D_3 activity, an event of a type completely different from macrospicules was discovered in the quiet sun. Chapter 4 describes a set of D_3 emission flares at the pole. This event is clearly much more energetic than macrospicule activity, and closely resembles impulsive D_3 flares seen in active regions. Its appearance at the pole makes it the most unusual event yet seen in D_3.

A popular idea for the mechanism producing impulsive

flares is that of chromospheric heating by nonthermal electron beams. It is valuable to study this idea in detail because it should apply to the impulsive events seen in D_3. In Chapter 5, this flare model is examined. As the test solution is necessarily a simplification of the real system, particular attention is given to its internal consistency. Any problems quickly indicate what improvements in the model are needed for future calculations.

Much more work will have to be done before D_3 can be reliably used as a diagnostic. Observations are particularly important as, regardless of the complexity of the analysis, the results obtained are only as good as the data. The present work does show, however, that the different behavior of D_3 is a strong asset in studying the chromosphere.

CHAPTER 1

Hα OBSERVATIONS OF THE AUGUST 12, 1975 TYPE III-RS BURSTS

Appears as BBSO Preprint No. 0155
in revised form as
Solar Physics, 50, 201, 1976.

ABSTRACT

We present Hα filtergram observations of a number of the Type III-RS (reverse slope) bursts that occurred on August 12, 1975. Solar radio emission was peculiar on that date in that a large number, and proportion, of the usually rare reverse slope bursts were observed (Tarnstrom and Zehntner, 1975). We show that the radio bursts coincide in time with a homologous set of Hα flares located at the limb-ward edge of spot group Mt. Wilson 19598. We propose a model in which the reverse slope bursts are the downward branches of U bursts, whose upward branches are hidden be-hind the coronal density enhancement over the spot group.

1. INTRODUCTION

Tarnstrom and Zehntner (1975), hereafter TZ, have called attention to the peculiar solar radio emission on August 12, 1975. In particular, they observed a large number and proportion of Type III-RS (reverse slope) bursts. We have studied the Hα filtergram movies taken at Big Bear Solar Observatory on August 12 and believe the combination of the Hα and radio data indicates a simple explanation for the preponderance of reverse slope bursts that day. Our argument is as follows: We consider each Type III-RS burst as the downward branch of a U burst whose upward branch is for some reason unobservable. From the Hα films we identify the sources of the Type III bursts as a series of flares at a satellite magnetic pole on the preceding edge of sunspot group Mt. Wilson 19598. We also identify a magnetic arch connecting the site of these flares with the following part of the group, which demonstrates a closed field structure necessary for a U burst. This spot group was at $\sim$45° W longitude on August 12, so our line of sight to the source of the Type III's lay through the coronal density enhancement over the group. Therefore the radio ray paths were reflected higher in the solar atmosphere on the preceding side of the group than on the following. The bursts were thus seen only with reverse slope because at a given frequency the plasma level, which is the site of the emission

at that frequency, was observable only on the following side of the group, where the electron stream was moving down in the atmosphere.

2. OBSERVATIONS

The first point is the identification of the reverse slope bursts as the downward branches of U bursts. TZ show that at least two of their events, 1102 and 1507 UT, were downward branches, unusual in being more intense than their corresponding upward branches. Three additional events, 1220, 1651, and 1713 UT, were identified as U bursts by the groups at Harvard and at Weissenau (Solar-Geophys. Data, 1975). Since TZ see those as purely reverse slope, they must also have more intense downward branches. We will demonstrate below that at least one reverse burst, 1508 UT, was produced by activity identical to that of the U bursts at 1507, 1651 and 1713. By extension we will consider that all the reverse slope bursts on August 12 were in fact downward branches of U bursts. Our problem is then to determine why the upward branches were weak or unobservable.

Observations at Big Bear on August 12 covered 1420 - 0020 UT. The data used for this study were taken with the 22 and 25 cm vacuum refractors. Numerous small flares and surges occurred in Mt. Wilson 19598 throughout the day, with most of the activity taking place at the locations marked in

Figure 1. A was a satellite magnetic pole near the preceding spots which produced a series of flares and surges, and is the site we identify as the source of the electron streams that produce the Type III bursts. Although present on August 11 and 13, A did not flare on those dates. B was an emerging flux region that appeared overnight and produced flares at 1445, 1625 and 2204 UT. C was a site among the following spots that produced nearly continuous slow surging.

Two series of events occurred at A. Events slightly to the north were at 1525, 1825, 2030, 2052, and 2310 UT. These were principally surge events, with flare brightening either absent or having a slow onset. The second series, slightly to the south, was at 1425, 1435, 1457, 1507, 1651 and 1713 UT. These events were flares in the chromosphere above the satellite pole, with surges following after, if at all. The 1425 and 1435 events were relatively slow, but the others had one or more (at 1507 and 1713) inpulsive flashes. It is this set of impulsive events that we can associate with the radio bursts. We now show the detailed correspondence.

The 1507 event had two flashes (Fig. 2). The initial brightening, from 1506:43 to 1507:15 matches the 1506.9 - 1507.2 radio event. This was followed by emission surges and then a second brightening at 1508:03 to 1508:23 that matches the 1508.2 - 1508.4 radio event. This second

brightening was evident in its extension onto the penumbra of the large preceding spot.

The 1651 event (Fig. 3) was the simplest. It consisted of a bright flash in two points at the satellite pole at 1605:50 - 1651:01, which matches the radio event of 1650.9 - 1651.1. No surge appeared at any time.

The 1713 event (Fig. 4) was the largest of the day at Location A. Initial brightening occurred at 1712:57. Brightening extended onto the penumbra of the large spot at 1713:41. Peak brilliance occurred at 1714:00. Emission surging followed this flare. The radio event covers 1713.0 - 1715.6; the part shown by TZ in Figure 1a of their paper corresponds to the time of the peak brilliance.

The correspondence of radio and Hα activity is not perfect. First, we observed an Hα event at 1457 with a location and character similar to those which produced bursts, yet no radio event was seen. This is not a serious problem since previous studies (Kuiper and Pasachoff, 1973; Kuiper, 1973) have shown that the high resolution of the Big Bear data permits detection of Hα activity which has no radio counterpart. Second, there was a radio burst at 1452.7 - 1452.9 for which there was no Hα activity at A. Figure 5 shows that at the time of the burst the only Hα activity is a rapid motion of emission material in an arch away from B. This was a part of the 1445 flare. If this activity did

produce the 1453 burst, it is not clear why that burst should be similar to those produced at A, i.e. reverse slope. This one burst thus is a serious problem to our model.

One requirement for a U burst is a closed magnetic field, so that the electron stream is returned to a region of higher density. Figure 6 shows a closed magnetic arch connecting the preceding field which surrounds A with the following spots. Shortly after the onset of the 2310 emission surge at A, a portion of an arch appeared at the following spots. As the event continued, a two-pronged absorption surge was produced, reaching maximum height at 2320. At 2323 an extension of the arch from the following spots suddenly appeared, and in projection reached nearly to the preceding spots. This long arch was also two-stranded, and the material in it was downflowing, toward the following spots. We interpret this event as bulk motion of the surge material from A along a pair of closed field lines to the following part of the group. This is probably not the exact path followed by the burst electrons, since from Figure 1 of TZ the half travel time is $\gtrsim$ 2.3 sec and at a velocity of c/3, the path length $\gtrsim$ 460,000 km. The observed arch appears to lie too low to be that long. It should be noted that we do not observe any Hα brightening in the following part of the group at the times of the radio bursts, which would correspond to the impact of the electron stream at the

footpoint of the closed field line.

3. THE MODEL

From our full disk photographs at $\sim$ 1700 UT we measure positions of the large preceding spot to be 9°N, 49°W, and the centroid of the following spots to be 11°N, 38°W. Our line of sight to A lies directly over the center of the group, through the coronal density enhancement produced by the region. Newkirk (1961) has shown that the radio ray paths over an active region are reflected higher on the limbward side of the active region than on the side nearer disk center. Since reflection occurs at the point of maximum electron density along the ray path, this implies that at a given frequency we cannot observe plasma level on the limbward side of the group. Using the radio data as a probe of the coronal density structure in Mt. Wilson 19598, we can demonstrate the effect for this particular active region.

From TZ we take the following properties of the bursts: high frequency cutoff $\sim$ 500 MHz; low frequency turnover $\lesssim$ 130 MHz; and half travel time $\gtrsim$ 2.3 sec, implying a total path length of $\gtrsim$ 460,000 km. We assume that the high frequency cutoff is caused by the collisional destruction of the electron stream at the corona-chromosphere transition zone. Thus 500 MHz corresponds to the plasma frequency at

the base of the corona at the ends of the closed field line. This is a minimum assumption on the density since the stream may degrade by some other mechanism before reaching the transition zone. The observation by TZ of Y bursts, which appear to show mirroring of the stream, indicates observationally that the stream may not always reach the transition zone. If we assume that the electron path has a roughly circular shape, we can use the total path length and the surface separation of the base points, $\sim$ 132,000 km, to solve for the height of the top of the path. Setting the plasma frequency at the top of the path to 130 MHz, we can then derive a density scale height which is $\sim$ 40,000 km. Using the base density and scale height we model the density structure over the region as

$$N_e(R,\Theta)=EXP\left(\frac{1.003-R}{.0571}\right)x\left[5.0x10^8+8.0x10^9\ EXP\left(-\left(\frac{\Theta-43.5}{5.5}\right)^2\right)\right] \quad (1)$$

where R is in units of a solar radius. The spherically symmetric term represents the quiet corona. Use of a Baumbach density law for the quiet corona term gives nearly identical results for the ray reflection over the active region.

Figure 7 shows the result of ray tracing calculations using the density model of Equation 1, ignoring magnetic fields. The ray reflection levels were determined for 100

and 300 MHz. Each level represents the deepest layer in the solar atmosphere from which radiation at the given frequency can propagate to earth. Because of the finite step size of the ray tracing program, the levels plotted are systematically too deep by $\sim$ 1/2 a step or $\sim$ 7,000 km. It is easily seen that the ray paths penetrate to the plasma level on the following side of the group, but not on the preceding side. Type III bursts produced by activity on the preceding side of the group therefore should not be observable as the electrons rise in the corona. The bursts will only be seen on the following side of the group, as the electrons move downward, producing a reverse slope burst.

There are several constraints which must be met for this model to apply. The observed bursts must be emitted at the fundamental frequency, not the second harmonic. Emission at the harmonic would not be blocked by the coronal density, and the upward branch of the U burst would be observed. Another condition is that the line of sight lay in the plane of the arch along which the burst electrons travel. Soft X-ray observations, for example Vaiana et al., (1973), show that in active regions the coronal density is larger in individual magnetic arches, with lower densities elsewhere. We are concerned with such a high density arch since the repeated flare and surge activity at location A must have deposited an excess of material into a few closed

field lines. If the arch was at an angle to the line of sight, the emission from the upward branch could be observed through the regions of lower density. The 2320 UT event indicated that we probably were in the plane of the arch. A related condition is that the corona above the spot group not be too inhomogeneous, lest scattering off the inhomogeneities direct some of the upward branch emission to Earth. The isolation and simple bipolar nature of the group, with activity limited to scales much smaller than the group, suggest that this condition was also met.

4. DISCUSSION

The basic idea of our model is that an RS burst is emitted as a U burst, but a region of higher density between the ends of the magnetic arch prevents observation of the upward branch. Since this model appears to explain the bursts of August 12, 1975, perhaps it can explain other RS bursts. The alternative model is that the bursts are emitted only with reverse slope, either because the electron stream is produced at high altitude and travels only downward, or some peculiar configuration of the fields or density inhibits emission during the upward passage. This last mechanism would be difficult to confirm observationally; if the electrons cannot excite plasma oscillations they probably cannot produce any other observable phenomena.

If the electrons are produced at high altitude, there are observational consequences. There should be some weak RS bursts with no Hα event. There should be some bursts in which the radio travel time between the near and far sides of an arch is large; these bursts would look like the inverse of a merging front event. Bursts associated with Hα flares will have one of two possible characteristics. If the flare is produced by the impact of the electrons on the chromosphere, there should be X-rays from thick target emission. If the flare is produced by a thermal mechanism, there should be two Hα ribbons separated by a distance comparable to the altitude, $\sim$ 100,000 km.

To further test these models observationally, we searched Solar Geophysical Data for the years of 1970 through 1974, and found 11 days with more than two Type III-RS bursts. Among these days and adjacent ones with bursts from the same spot groups, we have Hα data on 9 bursts, listed in Table 1. Four (4,6,7,9) are identical in character with the August 11 activity. Only two (3,5) have the scale or the X-ray emission predicted by the high altitude model. Thus we have seven more events which cannot be explained by alternative models. Although none of these events has as simple a geometry as those on August 12, it is not impossible to construct coronal models which produce similar blocking of upward branch emission.

5. SUMMARY

We believe that the unusual number and proportion of Type III-RS bursts observed on August 12, 1975 can be explained by a simple geometric configuration. We find that 4 of the 5 bursts for which there are Hα data coincide in time with impulsive flare brightenings at a satellite magnetic polarity on the preceding edge of Mt. Wilson 19598. We show that the preceding field surrounding the satellite pole is connected by closed field lines to the following field of the group, providing a necessary configuration for U bursts. Finally we show that the preceding side of these closed field lines was unobservable at meter wavelengths due to the coronal density enhancement over the group. Thus a radio burst would only be seen on the following side, as the electron stream moves downward in the corona travelling from the flare site, producing a reverse slope. We do note however that at least one RS burst, at 1453 UT, does not fit this model.

This research was supported by NASA under NGR 05 002 034, the National Science Foundation under ATM74-13849, and the Air Force under F19628-76-C-0055.

REFERENCES

Kuiper, T.: 1973, Solar Phys. 33, 461.

Kuiper, T. and Pasachoff, J.: 1973, Solar Phys. 28, 187.

Newkirk, G.: 1961, Ap.J. 133, 983.

Solar Geophysical Data, 374 Part I, p. 102, August 1975, U.S. Dept. of Commerce, Boulder, Colorado 80302.

Tarnstrom, G.L. and Zehntner, Ch.: 1975, Nature 258, 693.

Vaiana, G.J., Davis, J.M., Giaconni, R., Kreiger, A.S., Silk, J.K., Timothy, A.F., Zombeck, M.: 1973, Ap.J. 185, L47.

Table 1

TYPE III-RS BURSTS WITH Hα DATA

	Date	Time(UT)	Description
1	8/1/72	0146	Flash in arch at neutral line
2	"	2118	Similar to 1
3	10/25/72	1136	Large filament activation, X-rays
4	10/26/72	0957	Flare-surge at satellite pole
5	"	1254	Similar to 3
6	8/9/74	0850	Flare-surge at satellite pole
7	"	1003	Flare at satellite pole
8	"	1018	Small filament activation, surge
9	"	1148	Flare points at satellite pole

FIGURE CAPTIONS

Figure 1:

Mt. Wilson 19598 on August 12, 1975. West is left, south is up. Times given in UT. At the top the cross marks disk center. Note the basically bipolar nature of the spot group and its isolation on the disk. Locations marked in the bottom photograph are the sites of activity on August 12. Flares associated with the radio bursts occurred at A.

Figure 2:

Hα activity at 1507 and 1508 UT. Top sequence is Hα + .6 Å, lower sequence Hα line center. West is up. The 1507 radio event corresponds to the initial brightening at the flare site. The 1508 event matches a second brightening, which also extends onto the penumbra of the largest p spot.

Figure 3:

Hα activity at 1651 UT. At the time of the radio event there is an impulsive brightening at the satellite pole. No surge is produced.

Figure 4:

Hα activity at 1713 UT. Top sequence is Hα line center, lower sequence Hα + .6 Å. The radio event begins at the time of initial Hα brightening. As in the 1508

event, emission extends onto the penumbra of the largest p spot (1713:41). The portion of the radio event shown by Tarnstrom and Zehntner (1975) corresponds to the time of peak Hα intensity, 1714:00.

Figure 5:

Hα activity at 1453 UT. Arrow marks the arch of moving emission material. This is a part of the 1445 flare in the EFR at location B. Location A shows no rapid change at this time; only the slow decay of the 1435 event is in progress.

Figure 6:

Surge and arch structure at 2320 UT. West is up. The surge maximum is followed by the appearance of long arch connecting to the following spots. Note that both structures are double stranded.

Figure 7:

Coronal model of Mt. Wilson 19598. Density structure is given by Equation 1. Dotted lines are density contours; heavy dashed lines are radio reflection levels; light dashed lines schematically represents the closed field line along which the burst electrons travel.

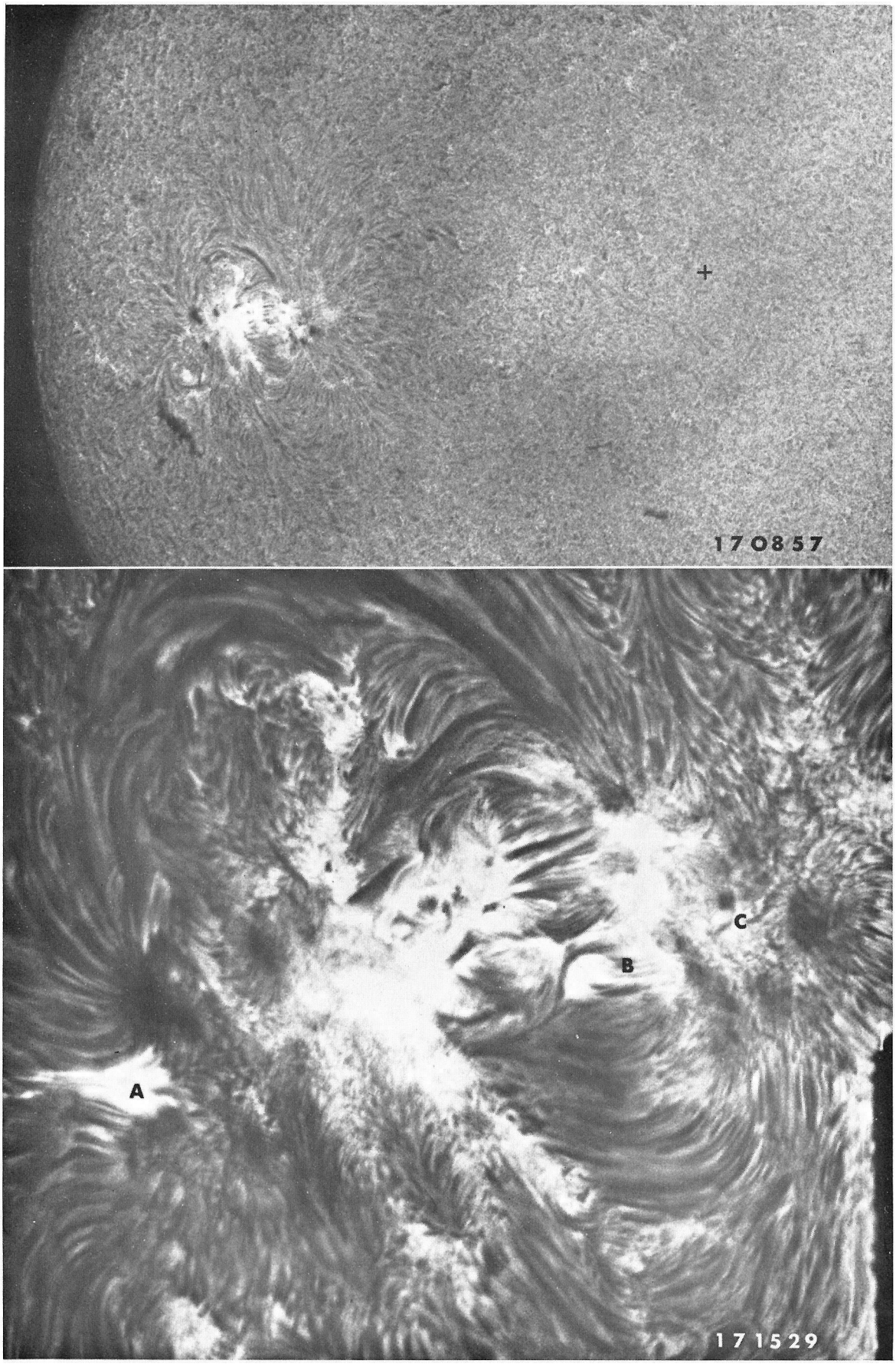

Figure 1

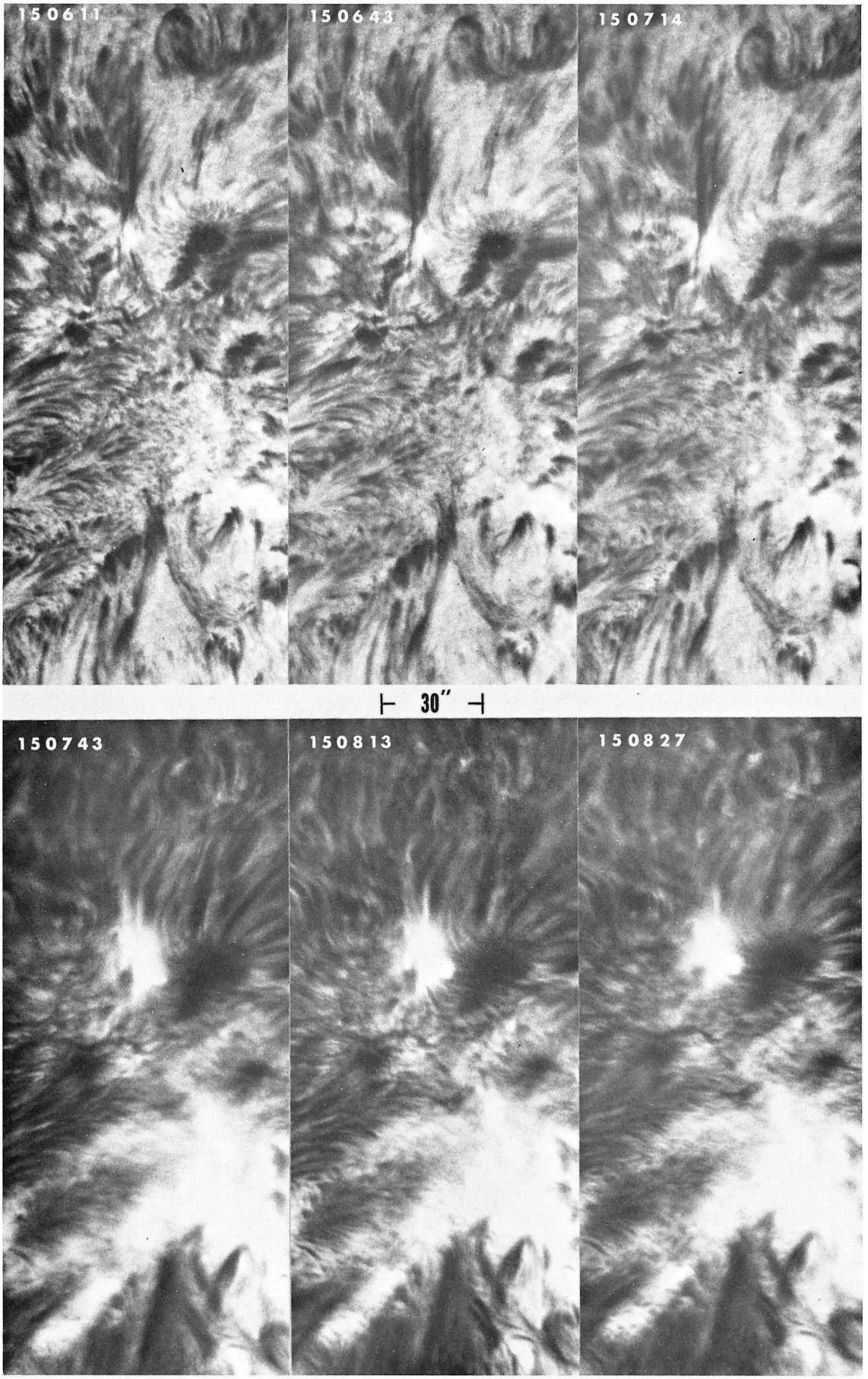

Figure 2

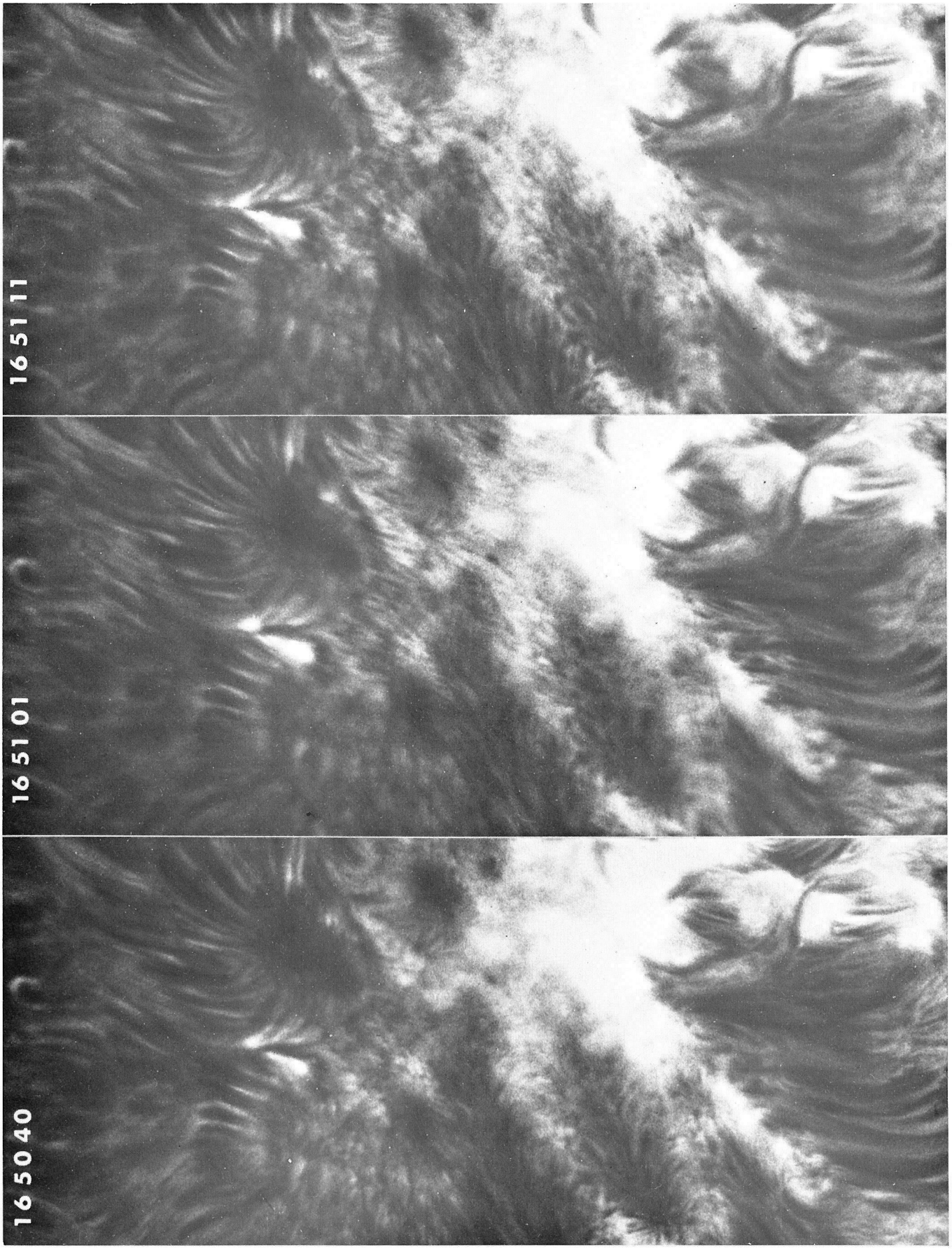

Figure 3

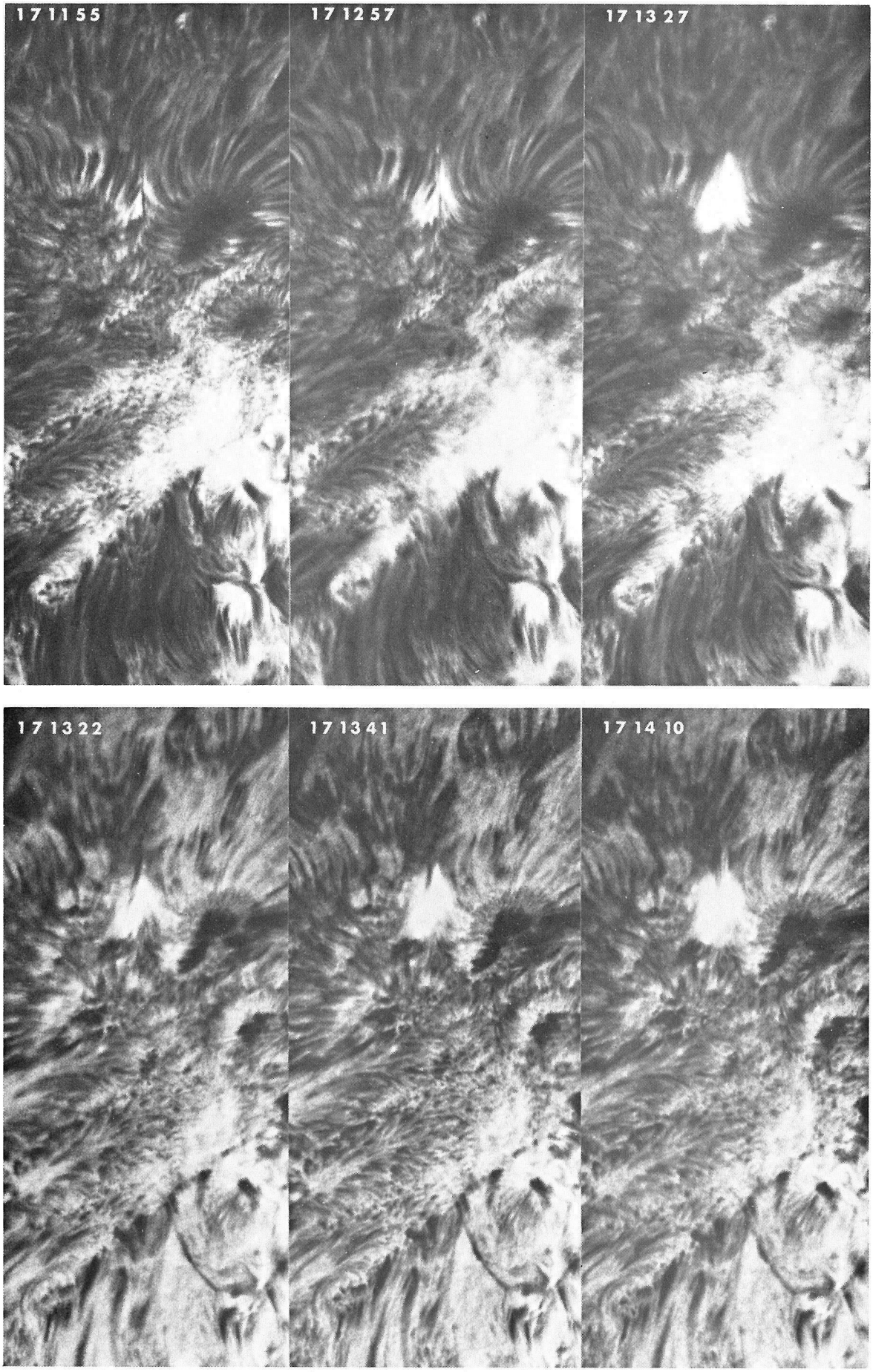

Figure 4

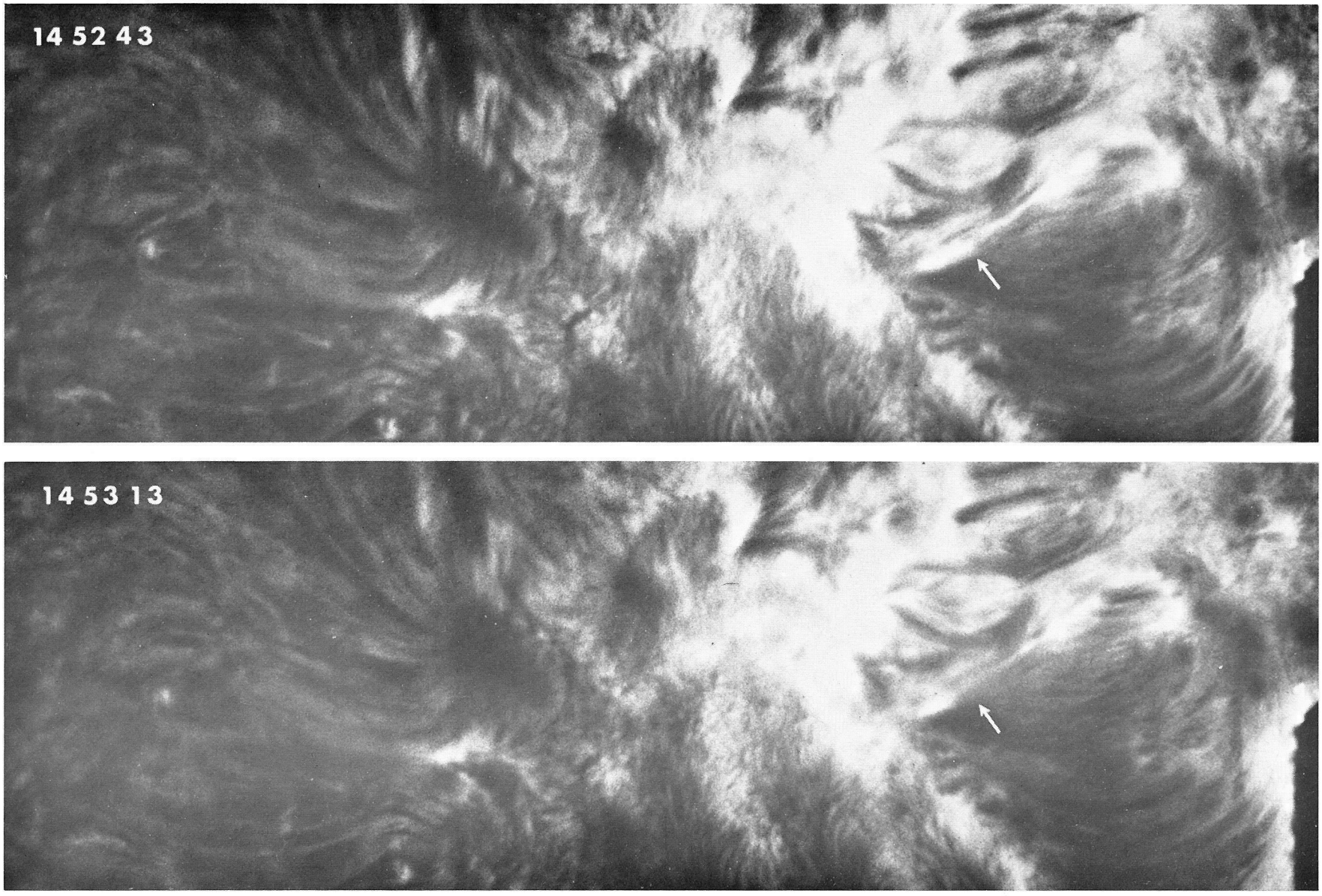

Figure 5

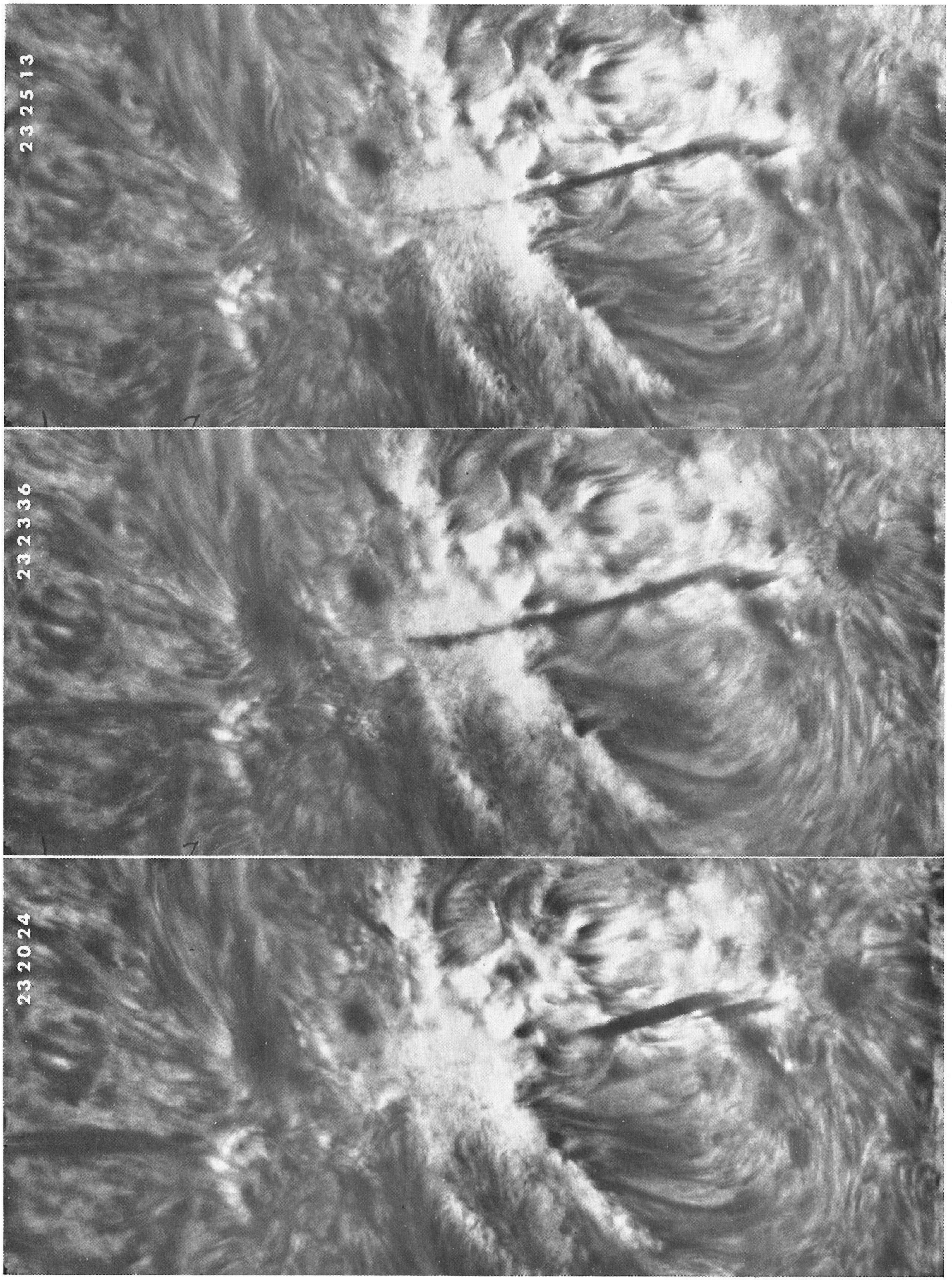

Figure 6

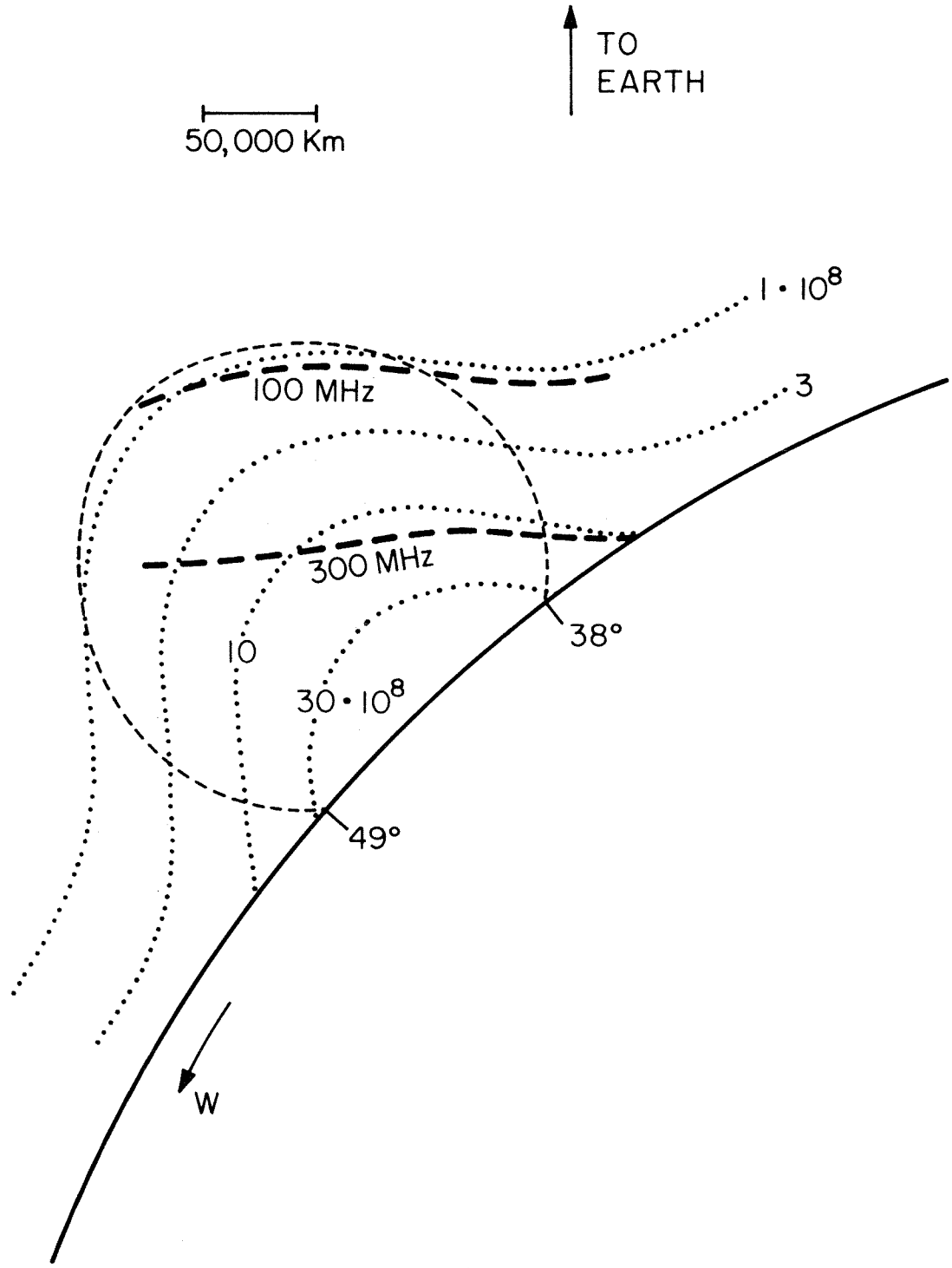

Figure 7

CHAPTER 2

A MEASUREMENT OF THE HELIUM D_3 PROFILE WITH A BIREFRINGENT FILTER

Appears as BBSO Preprint No. 0160
in revised form as
Solar Physics, 53, 369, 1977.

ABSTRACT

The D_3 line profile in plages on the disk is measured using a birefringent filter. The best fit Gaussian has a 1/e width of .4 Å, with negligible instrumental contribution. The D_3 opacity is produced in regions with thermal linewidth $\simeq$.1 Å; the much larger observed width indicates large non-thermal motions in the chromosphere.

1. INTRODUCTION

The He I D_3 line (5876Å) is an interesting and useful diagnostic of the regions above the temperature minimum in the solar atmosphere. There is no photospheric contribution to the line, so the correspondence of structures observed in D_3 to these higher layers is straightforward. D_3 is not only sensitive to chromospheric conditions, but to coronal conditions as well (Pope and Schoolman, 1975; Zirin, 1975).

A problem in using D_3 is its extreme weakness in the non-flare atmosphere. From the brightness of the D_3 limb band (White, 1963; Pope and Schoolman, 1975; Zirin, 1975) and the depth of the He I 10830 line (de Jager, Namba, Neven, 1966) one can estimate that the average depth of the quiet sun D_3 line must be $\lesssim .5\%$. For example, the observed limb band brightness, in units of the disk center continuum intensity, is $I_L \lesssim .2$. In the same units, the source function for D_3 is fixed by scattering of the photospheric radiation, at a value $S_{D_3} \simeq .4$, accounting for limb darkening. The line of sight optical depth in the limb band is

$$\tau_L = 2^{3/2} R_\odot^{1/2} T^{-1/2} \tau_V = 75\, T^{-1/2} \tau_V \ ,$$

where T is the band vertical thickness in Mm and is $\simeq 1$, and τ_V the average vertical optical depth. Inverting the transfer equation

$$I_L = S_{D_3} (1 - e^{-\tau_L})$$

gives a value $\tau_V \simeq .009$. For a weak line in pure scattering, the central depth is just $\tau_V/2$, or < .5%. Examination of the Liège Photometric Atlas (Delbouille, Roland, Neven, 1973) confirms the absence of a line in excess of this value.

Fortunately, D_3 is not uniformly produced across the disk, but shows enhanced absorption in individual structures, such as plages and filaments (Chapman, 1972). We take advantage of this structure by using a birefringent filter to provide the necessary spectral resolution. Since filtergrams display two spatial dimensions, we can measure the contrast profile of selected, individual, spatially resolved features with enhanced D_3, relative to the rest of the disk. For a very weak line, such contrast profiles will be identical with the actual profiles. In addition, sources of sytematic error, such as terrestrial absorption lines, are eliminated.

2. OBSERVATIONS

The data were taken at Big Bear Solar Observatory, using the Universal Birefringent Filter on the 65 cm vacuum reflector. We observed spot group Mount Wilson 19443 near the east limb on August 5, 1974 (Figure 1). Note in the D_3 frame (Figure 1b), the D_3 absorption features are

systematically limbward of their associated continuum faculae. This is a projection effect, caused by the altitude difference of the continuum photosphere and the D_3 chromospheric layer. This separation is seen most clearly at the limb in the cancelled frame (Figure 1c) where the D_3 layer is detached from the continuum limb.

A series of filtergrams were taken at .15 Å intervals through D_3, with additional frames in the continuum at 5872 Å. The total time required for the scan was 80 seconds. The filter bandpass has a FWHM of .19 Å at D_3. At each wavelength the single frame with highest spatial resolution was identified, and selected locations were measured; 17 in plages with D_3 absorption, and 15 in quiet areas for use as nulls. The measurements were made with a photometer in a projected image, permitting identification of the individual features. The D_3 central depth for the 17 locations ranged from 1.0 to 8.6%, corrected for the filter bandpass.

The individual profiles were normalized to unit depth and averaged, with weights given by their individual errors. The weighted mean depth is 5.0%. The normalized profile obtained is shown in Figure 2. Also shown is the best fit Gaussian, with 1/e width of .40 Å ($\pm$ .13 Å, 95% confidence limits). The correction to the linewidth to correct for the filter bandwidth would be only .01 Å, well below the accuracy of measurement. We also obtain a value for the line

center limb band brightness of $\lesssim .2$ of the disk center continuum brightness. Although we have a positive detection, calibration uncertainties allow us only to set an upper limit.

The only previous observation of the nonflare D_3 disk profile is that of Krat and Pravduke (1958). Their data give an average 1/e width of $.27 \pm .06$ Å from spectra of 10 plages. This value is within our error limits. It should be noted that Krat and Pravduke claim to observe a quiet sun D_3 depth of 1.1%, which is inconsistent with the more easily measured parameters we mentioned above. The source of this discrepancy is not clear. Confusion with terrestrial lines is the most probable error. Solar cycle variation of D_3 depth is not indicated; the limb band data referenced above were taken during periods of average sunspot number $R \simeq 35$, the 10830 data with $R \simeq 110$. The 10830 width from de Jager *et al.*, if scaled by λ, would imply a D_3 width of order .3 Å, comparable with these direct measurements.

3. DISCUSSION

The interesting property of the D_3 profile is that at the densities of the layers above the temperature minimum, the only important broadening mechanism is Doppler broadening. Interpreting the observed .4 Å width as thermal Doppler broadening, one derives a temperature of 1×10^5 K.

Calculations demonstrate (Zirin, 1975; LaBonte, in preparation) however, that the D_3 opacity is produced not by collisional mechanisms at high temperatures in the transition zone, but rather by radiative processes at lower temperatures in the chromosphere. The D_3 line is formed in regions with temperatures near 7000 K, and with thermal Doppler widths $\simeq .11$ Å. The much larger observed linewidth is therefore a direct measurement of the turbulent and oscillatory motions in the chromosphere. Using our observed width, and removing the filter and estimated thermal widths, we obtain a value of 19 km/sec for the non-thermal motions. The value from Krat and Pravduke is about 12 km/sec. These values are comparable with those obtained by Hirayama (1971) from eclipse data on helium lines at higher altitudes, where spicules would dominate the emission. Our value corresponds to the altitude of the limb band, 1700 $\pm$ 500 km above $\tau_{5000} = 1$. Judging from the low contrast of spicules in the limb band, most of its material is nonspicular.

Regarding the observing technique, the use of a birefringent filter to measure the D_3 profile is found to be quite successful, since we are interested in a narrow range of wavelengths, but a broad range of positions. The spectral resolution is more than adequate, and the ability to simultaneously record of order 10^4 to 10^5 separate spatial locations greatly speeds data collection. With improved

photometric analysis, both the accuracy and volume of data could be increased. Measurement of the individual profiles of each of the spatial resolved points would be possible, as well as much more accurate average profiles. Although the use of contrast profiles somewhat limits the detection threshold, one can go to progressively weaker features; for example, a quiet region can be measured by using a coronal hole as the null region.

This research was supported by NASA under NGR 05 002 034 and the Air Force under Contract F19628-76-C-0055.

REFERENCES

Chapman, G.A.: 1972, Solar Phys. 24, 288.

de Jager, C., Namba, O., Neven, L.: 1966, Bull. Astr. Inst. Neth. 18, 128.

Delbouille, L., Roland, G., Neven, L.: 1973, Photometric Atlas of the Solar Spectrum, λ3000 to 10000 Å, Liège.

Hirayama, T.: 1971, Solar Phys. 19, 384.

Krat, V.A. and Pravduke, L.M.: 1958, Izv. Gl. Astr. Obs. Pulkovo, 20, 55.

Pope, T. and Schoolman, S.: 1975, Solar Phys. 42, 47.

White, O.R.: 1963, Ap.J. 138, 1316.

Zirin, H.: 1975, Ap.J. 199, L63.

FIGURE CAPTIONS

Figure 1:

Mt. Wilson 19448, August 5, 1974. 1707:35 UT

a) Continuum at 5872 Å;

b) D_3

c) Difference picture, b-a, showing D_3 features. Diffuse mottling and failure of the spot umbrae to cancel are artifacts of the reduction process;

d) Hα

The strongest D_3 features can be seen on the undifferenced frame as obscurations of or dark appendages to the continuum faculae. On the difference frame, weaker features are visible down to D_3 depths ≃ .5%. The bright D_3 limb band is apparent. Some of the 1" D_3 knots near the large spot lie in the penumbra. The filament and the surge seen in Hα do not appear in D_3, although the plages below them are visible.

Figure 2:

Observed normalized D_3 profile. Weighted average of 17 plage profiles with mean central depth of 5.0%. Error bars on data points are $\pm$ 1σ deviation of the mean, and average .6% in intensity. Curve is the best fit Gaussian, with 1/e width = .40 Å. Instrumental profile has a FWHM of .19 Å, and contributes .01 Å to the observed linewidth.

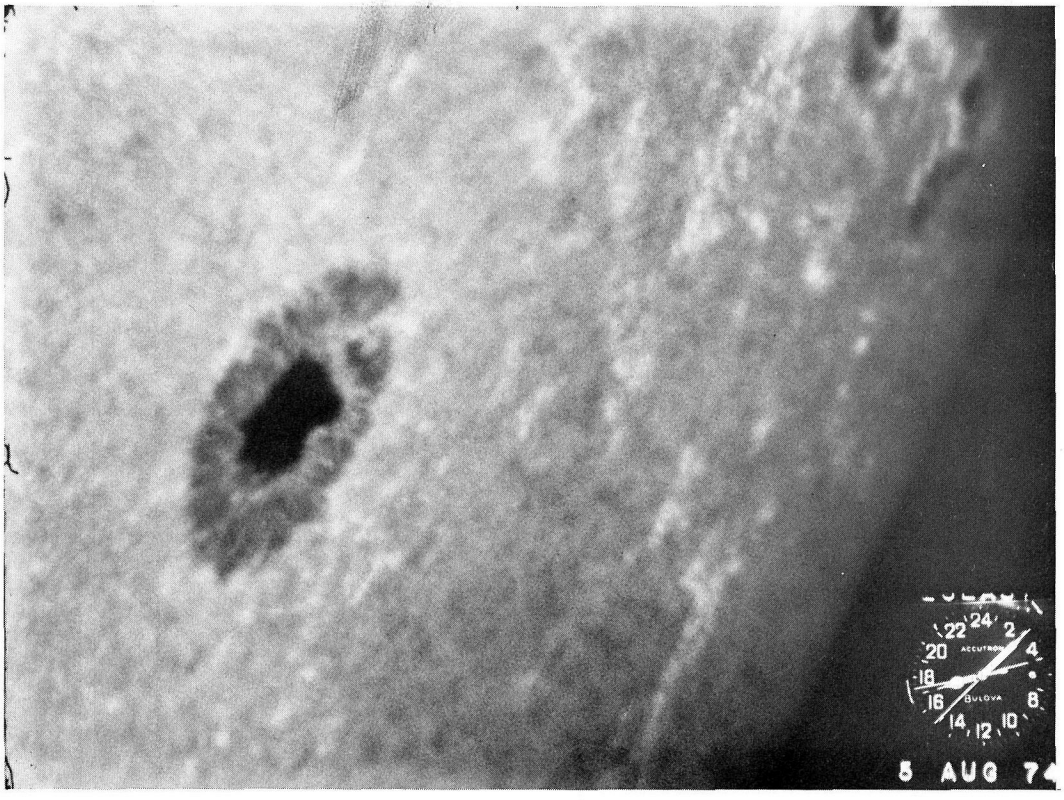

A

20″

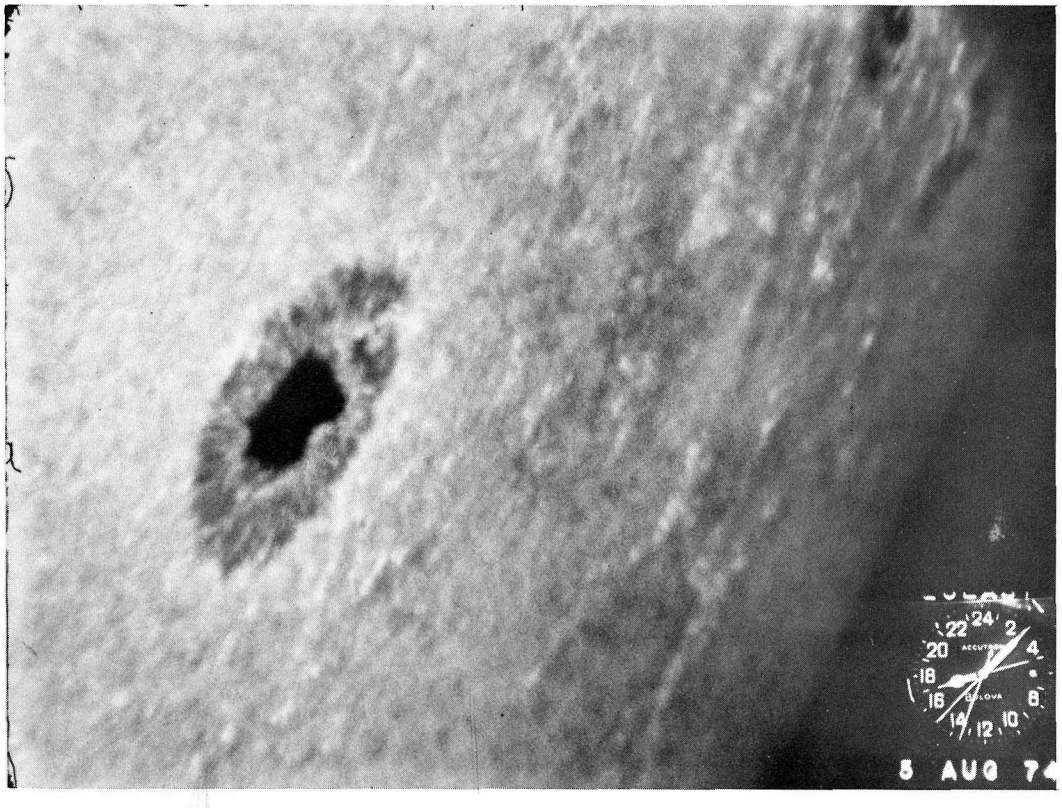

B

FIGURE 1 (A,B)

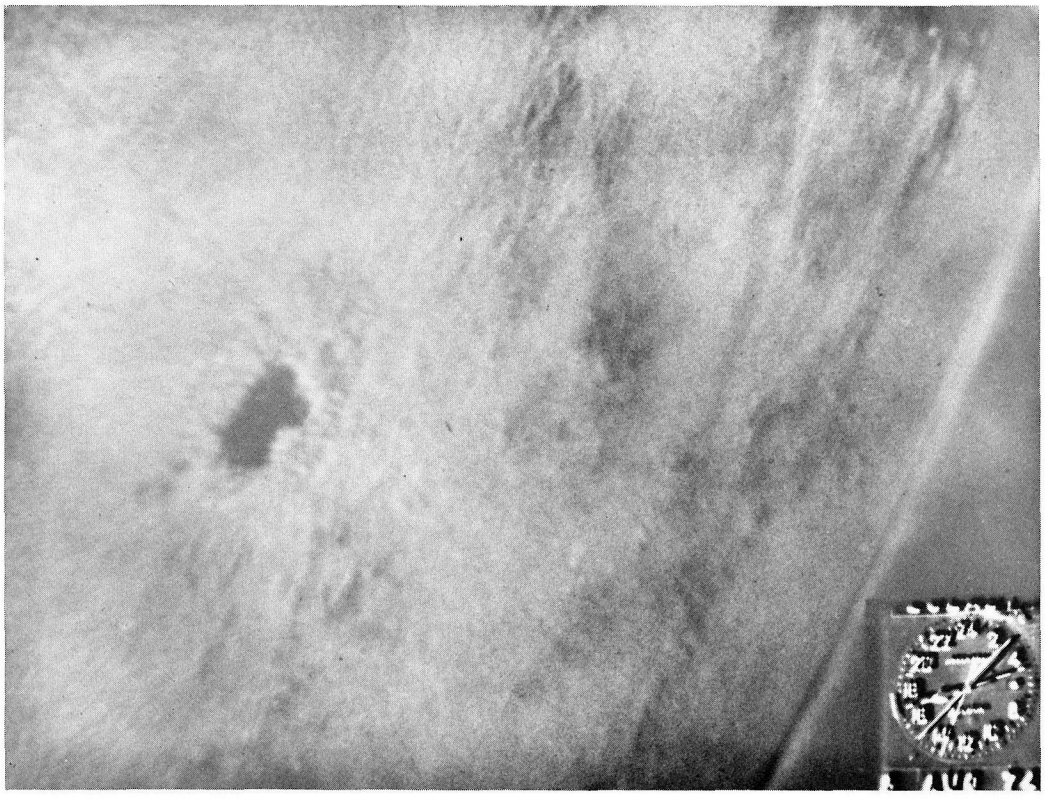

C

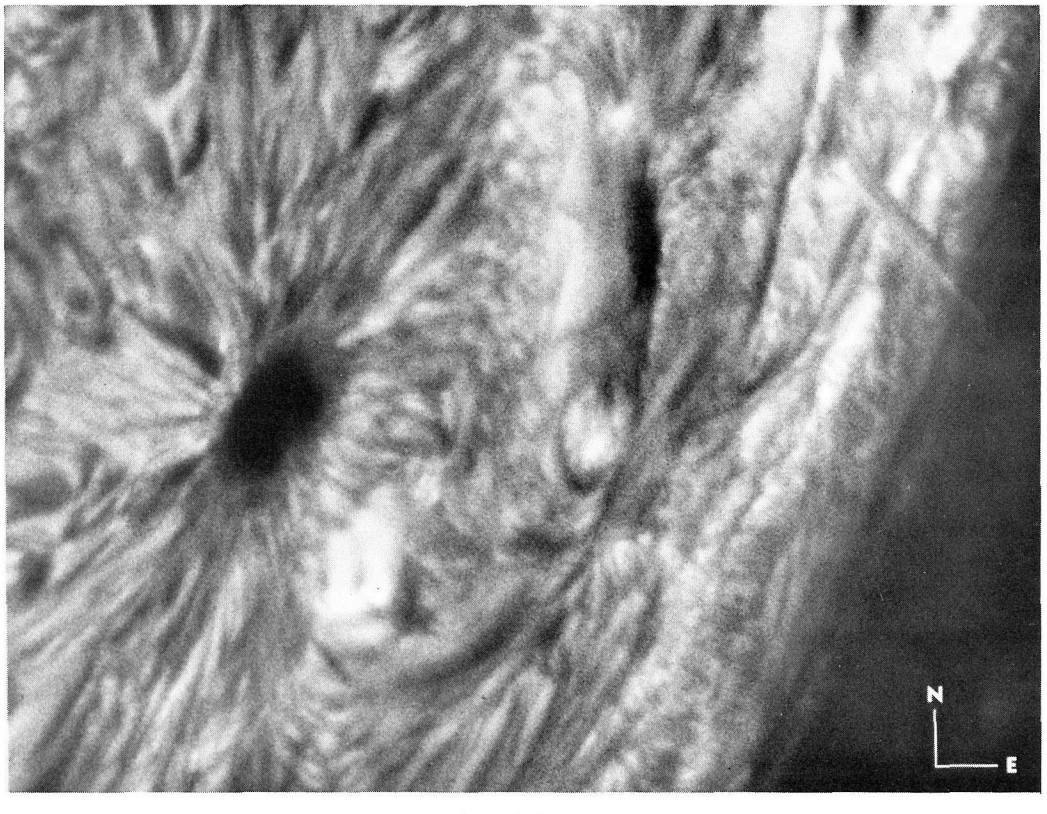

D

FIGURE 1 (C,D)

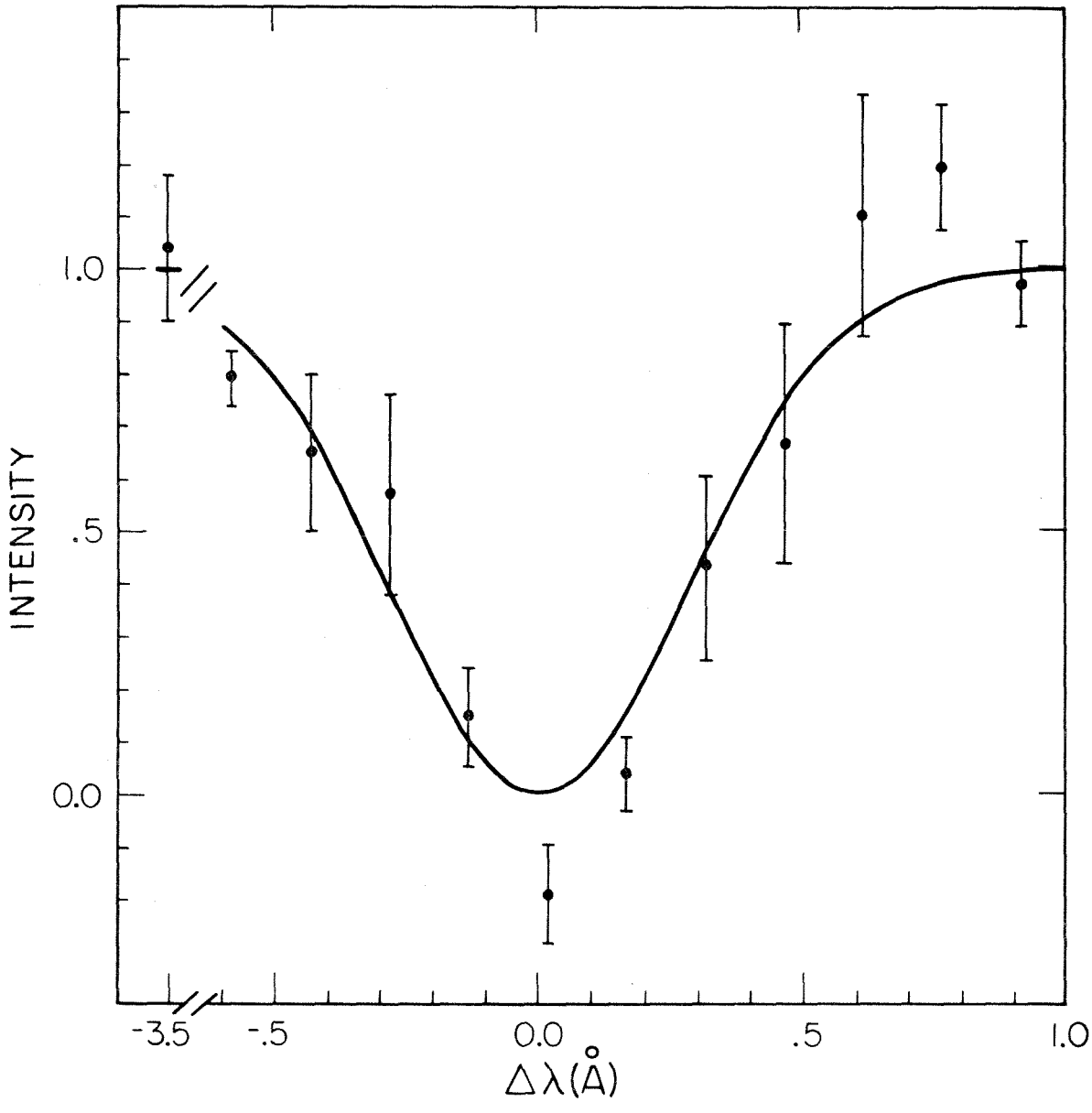

Figure 2

CHAPTER 3

THE PROPERTIES OF MACROSPICULES OBSERVED IN Hα AND D_3

Appears as BBSO Preprint No. 0171

ABSTRACT

Macrospicules have been observed in Hα and He I D_3, on the disk and above the limb. D_3 intensities are a few x 10^{-3} of the disk center, and do not decrease in coronal holes. The ratio of Hα to D_3 intensities is ≈10. Electron densities of 1 to 2 x 10^{10} cm^{-3} are derived from the D_3 intensities, using the coronal EUV model to control the helium ionization. The Hα to D_3 ratio is not understood.

1. INTRODUCTION

Small scale activity is common in the quiet Sun. Its most obvious form, the Hα polar limb surge, was first reported as a distinct phenomenon by Godoli and Mazzucconi (1967). This type of event was observed earlier (Roberts, 1945), but not distinguished from ordinary spicules. Limb surges occur in quiet regions at all latitudes, not only at the poles, and are called Hα macrospicules. Ramsey and Mosher (1976) have described the structural appearance of Hα macrospicules and their frequency of occurrence as a function of latitude and solar cycle phase.

Recently, Moore et al., (1977) have shown that Hα macrospicules correspond to extreme-ultraviolet (EUV) macrospicules (Bohlin et al., 1975; Withbroe et al., 1976), and to flares in soft X-ray bright points (Golub et al., 1974). The work of Golub et al. and Harvey et al., (1975) has previously indicated that the X-ray bright points are the coronal manifestations of magnetic ephemeral regions. We may thus identify the sites of macrospicules as ephemeral regions near the limb. The ability of ephemeral regions to produce small Hα flares and surges was recognized when they were first discovered (Harvey and Martin, 1973). It has seemed that the small scale of activity in ephemeral regions is commensurate with their

small magnetic fluxes, short lifetimes, and simple, bipolar structure (Harvey et al., 1975).

Macrospicules have also been observed in the He I D_3 line (Ramsey et al., 1975). We report here on further observations in Hα and D_3. In addition, we show that the physical conditions in macrospicules can be derived from an analysis of the observed D_3 properties. The only previous determination of macrospicule conditions is that of Withbroe et al., (1976), based on EUV data from two events. The ability to use optical observations, which can be obtained in quantity, is therefore of interest.

2. OBSERVATIONS

2.1 Instrumentation

For this study, filtergram movies were made at the Big Bear Solar Observatory, in Hα and D_3, with the 25 cm vacuum refractor. Filter bandwidths were 0.25 Å at Hα, and 0.19 or 0.38 Å at D_3. The field covered was 4.2 by 5.6 arcminutes at Hα, 5.5 by 7.3 arcminutes at D_3, with the long dimension oriented east-west.

Data from three observing runs were used: May 20 to June 20, 1975, with 122 hours of D_3 film from 20 days, covering the disk and limb, with a 0.19 Å filter; September 19 to October 2, 1975, with 99 hours of D_3 film from 12 days, deeply exposed at the limb, with a 0.38 Å filter; October 28 to November 12, 1975, with 54 hours of D_3 film from 15 days, covering the disk and limb, with a 0.38 Å filter.

2.2 Appearance at the Limb

2.2.1 Hα

Hα macrospicules are easily observed with our instrument. Figure 1 shows one example, which illustrates many of the commonly observed features. Events in Hα generally reach altitudes of 8000 or 20000 km above the continuum limb. Most have multiple knots, spikes, loops, and other

fine structure, and are more similar in appearance to filament eruptions than to simple spike surges. Lifetimes are typically a few minutes; the specific events discussed in this paper were among the larger macrospicules seen, and lasted 7 to 15 minutes.

Differential motion of fine structures relative to each other is normal. In many events, motion of the macrospicule along the limb is seen before the vertical eruption occurs. Apparent velocities, both horizontal and vertical, can be tens of $km\text{-}s^{-1}$ in the early stages. For example, the event of Figure 1 moved horizontally at 40 $km\text{-}s^{-1}$ and vertically at 60 $km\text{-}s^{-1}$, and that of Figure 2, 40 $km\text{-}s^{-1}$ vertically, at some times.

The complex appearance and evolution of macrospicules determines a definite time direction; it is easy to tell if the film is being viewed forwards or backwards. Only in a minority of events is a simple up-and-down flow along a tube suggested.

During the September 19 to October 2, 1975 run, in 47 hours at the south pole, within the polar coronal hole, 13 prominent (in terms of size, intensity, and structure) Hα macrospicules were counted. In 52 hours at the east limb, 19 events were seen. Using the known field size, one may convert these counts into an expected rate for the entire 360° of limb. This yields rates of 5.0 ± 1.4

events-(hour-360°)$^{-1}$ at the pole, and 8.7 $\pm$ 2.0 events-(hour-360°)$^{-1}$ at the equator. A higher rate is expected at the equator since the surface density of ephemeral regions is larger in the active latitudes (Martin and Harvey, 1976). The relatively small difference in the rates at the pole and equator indicates that the distribution of ephemeral regions in 1975 was nearly uniform up to the pole, a fact which is somewhat masked in the magnetic observations by a steep limb visibility function (Harvey et al., 1975). Mosher (private communication) has shown that the number of Hα macrospicules detected can vary by orders of magnitude, depending upon the observing technique; therefore these rates should only be considered as measures of the detection threshold. As an example, Moore et al., (1977), using the 22 cm vacuum refractor at Big Bear, which gives a full disk Hα image, found 45 prominent events in 185 hours on film exposed for the disk, or a rate of 0.24 $\pm$ 0.04 events-(hour-360°)$^{-1}$.

2.2.2 D_3

A few events were also detected in D_3. Figure 2 shows one example, in both Hα-1.0 Å and D_3 line center. In the figure, the Hα limb is the top of the spicules, approximately 3300 km (at this wavelength) above the photospheric limb seen in D_3. At the time of maximum

intensity, Hα emission can be traced to 20 000 km above the photosphere, and D_3 to 10 000 km. The macrospicule diameter is 2500 km in D_3, and is similar in Hα, although finer structure can be seen in Hα.

D_3 emission peaks in the lowest, brightest part of the Hα structure, as Ramsey et al.,(1975) have noted. It does not come from a sheath surrounding the Hα. Soft X-ray and EUV emission from similar events prove the existence of hotter material around the Hα structure; we infer that the D_3 emission is therefore apparently produced not at high temperature, but at high density. In Figure 2, the D_3 evolution parallels that of Hα; this is true for the other events as well.

Of the total 32 Hα events seen during the September 19 to October 2, 1975 run, D_3 film was obtained for 28. Only 4 macrospicules were detected in D_3; two at the south pole, and two at the east limb. Although the sample is small, the fact that equal numbers were seen at pole and equator suggests that D_3 macrospicules may not share the polar darkening evident in the D_3 limb band (Zirin, 1975; Marsh, 1977). This will be discussed further in later sections.

2.3 Emission Intensities

We have measured the Hα and D_3 intensities of the

four events with detectable D_3. A photometer was used in a projected image. Its circular aperture had a diameter corresponding to 0.5 arcseconds at Hα, 0.7 arcseconds at D_3.

Results are summarized in Table 1. Column 3 gives the altitudes above the photospheric limb at which the measurements were made. It was desirable to measure the D_3 at a low altitude where it was brightest, but in Hα, the presence of spicules forced the measurements to be made somewhat higher. Column 4 gives the maximum D_3 line center intensity in units of I_{DC}, the specific intensity of the continuum at disk center. Column 5 gives the same quantity for Hα, at the wavelength(s) relative to line center given in parentheses. At D_3, $I_{DC} = 3.36 \times 10^6$ ergs $(cm^2 s\text{-}st\text{-}\mathring{A})^{-1}$; at Hα I_{DC} is less by the factor 1.15 (Labs and Neckel, 1968).

The obvious result from Table 1 is that Hα is much brighter than D_3, with ratios of energy per unit wavelength from 5 to 25. If the ratio of Hα to D_3 linewidths is greater than 1 (for example, being $\gtrsim 2$ in spicules;[Beckers, 1972]), the total energy emission is correspondingly greater.

For the polar events, film was obtained at two wavelengths in Hα, although neither was line center. The general evolution was similar at both wavelengths, but

the fine structure was completely different. This difference in the fine structure implies that the linewidth at any point must be less than the separation of the two wavelengths, 1.5 Å. Substantial Doppler shifts are expected if the observed transverse velocities represent actual mass motions, 1 Å at Hα corresponding to 46 km-s^{-1}. Intensities observed in the line wings may thus be representative of those measured in the other parts of the macrospicule seen at line center.

The two events of September 20, 1975 occurred in the same region. A third event followed at 1935 UT, with no detectable D_3. Multiple events from a single site are not unique, and were noted on the disk by Harvey and Martin (1973). Relative intensities of these events are better determined than their absolute values, the 1903 event (Figure 2) being brighter in D_3, and fainter at Hα - 1 Å, by about the ratios of Table 1.

The September 27, 1975 event (Figure 1) was at the detection limit in D_3. Any fainter D_3 event would be missed.

The intensities in Table 1 have been corrected for the effects of the filter parasitic light, but not for the convolution of the filter and macrospicule line profiles, as the exact line shapes and shifts are unknown in the macrospicules. For an unshifted Gaussian line of width

0.4 Å, the D_3 intensities are changed to 5, 8, 3, and 7×10^{-3} for the events listed. For an 0.8 Å Hα linewidth, the values given are unchanged. Intensities on the disk were taken from the limb darkening curves of Pierce and Waddell (1961) for D_3, and White (1962) for Hα.

The estimated absolute accuracy of these measurements is ± 50%. Principal limits on the accuracy were the difficulty of measuring the characteristic curve of the film over a range of nearly 4 in density, the nearness of the D_3 intensities to the detection limit, confusion with spicules in Hα, and uncertainties in the filter parasitic light contribution.

2.4 Appearance on the Disk

Hα macrospicule events are also visible on the disk, and were found in magnetic ephemeral regions by Harvey and Martin (1973). The most obvious form is the filament eruption, illustrated in Figure 3. In the figure, a filament connecting a bipolar ephemeral region to nearby magnetic fields darkens, erupts in loops, and disappears. Both the ephemeral region and filament are within the interior of a supergranule cell. Events of this type are easily detected and are quite distinct from the normal action seen in quiet regions. The presence of a clearly bipolar ephemeral region is neither necessary nor usual,

as similar events occur in otherwise blank areas as well.

Surge-like macrospicules are also seen, as in Figure 4. These are distinguished from normal spicule events by their larger length, width, and lifetimes, composite structure, and, as in the event of Figure 4, significant brightening at the base.

A third type of disk macrospicule is the flare brightening, sometimes accompanied by a small surge. Examples are given by Glackin (1975). In these events, the brightening dominates the appearance, rather than the surge. Again, the presence of a distinct ephemeral region is unnecessary, as brightenings have been observed in previously blank locations. There are no examples of such events with simultaneous D_3 film, however.

In 176 hours of film from the May to June 1975 and October to November 1975 observing runs, which covered the disk in the equivalent of a raster pattern, 10 Hα events were seen. Allowing for a 1/3 reduction of the effective area covered due to the inclusion of plages, filaments, and sky in the field, a rate of 2.8 events per hour on the visible disk is inferred. If we take 10 000 Km as a typical height, the area covered by observations above the limb corresponds to $\approx$ 0.17 of the area of the visible disk. The disk rate may then be converted to a limb rate of 0.5 ± 0.2 events-(hour-360°)$^{-1}$. This is

lower than the total rates obtained at the limb, as expected, since the disk contrast of the smallest events seen off the limb is too low to permit detection. It is equal to 1/2 the rate of limb events with detectable D_3.

Of the 10 Hα events seen on the disk, D_3 film was available for 6, including those of Figures 3 and 4. No D_3 was detected in any part of any of these events, with a contrast threshold of 2 to 3%. The invisibility of macrospicules on the disk in D_3 is consistent with their low intensities observed at the limb.

2.5 Hα/D_3 Intensity Ratio

To obtain statistical data on the appearance of macrospicules in D_3 relative to Hα, film from Lockheed Solar Observatory twin eclipsing telescope (Ramsey et al., 1975) was studied. This instrument records the entire limb in both lines simultaneously, through wide filters ($\approx$ 10 Å FWHM); the Hα beam is further filtered so that quiescent prominences have the same film density in both images. The characteristic curve of the film is sufficiently similar at these two wavelengths to make relative intensity measurements meaningful. Stellmacher's (1972) data on 10 quiescent prominences give $R_Q = I(H\alpha)/I(D_3) = 11 \pm 3$.

Film from four days (June 25-27, July 3, 1974) was studied, totaling 31 hours, selected for its image quality

and freedom from active regions at the limb. The limb was divided into quadrants, giving separate data for the poles and equator. Macrospicules were selected in Hα, then rated on a visual intensity scale in each line (Table 2). Ninety-two macrospicules were found. The rate of appearance in the polar quadrants, 4.0 ± 0.5 events-(hour-360°)$^{-1}$, was constant from day to day, within 10%. The rate in the equatorial quadrants varied inversely with the amount of prominence material visible, equaling the polar rate on the best days. Confusion with Hα prominences prevented identification of the fainter macrospicules. This problem did not occur with the Big Bear data, because the larger image scale, lack of occulting, and higher resolution permitted the separation of macrospicules and moving prominence material.

On average, the D_3 intensity was proportional to the Hα intensity, but much weaker. The correlation coefficient $r = 0.53$, and the probability of no correlation $P(r=0 \mid r,92) = 2 \times 10^{-6}$. No events were found with an intensity ratio of Hα to D_3 in the macrospicule, R_M, less than R_Q; in only 5% was $R_M \simeq R_Q$. In 45% of the events, D_3 was indetectable, $R_M \gg R_Q$. To calculate the average ratio for all events, $\overline{R}_M$, the effects of the equatorial bias toward brighter events must be removed. Values of $R_M(I_{H\alpha})$ are determined separately for the pole and equator,

and the average ratio is then

$$\bar{R}_M = \frac{\sum_{I_{H\alpha}} N(I_{H\alpha})\ R_M(I_{H\alpha})}{\sum_{I_{H\alpha}} N(I_{H\alpha})} ,$$

where the distribution of number versus intensity, $N(I_{H\alpha})$, is taken to be the polar distribution. $\bar{R}_M$ is the same at the poles, 2.0 ± 0.3 on our visual scale, and the equator, 1.8 ± 0.4. This confirms, with a larger sample (51 detected D_3 events), the suggestion from the Big Bear data that D_3 macrospicules are not dimmer at the poles.

2.5.1 Doppler Brightening

Ramsey et al., (1975) suggest that part of the Hα enhancement (i.e., $R_M > R_Q$) is caused by Doppler brightening (Hyder and Lites, 1970) in the moving material of the macrospicule. The Doppler mechanism predicts intensity maxima during ascending and descending phases, when the velocity transverse to the line of sight is large, and an intensity minimum at the time of maximum height, when the transverse velocity is zero. It also predicts wavelength shifts of the Hα line (Rompolt, 1967), but confusion with line-of-sight velocities is unavoidable. Indeed, most events do fade as they rise, and their velocities decrease. However, because a descending phase is rarely observed,

the expected brightening as the material falls cannot be confirmed. Rather, most macrospicules fade to invisibility upon reaching their maximum height.

This monotonic intensity decrease must be a sum of any Doppler effects plus a change in the state of the material in the macrospicule. From the morphology, it is clear that the macrospicule undergoes a monotonic expansion, with a corresponding reduction in density. This in turn gives a reduction in the recombination rates. Since the hydrogen ionization rate is primarily radiatively controlled (Pottasch and Thomas, 1959), it is independent of the local density. Therefore, as the macrospicule expands, the ionization fraction of hydrogen increases, reducing the bound level populations, and the Hα intensity.

2.6 Intensity Distribution

Observed Hα macrospicule rates at the poles were equal within the errors, in the Big Bear and Lockheed data. If the actual rate of macrospicule production was the same during both observing runs, then the detection level in Hα was also the same. Mosher (private communication) finds no detectable solar cycle variation in the polar macrospicule rate. Although solar cycle variations of ephemeral regions (Harvey et al., 1975) and coronal bright points (Davis et al., 1977) have been observed, the expected

variation between the observing runs is less than the counting errors.

In the Lockheed data, a ratio of total energy emission in Hα to D_3 of $R_Q \simeq 11$ is required to produce equal film densities. In the Big Bear data, assuming a ratio of Hα to D_3 linewidths of 2, the required energy ratio is $\simeq 4$. The faintest events detected on the Lockheed film are thus $\simeq 3$ times less intense than those on the Big Bear film. With this higher sensitivity, the fraction of macrospicules detected in D_3 rose from 17% to 56%, also a factor $\simeq 3$. The integral number of macrospicules brighter than a given D_3 intensity I_o is thus $n_M(I > I_o) \propto I_o^{-1.2\pm0.5}$.

3. D_3 EXCITATION

The observation that $\overline{R}_M$ is the same at the poles and equator is most interesting. It has been shown (e.g., Hirayama, 1971; Zirin, 1975) that D_3 in the quiet sun is controlled by radiative processes, as originally suggested by Goldberg (1939). Coronal EUV radiation ionizes He I from the ground state; recombination populates the metastable triplet terms. Excitation of the triplet lines, including D_3, is fixed by scattering of the photospheric continuum. The decrease of the coronal EUV flux in coronal holes, measured by Munro and Withbroe (1972), Withbroe and Wang (1972), and Huber et al. (1974) to be a factor of 5, is reflected in an observed factor of $\gtrsim 3$ decrease in the D_3 limb band brightness (Pope and Schoolman, 1975; Zirin, 1975).

D_3 limb band scans taken during the 1975 Big Bear run showed that the polar area studied was within a coronal hole, while the equatorial area was not. A soft X-ray photograph from June 27, 1974 (D. Rust, private communication), in the middle of the days studied on Lockheed film, shows the polar hole boundaries at 60 to 65° latitude, with the holes occupying about 2/3 of each polar quadrant. (These values for the boundary latitudes are also those typically found in the Big Bear D_3 scans made since 1974, currently reported in Solar-Geophysical Data.) The X-ray

picture also shows a hole near disk center which may have contaminated the west limb data of July 3; but that is only 1/4 of the total equatorial data.

Considering the film gamma of ≈ 3, even a small systematic intensity difference between macrospicules in and out of coronal holes should have been obvious. Because no such difference is seen, the production of D_3 in macrospicules must be independent of the spatial variations of the global coronal EUV radiation field, unlike the normal quiet chromosphere.

Collisional control of the helium system can be ruled out. Temperatures of order 20 - 60 000°K at densities of 10^{10} to 10^{11} cm^{-3} would be required for the collisional rates to dominate the radiative rates in the ionization equilibrium. Withbroe et al. (1976) have determined the emission measure of macrospicules in this temperature range to be $\simeq 1.5 \times 10^{35}$ cm^{-3} per 1 cm horizontal slice. At the densities stated, the macrospicule would have to be 20 - 200 km in radius, in obvious contradiction of the observations. Since the events observed at Big Bear and Lockheed were smaller than those of Withbroe et al., the mass at high temperature should be correspondingly smaller.

With the EUV controlling the helium ionization, there is one circumstance in which the D_3 intensity is independent of exact value of the EUV flux: if the flux is large

enough to fully ionize helium to He II. The D_3 intensity then depends only upon density. To demonstrate this, the solutions for macrospicules will be displayed, in the two cases of an optically thin, and thick, 504 Å continuum.

For these calculations, the macrospicule is represented as a cylinder of constant density, temperature 10^4 K, lifetime $t_M \simeq 600$ s, and radius r_M and height h_M such that $r_M << h_M << H$, the scale height of the diffuse coronal emission ($r_M:h_M:H \simeq 10^8:10^9:6 \times 10^9$ cm).

3.1 Optically Thin Continuum

At low densities and high ionization fractions, the He I 504 Å continuum is optically thin, with the ionization balance for each volume element

$$N_I \; 2\pi \; \Phi_1 \; R_I = N_{II} \; N_e \; \alpha_I \qquad (1)$$

$$\text{with } 2\pi \; \Phi_1 \; R_I = \int d\Omega \int d\lambda \; I(\Omega,\lambda) \; a_I(\lambda)$$

where N_I, N_{II}, N_e are the He I, He II and electron number densities, α_I the total recombination coefficient to all singlet terms, I the EUV intensity, and a_I the 504 Å absorption cross-section. The angular factor Φ_1 and photon absorption rate R_I are derived in the Appendix; R_I varies from quiet sun to coronal hole.

The triplet terms are populated by recombination,

$$\Sigma\, N_{n^3L}\, R_{n^3Lk} \equiv N_T\, R_{Tk} = N_{II}\, N_e\, \alpha_T \qquad (2)$$

with N_{n^3L}, N_T the n^3L and total triplet number densities, R_{n^3Lk}, R_{Tk} the n^3L and total effective photoionization rates, and α_T the total recombination coefficient to all triplet terms. In a volume optically thin in all triplet lines, most of the triplet population is in just two terms, as $N_{2^3S}:N_{2^3P}:N_T = 0.85:0.15:1.0$, all others totalling 5×10^{-3} N_T. The ionization rates are determined by inverting the recombination coefficients of Burgess (1958) and Burgess and Seaton (1960) with the spectra of Labs and Neckel (1968) and Tousey et al. (1974); for example, $R_{2^3Sk} = 236\ s^{-1}$, $R_{2^3Pk} = 9870\ s^{-1}$, and $R_{Tk} = 3300\ s^{-1}$.

In addition, the conservation of total helium number density requires

$$N_I + N_{II} = 0.11\, N_e \qquad (3)$$

assuming 90% hydrogen ionization (Giovanelli, 1967) and an abundance ratio of helium to hydrogen of 0.1 by number. The He III number density will be shown to be negligible.

From Equations 1 and 3 an expression for N_{II} is obtained, which upon substitution into Equation 2 gives

$$N_T = \frac{0.11\, N_e^2\, \alpha_T}{R_{Tk}} \left[\frac{2\pi\, \Phi_1\, R_I}{N_e\, \alpha_I + 2\pi\, \Phi_1\, R_I} \right] . \qquad (4)$$

[This form has also been obtained by Livshits (1976) and Livshits et al. (1976); they wrongly applied it to spicules and the quiet chromosphere, which are optically deep (Marsh, 1977).] It is clear that for

$$N_e < N_e^* = \frac{2\pi \Phi_1 R_I}{\alpha_I} \qquad (5)$$

the quantity in brackets in Equation 4 approaches unity, and the triplet population is independent of the EUV flux. Since Equation 5 must hold in coronal holes, $R_I^H = 4.1 \times 10^{-4}$ s^{-1} st^{-1} is used, giving $N_e^* = 1.1 \times 10^{10}$ cm^{-3}.

At $N_e = N_e^*$, $N_T = 420$ cm^{-3}, $N_2{}^3P = 60$ cm^{-3}, and, assuming a 0.4 Å Doppler linewidth, as found in plages (LaBonte, 1977), or about that of spicules (Beckers, 1972), the D_3 optical depth is

$$\tau_{D_3} = 2.6 \times 10^{-13} (2r_M) N_2{}^3P = 3.2 \times 10^{-3} .$$

The D_3 source function is set by pure scattering of the photospheric continuum at $S_{D_3} = 0.35\ I_{DC}$, giving a brightness at line center of $1.1 \times 10^{-3}\ I_{DC}$, just below the values measured (Table 1).

Only the diffuse coronal emission was counted in deriving N_e^*. The resulting intensity suggests that for the large numbers of faint macrospicules seen in the Lockheed data, that source alone is sufficient to produce flux independent D_3 emission, as observed. For the

brightest events, observed at Big Bear, densities larger than N_e^* are required, violating flux independence. Since even these events show no pole-equator intensity effect, it is suggested that N_e^* was underestimated (at least, for these events), with, perhaps, local EUV emission being important (Section 3.3).

3.1.1 Consistency Criteria

Consistency checks need to be made. First, is the optical depth in fact small? From Equations 1, 3, and 5,

$$N_I = \frac{0.11\ N_e^2}{N_e + N_e^*} = 6.1 \times 10^8\ \text{cm}^{-3} \qquad (6)$$

for $N_e = N_e^*$. The central depth of a cylinder of radius r_M at the optically thin mean wavelength, $\lambda_n = 370$ Å, (see Appendix) is

$$\tau(\lambda_n) = r_M\ N_I\ a_I(370\ \text{Å}) = 0.25.$$

This is not too large when one considers that, because of the limb brightening of the coronal EUV emission, most photons enter the cylinder radially. The hydrogen Lyman continuum due to the failure of total ionization, can be calculated with a value of N(H I)/N(H II) from Giovanelli (1967) for a 2000 km slab with density N_e^*, and is 0.04.

Next, is N_{III} small? The equilibrium is

$$\frac{N_{III}}{N_{II}} = \frac{2\pi\ \Phi_1\ R_{II}^{H}}{N_e^{*}\ \alpha_{II}} = 4.8 \times 10^{-3}. \qquad (7)$$

This condition is also satisfied.

Third, is equilibrium actually achieved, that is, does the helium system equilibrate in a macrospicule lifetime? The time dependent equation

$$\frac{\partial N_{II}}{\partial t} = -N_e \alpha_I\ N_{II} + N_I\ 2\pi\ \Phi_1\ R_I \qquad (8)$$

can be solved analytically with Equation 3 and the boundary condition $N_{II}(t=0) = 0$, because the rate coefficients are independent of the helium system. The resulting time constant is $t_e = (N_e\ \alpha_I + 2\pi\ \Phi_1\ R_I)^{-1}$. With $N_e = N_e^{*}$, $t_e = 200$ s $< t_M$. Equilibration times for N_T and N_{III} are less than t_e.

Finally, what is the effect of fine structure? The application of the analysis to an inhomogeneous object will derive a root-mean-square density, since

$$N_e\ (\text{derived}) \propto (I_{D_3}/r_M)^{\frac{1}{2}} \propto \left[\frac{\int N_e^{2}(\text{actual})\ dr}{\int dr}\right]^{\frac{1}{2}}.$$

As long as the intensity and radius are representative of the object, this is a fair estimate.

3.2 Optically Thick Continuum

Here, the exact geometry is more important, as the

ionization fraction will vary through the volume even though the total density does not. The total number of ionizing photons crossing the macrospicule surface is balanced by the total number of recombinations in the volume,

$$2\pi\ \Phi_2\ \mathcal{F}_I\ A_M = \int N_{II}\ N_e \alpha_S\ dV = \bar{A}\ \alpha_S \int N_e\ N_{II}\ dr \qquad (9)$$

where the angular factor Φ_2 and the EUV photon flux $\mathcal{F}_I$ are derived in the Appendix; A_M is the macrospicule surface area, $\bar{A}$ a mean density weighted area, and α_S the total recombination coefficient to all singlet terms except the ground state. In actual events, $\bar{A}$ varies from A_M (N_{II} concentrated at the surface) to 0.5 A_M (N_{II} constant); an average value of 0.75 will be used.

Only recombinations to excited singlet terms are counted in Equation 9 because the escape probability of 504 Å recombination photons produced is negligible. On average, the incident coronal photons penetrate to $\tau(\lambda_k) = \tau(300\ \text{Å}) = 1$ (see Appendix), or $\tau(504\ \text{Å}) = 2.8$. Scattering in the continuum is effectively coherent, as the absorption cross-section is a broader function of wavelength than the emission profile; therefore, τ^2 steps are required to scatter to the surface, with a probability of scattering (as opposed to degrading; Athay, 1972) at each step of $P_s = (\alpha_I - \alpha_S)/\alpha_I = 0.72$. Only $\frac{1}{2}$ the photons

move toward the surface, so the escape probability is

$$P_e(504\ \mathring{A}) \simeq \tfrac{1}{2}\,(P_s)^{\tau^2} = 0.04.$$

The actual escape probability is even lower than this, since the incident coronal photons enter the cylinder radially, while the 504 photons also scatter vertically, along paths with larger optical depths. Because the 504 photons do not escape, they simply cause reionization, with no net recombination. On the other hand, recombinations to excited states are effective, with cascade leading to the production of 584 $\mathring{A}$ line photons. Although $\tau(584) = 1.6 \times 10^3\ \tau(504)$, for a 0.04 $\mathring{A}$ Doppler linewidth, scattering in the line is incoherent, and only τ steps are required for escape. Further, the probability of scattering is much larger, $P_s = (1 - 4 \times 10^{-9})$, for collisional degradation at 10^4 K, $N_e = 10^{10}$ cm^{-3}. The line escape probability is thus unity, even for photons which move initially inward. (This is why chromospheric HeII 304 $\mathring{A}$ line photons freely penetrate the macrospicule.)

Solving Equations 2 and 9,

$$\int N_T\, dr = \frac{2\pi\ \Phi_2\ \mathcal{F}_I}{R_{Tk}}\ \frac{A_M}{\bar{A}}\ \frac{\alpha_T}{\alpha_S} = 2.9 \times 10^{11}\ \text{cm}^{-2} \qquad (10)$$

is obtained, again taking the value of the EUV flux in a coronal hole. This form is not flux independent, but is independent of the temperature, density, and size of the macrospicule. All optically thick vertical cylinders

should have equal D_3 intensity.

The D_3 optical depth is

$$\tau_{D_3} = 2.6 \times 10^{-13}(0.15)\ 2 \int N_T\ dr = 2.3 \times 10^{-2},$$

and the intensity, $7.9 \times 10^{-3}\ I_{DC}$. This is the maximum intensity a cylinder can achieve if illuminated only by the diffuse coronal hole EUV. Outside a hole, the flux, and thus maximum intensity, is 3 times larger. No account need be taken for hydrogen Lyman continuum absorption; at the densities of interest, 10^{10} to 10^{11} cm^{-3}, the number of neutral hydrogen atoms $N(HI) \simeq N_I$ (Giovanelli, 1967), and $\tau(HI) = 0.1\ \tau(He\ I)$.

3.2.1 Validity Criteria

For $\tau(\lambda_k) > 1$, an object with radius 10^8 cm must have $N_I > 3.6 \times 10^9$ cm^{-3}, or $N_e > 4 \times 10^{10}$ cm^{-3}. At this density the equilibration times are much less than the event lifetimes, and the N_{III} density is negligible. Density variations within the macrospicule do not alter the total number of triplet atoms (thus, the average D_3 intensity), as long as the entire object still presents a vertical cylindrical silhouette to the EUV photons. However, they would alter the value of $A_M/\bar{A}$ locally, producing fine structure in D_3.

3.3 Local EUV Emission

The diffuse coronal EUV flux is sufficient to explain most D_3 macrospicule intensities. For the large number of faint events seen in the Lockheed data, all the validity criteria are fully met. In the few brightest events, however, there arise problems, as $N_e \gtrsim N_e^*$. For example, at $N_e = N_e^*$, there is a 50% pole-equator intensity difference, as the bracketed quantity in Equation 4 changes from 0.5 to 0.75. Further, for these events, the radius is larger than r_M, and the 504 Å continuum optical depth becomes uncomfortably large. Local EUV emission, either from the macrospicule itself or a nearby coronal bright point, would effectively increase N_e^*, and objects with higher densities would still meet the validity criteria. It will be shown that local emission does make a contribution, in a few of the largest events (just those which otherwise cause difficulties), although it may not be generally important.

Soft X-ray bright point flares (Golub et al., 1974) clearly have enhanced emission from material at $1 - 3 \times 10^6$K, the temperature range from which the EUV lines important to helium ionization are emitted. However, Moore et al. (1977) show that events with detectable X-rays are only a small fraction of all macrospicules, apparently only the most dense. Golub et al. (1974) estimate 50 to 100 bright

point flares per day on the entire sun; the average Big Bear limb rate of 7 events-(hr-360°)$^{-1}$ corresponds to 2000 macrospicules per day on the entire sun. Observations of Withbroe et al. (1976) detect no Mg x 625 Å line emission from other macrospicules, yet this line should also be produced at a few million degrees. The EUV emission of the macrospicule itself is therefore important only in a few large events.

The case of coronal bright point contributions is similar. The contrast of the bright points relative to the diffuse emission falls rapidly as one looks toward the limb (e.g., Figure 6 of Noyes et al., 1974). Only the few brightest points [we estimate $\simeq$ 60-180 ($A_\odot$-day)$^{-1}$] have angle averaged surface brightnesses larger than that of the diffuse component. In addition, the solid angle occupied by a bright point will be less than 2π, even if the macrospicule is embedded, and much less if it is not, as in Figure 3. The total contribution from a bright point is thus also generally small, except in a few large points, which presumably produce the largest macrospicules.

There is one phenomenon in D_3 itself which provides evidence of local EUV emission, namely, the isolated patches of chromospheric D_3 emission seen in coronal holes (Zirin, 1975; Marsh, 1977). The patches are produced by the EUV emission of ephemeral regions (Harvey et al., 1975b).

There are typically 1-2 patches per polar hole; considering the area sampled at the limb, this corresponds to 1-200 patches per $A_{\odot}$. No patch was visible at the site of the September 20 polar macrospicules; however, the events arise beyond the limb, and a low-lying patch would not be seen.

4. MACROSPICULE PROPERTIES

4.1 Macrospicule Densities

No pole-equator intensity difference is observed in the brightest D_3 macrospicules; further, the fraction of events which seem to violate Equation 5 (2/28) is similar to the fraction of all events that have substantial local EUV ($\simeq$ 200/2000). Thus, the bracketed quantity in Equation 4 must be $\simeq$ 1 for these events. Electron densities derived from Equation 4 with this value are given in column 6 of Table 3, and range from 1 to 2 x 10^{10} cm^{-3}. This statistical argument may fail for any single event; densities derived using only the diffuse EUV flux are given in column 5, ranging from 1 to 4 x 10^{10} cm^{-3}. By comparison, from EUV data Withbroe et al. (1976) found electron densities of $10^{10 \pm 0.5}$ cm^{-3} for two events.

For the equatorial events, the larger value of the diffuse EUV flux guarantees that the optically thin case is valid. Any local EUV has little effect, and the densities are well determined. The polar events, however, require local EUV to be in the optically thin regime; the brightest (9/20/75, 1903 UT) has an intensity which is not different from the optically thick limiting value, otherwise. Although the densities of column 6 are the most probable, those of column 5 are possible, and the density of the brightest event may be even larger.

4.2 The Hα Problem

The agreement of the observed D_3 macrospicule intensities and pole-equator behavior with those predicted by a simple model is very satisfying. Unfortunately, the Hα macrospicule intensities pose a problem. An event with an Hα line center intensity of $5 \times 10^{-2}\ I_{DC}$, 0.8 Å Doppler linewidth, and radius r_M has a value of $N_3\ P_e(H\alpha) \simeq 100\ cm^{-3}$, with N_3 the number density of the Hα upper level and $P_e(H\alpha)$ the average probability that an Hα photon will escape the volume. From Giovanelli's (1967) calculations, this corresponds to an electron density of $\simeq 2 \times 10^{11}\ cm^{-3}$, an order of magnitude larger than the values derived from D_3. Using Giovanelli's results for $N_e = 10^{10}\ cm^{-3}$, Hα macrospicule intensities of $\simeq 4 \times 10^{-3}\ I_{DC}$ are predicted, about equal to the D_3 values. No single factor can explain this discrepancy; several sources of error must be important.

Uncertainties in the measured intensities alone are not large enough to account for the difference. This is true for the absolute measurements from the Big Bear data, and especially for the simple relative measures from the Lockheed data. The ratio of Hα to D_3 total intensities must be $\gtrsim 10$, and it is this ratio that cannot be reconciled with both calculations.

The theory has several problems. Some are peculiar to

each calculation; for example, the helium abundance is unknown within a factor of 2, while the hydrogen calculation did not include Doppler brightening, which, at the velocities observed, can produce a 50% intensity increase in Hα. However, most of the problems with the theory are shared by both calculations. Among them are the use of incorrect geometry, especially the neglect of fine structure; neglect of the time variation of the macrospicule and the possibility of nonequilibria; neglect of the spatial variation of the density, ionization and excitation through the object; and use of incomplete model atoms, with various levels and processes left out.

It is not known which problems most affect which calculation; it is likely that both are in error, rather than only one. A simultaneous, mutually consistent solution of both the hydrogen and helium systems will be necessary to resolve the question. Before attempting such a detailed analysis, new data should be obtained, giving the D_3 and Hα line profiles as functions of space and time in several events, to determine the importance of Doppler effects, fine structure, and so on, in detail. We hope to address the observational and theoretical questions in the future.

4.3 Particle Flux in Macrospicules

The total upward particle flux of macrospicules, some

fraction of which may fall back to the surface, is just $F_m = n_m N_e V_m$, n_m the integral rate of macrospicules. Using values from earlier sections, we find $F_m \simeq 7 \times 10^{33}$ nuclei-s^{-1}. This is quite small compared to the solar wind flux, $F_w \simeq 8 \times 10^{35}$.

In the optically thin limit, $I_m \propto N_e^2$, and we have shown that $n_m \propto I_m^{-1}$. If all macrospicules have about the same volume, then $F_m \propto N_e^{-1}$, with most of the mass in low density objects. We again point out that Mosher (private communication) has found that the macrospicule rate is a strong function of detection threshold, and that some coronagraph data show rates 100 times as large as ours. However, to equal the solar wind flux, objects of $N_e \simeq 10^8$ would be needed; there is no evidence for the existence of such thin (and faint) objects, which would actually be less dense than the surrounding corona.

4.4 Macrospicule Energies

As Withbroe et al. (1976) have stated, macrospicule energies are dominated by the ejection energy of the material; this is just the gravitational potential energy at the time of maximum height (a moment which may not be well defined, since events disappear without falling back toward the surface). Contributions, in ergs, from gravitational, ionization, and thermal kinetic energies are

6(h/20 Mm), 2, and 0.4 $(T/10^4\ K) \times 10^{-11}\ N_e V_m$. Turbulent kinetic energy should be of the order of the thermal value. For the events detected at Big Bear in D_3, the total energy ranged from 0.7 to 3×10^{26} ergs. These compare with 3×10^{26} ergs for the events reported by Withbroe et al. (1976). Continued energy injection is not required to maintain the temperature, which must, through photoionization, be set by the external radiation fields.

4.5 The EUV Appearance of Macrospicules

From our analysis, the EUV properties of macrospicules, as observed in the HeI 534 Å, HeII 304 Å lines and the HeI 504 Å continuum, can be predicted. The temperatures and densities are too low for thermal excitation to be important; only recombination and scattering contribute to the EUV transition intensities. From Timothy et al. (1972), the mean disk intensity of quiet regions is $I(584) = 2 \times 10^{13}$ pht-$(cm^2\text{-s-st})^{-1}$, $I(504) = 4 \times 10^{13}$ pht-$(cm^2\text{-s-st})^{-1}$, and $I(304) = 1 \times 10^{14}$ pht-$(cm^2\text{-s-st})^{-1}$ (see Appendix, Section A.1).

Using the optically thin formulae, the recombination intensities are

$$I_r = 2\ r\ N_e \alpha_\lambda N_{i+1}/4\pi\ ,$$

with α_λ the effective recombination coefficient onto the

upper level of (in the case of 504, through) the transition, and N_{i+1} the density of the next higher ionization state. For radius $r = 10^8$ cm and $N_e = 10^{10}$ cm^{-3}, this gives $I_r(584) = 4 \times 10^{12}$ pht-(cm^2-s-st)$^{-1}$, $I_r(504) = 1.3 \times 10^{13}$ pht-(cm^2-s-st)$^{-1}$, and $I_r(304) = 4 \times 10^{11}$ pht-(cm^2-s-st)$^{-1}$.

Since the continuum is optically thin, scattering is not important, but for the lines, which are optically deep, scattering of the disk emission is an important contribution. For the same values of r and N_e, and the linewidths from Doschek et al. (1974), the radial optical depth of the macrospicule is $\tau(584) = 260$, $\tau(304) = 180$. An optically deep vertical cylinder (with a linewidth $\geq$ the disk emission line) has a scattered intensity of 1/4 the average disk intensity. This contributes $I_s(584) = 5 \times 10^{12}$ pht-(cm^2-s-st)$^{-1}$, $I_s(304) = 2.5 \times 10^{13}$ pht-(cm^2-s-st)$^{-1}$.

The predicted total ($I_r + I_s$) 584 intensity is about equally contributed by recombination and scattering, $I_M(584) = 1/2\ I_{disk}$. The 504 intensity is almost entirely from recombination, $I_M(504) = 1/3\ I_{disk}$, while the 304 intensity is mostly scattering, $I_M(304) = 1/4\ I_{disk}$. There are no quantitative measurements of the He EUV macrospicule intensities; the data of Bohlin et al. (1975) indicate that macrospicules are fainter than the disk in 304 and 584, but not greatly so.

The evolution of macrospicules should be much different

in the optically thin transitions (504, D_3), which depend on recombination, and whose intensities vary as N_e^2, than in the optically thick transitions (584, 304), whose intensities are nearly fixed by the disk emission as long as $\tau >> 1$. As the macrospicule rises and expands, its density decreases, and the thin transitions fade proportionally, while the thick transitions maintain nearly constant intensity. For example, from equations 4 and 6,

$$\frac{N_T}{N_I} = \frac{N_e^* \sigma_T}{R_{Tk}} ,$$

a constant. If N_e falls by a factor of 3, N_T and the D_3 intensity fall by a factor of 9. N_I and $\tau(584)$ also fall by a factor of 9, but we still have $\tau(584) >> 1$, and the scattered intensity will be essentially constant.

This effect explains several differences between optical and EUV macrospicules. First, macrospicules are larger and longer lived in the EUV than in the visible. As the events continue to rise, they have larger volumes, lower densities, and can be seen longer in the optically deep EUV lines. Next, macrospicules are seen to fall back to the surface in the EUV, but disappear at altitude in the visible. If the events are denser when rising than falling, they may be seen in the EUV, while invisible in the visible.

One other property of EUV macrospicules is that they

are detected only in coronal holes (Bohlin et al., 1975). Explanations given for this effect (Moore et al., 1977) have been: that there is a true enhancement in the rate of macrospicules in holes over that in normal quiet regions; that macrospicule material rises higher in the open field lines of coronal holes than in the closed field of normal quiet regions; and that coronal holes are free of obscuring material (prominences). Our Big Bear data refute the first idea, as the rate is actually larger at the equator than in the polar holes. They also show no evidence of the second, as optical macrospicules look identical at all latitudes. Since EUV macrospicules are taller, however, this effect may occur above the height of our events. The Lockheed data do illustrate the third idea. On days with many equatorial prominences, the ratio of polar to equatorial macrospicule rates appeared enhanced by a factor of 4. This effect may thus be important in the EUV as well.

5. SUMMARY

Our principal results are:

1. The line center intensities of Hα and D_3 in the brightest macrospicules are $\simeq 5 \times 10^{-2}$ and $\simeq 5 \times 10^{-3}$ I_{DC}, respectively. This ratio of $H\alpha/D_3$ also holds for fainter events.
2. Macrospicule D_3 shows no intensity reduction in coronal holes, unlike the rest of the chromosphere.
3. The number of events with $I_{D_3} > I_o$ is proportional to I_o^{-1}.
4. The D_3 intensities can be explained by a model using the coronal EUV radiation to control the helium ionization. Electron densities of 1 to 2×10^{10} cm^{-3} are found for the brightest events. Other properties of the appearance of macrospicules in both D_3 and the helium EUV lines can also be understood with this model.
5. The observed ratio of $H\alpha/D_3$ intensities is not understood theoretically. Present analyses predict a ratio $\simeq 1$, rather than $\simeq 10$.

ACKNOWLEDGEMENTS

We thank the following people for their help during this investigation: Ron Moore, for extensive discussions, and Ken Marsh and Jim Mosher for other useful discussions; Alan Title for the use of the Lockheed Solar Observatory data, Dave Rust for providing American Science and Engineering data; the observers at Big Bear Solar Observatory, Gene Longbrake, Jack Klemroth, Peter Kupferman, Gary Phillis, and students John Barnard and Dave Kodama; and Jeff Nenow and Juan Sanchez for their work on the figures.

This work was supported by NASA under grant NGR 05 002 034 and NSF under grant ATM76-21132.

APPENDIX

EUV FLUX

A.1 Observed Flux

The best available integral disk EUV spectra with absolute calibrations are those of Timothy et al. (1972) and Heroux et al. (1974), from rocket flights on successive days (April 3 and 4, 1969). For the wavelength region important to helium, Timothy et al. cover λ250 to 504 Å, and Heroux et al. λ52 to 300 Å, each claiming 30% absolute accuracy. The two spectra agree in the region of overlap, λ250 to 300 Å, to within the quoted accuracy.

On the days of these observations, there were several active regions on the disk which contributed 45% of the 9.1 cm radio flux. Neupert (1967) and Chapman and Neupert (1974) have shown that the EUV and microwave fluxes are correlated. Using their formula for the relation of the EUV to the 2800 MHz flux (in SFU, 10^{-22} W-M^{-2}-Hz^{-1}),

$$F_{140\text{-}400\ \text{Å}} \propto (1 + .01\ F_{2800\ \text{MHz}})$$

we estimate that 40% of the EUV was contributed by the active regions; F_{2800} (April 3 and 4, 1969) = 183 SFU, while the quiet sun in 1976 had $F_{2800} \simeq 70$. (Note that Timothy [1976] suggests that comparison of EUV and microwave may not be straightforward, due to the difference in

emission mechanisms. His evidence is based on several independent absolute calibrations, which may be less comparable than the single instrument data used by Neupert. Also, the wavelength interval considered, 300 to 1027 Å, is dominated by emission from the chromosphere and transition zone, rather than the corona.) One can obtain a similar value for the active contribution, using the observed EUV contrast of active regions (Dupree et al., 1973) and their areas. Considering the various lines separately, we estimate that the true quiet sun flux is 0.5 the observed value for the coronal lines, and 0.8 of observed value for the He II 304 Å, which is chromospheric in origin.

In coronal holes, the coronal lines are reduced to 0.2 (Munro and Withbroe, 1972; Withbroe and Wang, 1972; Huber et al., 1974) and the 304 Å line to 0.7 (Linsky et al., 1976) of their quiet sun intensities. Although the angular variations of the coronal and 304 intensities are much different, it will be demonstrated below that the correction factors are the same, so the integrated mean intensity (observed at Earth) can be defined, for the quiet sun

$$\mathcal{F}_{I}^{Q} = 4. \times 10^{14} \text{ photons-cm}^{-2}\text{s}^{-1}\text{ster}^{-1}$$

$$\mathcal{F}_{II}^{Q} = 8. \times 10^{13} \text{ pht-cm}^{-2}\text{s}^{-1}\text{ster}^{-1}$$

and for coronal holes,

$$\mathcal{F}_I^H = 1.3 \times 10^{14} \text{ pht-cm}^{-2}\text{s}^{-1}\text{ster}^{-1}$$

$$\mathcal{F}_{II}^H = 1.6 \times 10^{13} \text{ pht-cm}^{-2}\text{s}^{-1}\text{ster}^{-1}$$

where the subscripts I and II indicate the integral is taken for $\lambda < \lambda 504$ Å and $\lambda < \lambda 228$ Å, respectively.

Integration of the spectrum over the HeI and II absorption cross-section ($R = \int I_\lambda \, a_\lambda \, d\lambda$) gives

$$R_I^Q = 1.3 \times 10^{-3} \text{ s}^{-1}\text{ster}^{-1} \qquad R_I^H = 4. \times 10^{-4} \text{ s}^{-1}\text{ster}^{-1}$$

$$R_{II}^Q = 8. \times 10^{-5} \text{ s}^{-1}\text{ster}^{-1} \qquad R_{II}^H = 1.6 \times 10^{-5} \text{ s}^{-1}\text{ster}^{-1}$$

where the cross-sections are from Allen (1963). Note that 94% of R_I is contributed at $\lambda > 228$ Å, so the HeI and II rates are essentially independent.

Mean effective wavelengths for optically thick and thin cases can also be defined,

$$\text{Thick } \lambda_k = \frac{\int \lambda \, I_\lambda \, d\lambda}{\int I_\lambda \, d\lambda} \quad ; \qquad \text{Thin } \lambda_n = \frac{\int \lambda \, a_\lambda \, I_\lambda \, d\lambda}{\int a_\lambda \, I_\lambda \, d\lambda}$$

(a_λ the absorption cross-section), which give $\lambda_k = 300$ Å, (HeI), 175 Å (HeII), and $\lambda_n = 370$ Å (HeI), 199 Å (HeII).

A.2 Limb Brightening Integrals

Mean EUV intensities measured at Earth ($\mathcal{F}$) should not

be applied directly to objects on the solar surface. Objects at Earth and on the Sun detect fluxes which are different angular integrals of the limb brightening function, depending on their cross-sections. We first consider the coronal lines, which are optically thin and strongly limb brightened. Only a diffuse component is considered; in Section 3.3 the effects of local inhomogenities are considered.

The limb brightening function of coronal EUV lines has been observed (Withbroe, 1970). It can be analytically represented quite simply by assuming that all the emission comes from the first scale height (H) of N_e^2, and the intensity in a given direction is just proportional to the distance $\ell(\theta)$ from the surface to altitude H. In that case, with μ = cos (central angle θ)

$$\frac{I(\mu)}{I_{DC}} = \frac{\ell(\mu)}{H} = \left[d^2\mu^2 + 2d + 1 \right]^{\frac{1}{2}} - d\mu; \quad d = \frac{R_\odot}{H} \quad \text{(A1)}$$

with $I(1) = I_{DC}$ by definition. (The approximation $1(\mu) = H/\mu$ is valid only for $\mu > d^{-1}$, and the integrals using that approximation are incorrect.) Equation A1 fits Withbroe's data with H = 60 Mm (d = 11.67), corresponding to a temperature of 2×10^6 °K. Although Equation A1 is obtained by assuming the lines are optically thin, the fact that it fits the data is not evidence that this assumption is true. However, Elwert (1958) has considered the case of coronal

lines with finite optical depth, and the observations are best fit by his form for $I(\mu)/I_{DC}$ with $\tau = 0$; the curve for $\tau = 0.5$ is markedly different, and does not fit as well. (Equations A1 and A2 match Elwert's $\tau = o$ solution to within 10% for all radial distances $r/R\odot$ from 0.0 to 1.05.)

The "limb spike" seen from Earth, where the path length just beyond the limb is doubled, can be treated separately, with allowance for the fact that the line of sight does not reach the surface:

$$\frac{\ell(z)}{H} = 2\left[2\ (R_\odot + H)\ (H - z)\right]^{\frac{1}{2}} \exp(-z/H) \qquad (A2)$$

where z is the minimum altitude reached by the line of sight. The limb spike then has a FWHM of approximately $z_{\frac{1}{2}} = H/2$, and a peak intensity of $2(2d + 1)^{\frac{1}{2}}\ I_{DC} = 9.9\ I_{DC}$, and contributes

$$I_{LS} = 2\pi\ r\ dr\ \ I(r) = 2\pi f_H \int_{R_\odot}^{z_{\frac{1}{2}}} I_{peak} = 0.6\ \pi\ I_{DC}$$

per $R_\odot^2$, where $f_H = 2/3$ allows for the presence of the polar coronal holes (see Vaiana et al., 1973 for a soft X-ray photograph on April 8, 1969, a few days after the EUV spectral measurements). Using Equation A1, the proper angular integrals can be done, to relate the flux at the Sun to that measured at Earth.

Case 1. Far Field (Earth Measurement)

The mean intensity observed at Earth is, with $R_\odot^2 = 1$,

$$\mathcal{J}^c = \frac{1}{\pi}\left[\int_o^1 2\pi\mu d\mu I(\mu) + I_{LS}\right] \qquad (A3)$$

$$= 2.2\ I_{DC}$$

The limb spike contributes just over 1/4 of the observed total.

Case 2. Near Field, Spherically Symmetric Particle (Atom on the Surface)

Here, the absorption cross-section is independent of angle. We will define the absorption rate to be

$$R_{abs} \equiv 2\pi\Phi_1^c\ \mathcal{J}^c\ \sigma_{abs} = \sigma_{abs}\int_o^1 2\pi\ I(\mu)\ d\mu \qquad (A4)$$

$$= 2\pi\sigma_{abs} \times 2.2\ I_{DC}$$

and therefore $\Phi_1^c = 1.0$. Although the angular integral is larger than in Case 1, the presence of the limb spike in the far field happens to just make up the difference.

Case 3. Near Field, Totally Absorbing Vertical Cylinder (Macrospicule)

In this case, the absorption cross-section is a function of angle; for a vertical cylinder of radius r and height h, with $r << h$, so that the area of the top of the cylinder

may be ignored, $\sigma(\theta) = 2\ (r+L)h \sin(\theta)$. We also assume that $h << H$, which is reasonable for the D_3 emitting region of the macrospicule; the cylinder is then treated as a microscopic particle, with the effects of its finite extent being negligible. Again, defining the total absorption rate,

$$R_{abs} = 2\pi\Phi_2^c\ \mathcal{F}^c\ A_s = \int_0^{\frac{\pi}{2}} 2\pi\sigma(\theta)\ I(\theta) \sin(\theta)\, d\theta \quad (A5)$$

$$= 4\pi\ (r+L)\ h \times 1.9\ I_{DC}\ .$$

Because the absorption cross-section varies with angle, the total surface area A_s is used for convenience in defining the rate; this leads to $\Phi_2^c = 0.27$.

The He II 304 Å line limb variation in unknown; since the line is optically thick, we will assume that it has no variation, to first order, $I(\mu) = I_{DC}$. Case 1 collapses to $\mathcal{F}^H = I_{DC}$, Case 2 to $\Phi_1^H = 1.0$, and Case 3 to $\Phi_2^H = 0.25$. As these values of Φ are nearly equal to the coronal values, Equations A3 through A5 for He and coronal lines can be summed, using $\Phi_1 = 1.0$, $\Phi_2 = 0.26$. Since we are considering objects very near the surface, all the angular integrals cover 2π solid angle, whether looking up at the corona or down at the surface.

REFERENCES

Allen, C.W.: 1963, Astrophysical Quantities, p. 92, Athlone Press, London.

Athay, R.G.: 1972, Radiation Transport in Spectral Lines, p. 27, D. Reidel Publ. Co., Dordrecht, Holland.

Beckers, J.M.: 1972, Ann. Rev. Astron. Astrophys., 10, 73.

Bohlin, J.D., Vogel, S.N., Purcell, J.D., Sheeley, N.R., Tousey, R. and Van Hoosier, M.E.: 1975, Ap. J., 197, L133.

Burgess, A.: 1958, M.N.R.A.S., 118, 477.

Burgess, A. and Seaton, M.J.: 1960, M.N.R.A.S., 121, 471.

Chapman, R.D. and Neupert, W.M.: 1974, J. Geophys. Res., 79, 4138.

Davis, J.M., Golub, L., and Krieger, A.S.: 1977, Ap.J., 214, L141.

Doschek, G.A., Behring, W.E., and Feldman, U.: 1974, Ap. J., 190, L141.

Dupree, A.K., Huber, M.C.E., Noyes, R.W., Parkinson, W.H., Reeves, E.M. and Withbroe, G.L.: 1973, Ap. J., 182, 321.

Elwert, G.: 1958, J. Atm. Terr. Phys., 12, 187.

Giovanelli, R.G.: 1967, Aust. J. Phys., 20, 81.

Glackin, D.L.: 1975, Solar Phys., 41, 115.

Goldberg, L.: 1939, Ap. J., 89, 673.

Godoli, G. and Mazzucconi, F.: 1967, Ap. J., 147, 1131.

Golub, L., Krieger, A.S., Silk, J.K., Timothy, A.F. and Vaiana, G.S.: 1974, Ap. J., 189, L93.

Harvey, K.L. and Martin, S.F.: 1973, Solar Phys., 32, 389.

Harvey, K.L., Harvey, J.W. and Martin, S.F.: 1975, Solar Phys., 40, 87.

Harvey, J.W., Krieger, A.S., Timothy, A.F. and Vaiana,G.S.: 1975b, B.A.A.S., 7, 358.

Heroux, L., Cohen, M. and Higgins, J.E.: 1974, J. Geophys. Res., 79, 5237.

Hirayama, T.: 1971, Solar Phys., 19, 384.

Huber, M.C.E., Foukal, P.V., Noyes, R.W., Reeves, E.M., Schmahl, E.J., Timothy, J.G., Vernazza, J.E., and Withbroe, G.L.: 1974, Ap. J., 194, L115.

Hyder, C.L. and Lites, B.W.: 1970, Solar Phys., 14, 147.

LaBonte, B.J.: 1977, Solar Phys., 53, 369.

Labs, D. and Neckel, H.: 1968, Z. f. Astrophys., 69, 1.

Linsky, J.L., Glackin, D.L., Chapman, R.D., Neupert,W.M., and Thomas, R.J.: 1976, Ap. J., 203, 509.

Livshits, M.A.: 1976, Sov. Astron., 19, 587.

Livshits, M.A., Akimov, L.A., Belkina, I.L. and Dyatel, N.P.: 1976, Solar Phys., 49, 315.

Marsh, K.A.: 1977, Big Bear Solar Obs. preprint 0166.

Martin, S.F. and Harvey, K.L.: 1976, A.F. Geophys. Lab. Report, AFGL-TR-76-0255

Moore, R.L., Tang, F., Bohlin, J.D. and Golub, L.: 1977, Ap. J., 218, 286.

Munro, R.H. and Withbroe, G.L.: 1972, Ap. J., 176, 511.

Neupert, W.M.: 1967, Solar Phys., 2, 294.

Noyes, R.W., Foukal, P.V., Huber, M.C.E., Reeves, E.M., Schmahl, E.J., Timothy, J.G., Vernazza, J.E. and Withbroe, G.L.: 1974, in S.R. Kane (ed.), Solar Gamma-, X- and EUV Radiation, IAU Symp. 68, 3.

Pierce, A.K. and Waddell, J.H.: 1961, Mem. R.A.S., 68,69.

Pope, T. and Schoolman, S.: 1975, Solar Phys., 42, 471.

Pottasch, S.R. and Thomas, R.N.: 1959, Ap. J., 130, 941.

Ramsey, H. and Mosher, J.: 1976, preprint.

Ramsey, H.H., Martin, S.F. and Harvey, K.L.: 1975, Lockheed Final Report, AFCRL-TR-75-0355

Roberts, W.O.: 1945, Ap. J., 101, 136

Rompolt, B.: 1967, Acta Astron., 17, 329

Stellmacher, G.: 1972, Solar Phys., 25, 104

Timothy, J.G.: 1976, preprint to appear in O.R. White, J.A. Eddy and D.F. Heath (eds.), The Physical Output of the Sun and its Variation.

Timothy, A.F., Timothy, J.G., Willmore, A.P. and Wager, J.H.: 1972, J. Atm. Terr. Phys., 34, 969.

Tousey, R., Milone, E.F., Purcell, J.D., Palm Schneider, W., Tilford, S.G.: 1974, An Atlas of the Solar Ultraviolet Spectrum Between 2226 and 2992 Angstroms, NRL Report 7788.

Vaiana, G.S., Krieger, A.S. and Timothy, A.F.: 1973, Solar Phys., 32, 81.

White, O.R.: 1962, Ap. J. Supl., 7, 333.

Withbroe, G.L.: 1970, Solar Phys., 11, 42.

Withbroe, G.L. and Wang, Y.: 1972, Solar Phys., 27, 394.

Withbroe, G.L., Jaffe, D.T., Foukal, P.V., Huber, M.C.E., Noyes, R.W., Reeves, E.M., Schmahl, E.J., Timothy, J.G. and Vernazza, J.E.: 1976, Ap. J., 203, 528.

Zirin, H.: 1975, Ap. J., 199, L63.

TABLE 1

Hα AND D3 MACROSPICULE INTENSITIES

Date and Time (UT)	Latitude	Height (km)[1] D3 (Hα)	I_{D3}/I_{DC}[2]	$I_{H\alpha}/I_{DC}$[3]
9/20/75 1853	81°S	3000 (3500, 5000)	4×10^{-3}	8×10^{-2} (-1.0Å) 3×10^{-2} (+0.5Å)
9/20/75 1903	80°S	3000 (3500, 5000)	6×10^{-3}	6×10^{-2} (-1.0Å) 3×10^{-2} (+0.5Å)
9/27/75 2038	38°N	4000 (6000)	2×10^{-3}	5×10^{-2} (0.0)
10/2/75 1702	31°N	5000 (6000)	6×10^{-3}	6×10^{-2} (0.0)

1) Height of intensity measurement.

2) I_{DC} is the specific intensity of the continuum at disk center.

3) Number in parentheses is the wavelength relative to line center.

Table 2

MACROSPICULE Hα AND D_3 INTENSITIES

$I_{H\alpha}$	I_{D_3}				
	0	1	2	3	Total
3	0(0)	2(0)	3(4)	0(1)	5(5)
2	4(1)	15(6)	4(4)	0(1)	23(12)
1	24(12)	8(0)	3(0)	0(0)	35(12)
Total:	28(13)	25(6)	10(8)	0(2)	63(29)

Entries are the number of events seen in both polar (equatorial) quadrants.

Visual intensity scales.

Events with $I_{D_3} = 0$ were invisible in D_3.

Table 3

D_3 MACROSPICULE DENSITIES

Date and Time (UT)	Radius [1] (km)	D_3 Optical Depth [2]	$N_2{}^3P$ (cm^{-3})	$N_e(N_e^*)$ [3] (cm^{-3})	$N_e(\infty)$ [4] (cm^{-3})
9/20/75 1853	1400	1.4×10^{-2}	200	2.4×10^{10}	1.4×10^{10}
9/20/75 1903	1300	2.1×10^{-2}	320	$\geq 3.6 \times 10^{10}$	1.7×10^{10}
9/27/75 2038	1300	6.1×10^{-3}	100	1.1×10^{10}	9.8×10^{9}
10/2/75 1701	2600	2.1×10^{-2}	160	1.5×10^{10}	1.3×10^{10}

(1) At time of intensity measurements.

(2) Assuming 0.4 Å Doppler linewidth.

(3) With N_e^* as appropriate for event location.

(4) With $N_e^* \rightarrow \infty$

FIGURE CAPTIONS

Figure 1:

Macrospicule in Hα line center. Event was located at 31° north latitude. The apparent limb is the top of the spicules, about 5000 km above the continuum limb.

The arrow marks the initial appearance of the event; substantial motion along the limb occurred before the vertical extension. Fine structure down to 0.5 arcsecond is visible. The vertical structures within the macrospicule do not fan out with height, as in spike surges, but lean toward each other. At 2041 UT, the structure looks like a closed loop. By 2043, diffuse material has been spread over a large volume. He I D3 emission was detected in this event.

Figure 2:

Macrospicule in Hα-1Å and D3. Event was located at 80° south latitude; the polar coronal hole boundary this day was at 65°. Times (UT) are (a) 1859:58; (b) 1902:12; (c) 1903:22; (d) 1904:51; (e) 1908:19.

D3 emission peaks in the lowest, brightest part of the Hα structure, not in a sheath surrounding the Hα. The Hα object shows much fine structure, and at (b) appears as a faint loop. Simultaneous film at

Hα + 0.5Å shows similar gross evolution, but different fine structure, implying Doppler lineshifts which are consistent with the apparent transverse velocities.

Figure 3:

Macrospicule on the disk in Hα line center. A filament connecting a bipolar magnetic ephemeral region to nearby fields darkens, erupts into loops, and disappears. The ephemeral region had a total lifetime of 25 hours, but lasted only 2 hours after this event. No D_3 absorption or emission was detected in this event. The location was 4° south, 12° east. Times (UT) are,

top, left to right: 1555, 1617, 1622

bottom, left to right: 1625, 1628, 1636.

Figure 4:

Surge-like macrospicule on the disk in Hα. Arch fibrils (A) connect the site of the macrospicule (B) to nearby magnetic areas, demonstrating the mixture of magnetic polarities. No D_3 was detected in this event. Event location was 0° north, 25° east. Times (UT) are,

top, left to right: 2301, 2306, 2308

bottom, left to right: 2310, 2312.

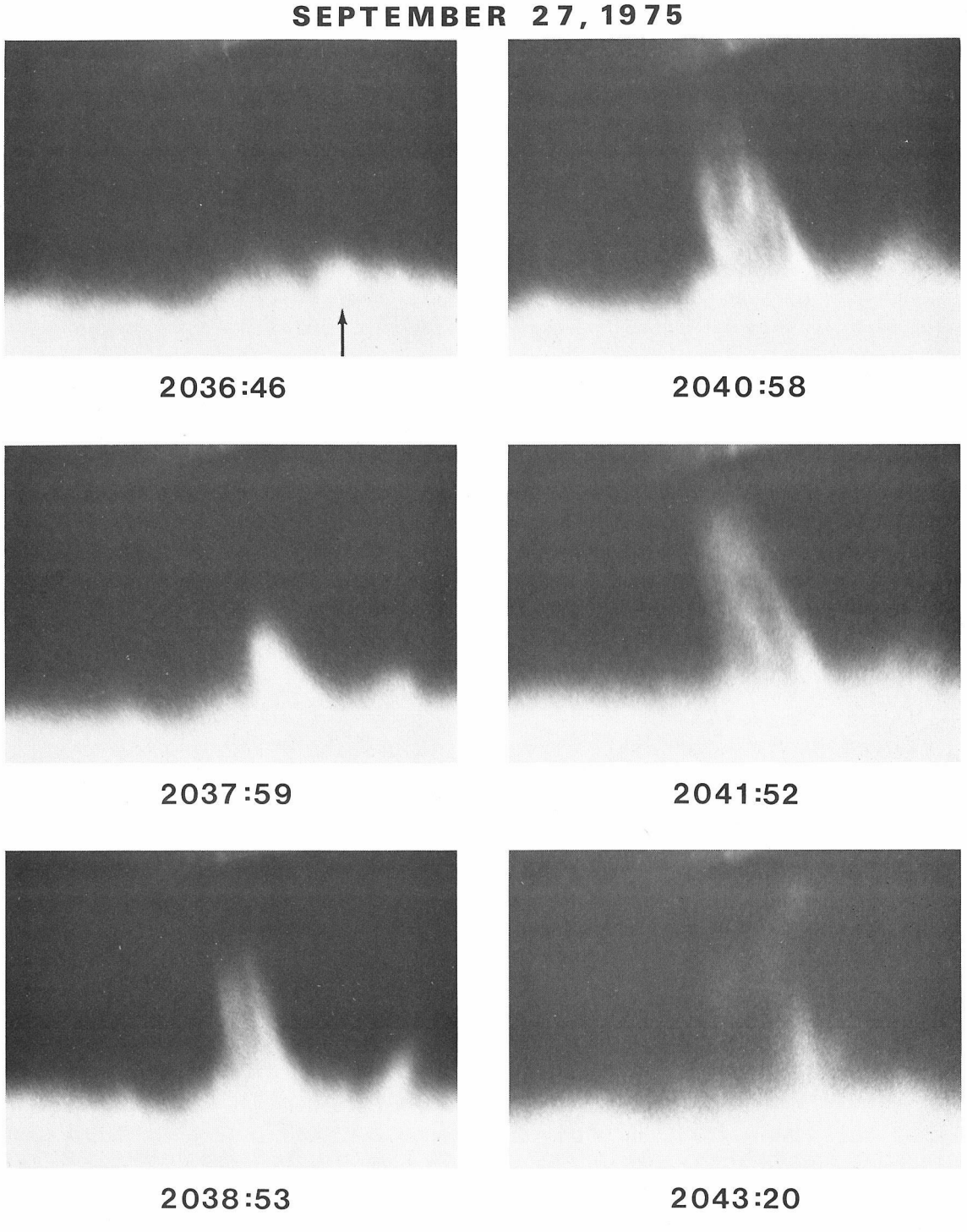
SEPTEMBER 27, 1975
2036:46
2040:58
2037:59
2041:52
2038:53
2043:20
20"

Figure 1

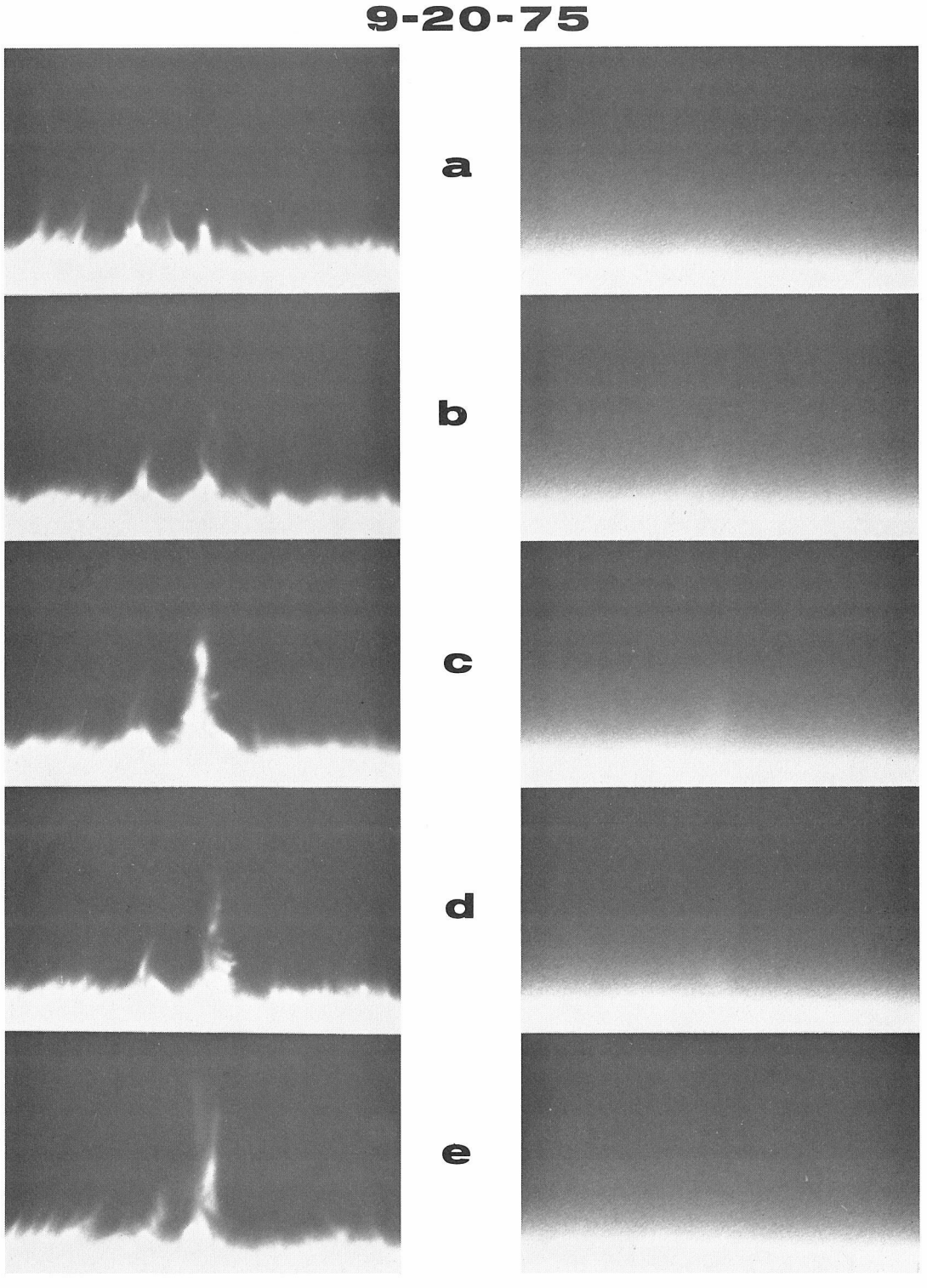

Figure 2

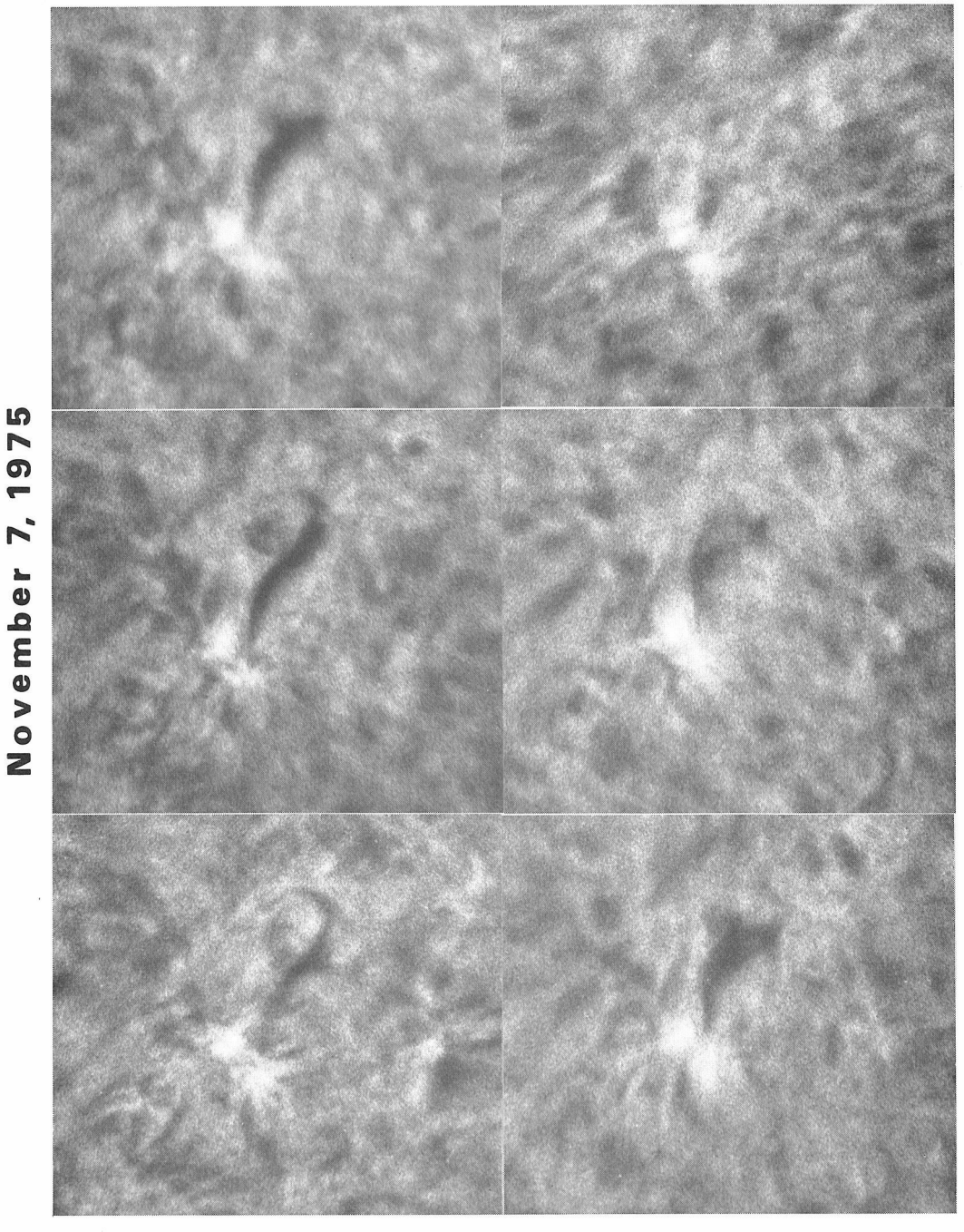

Figure 3

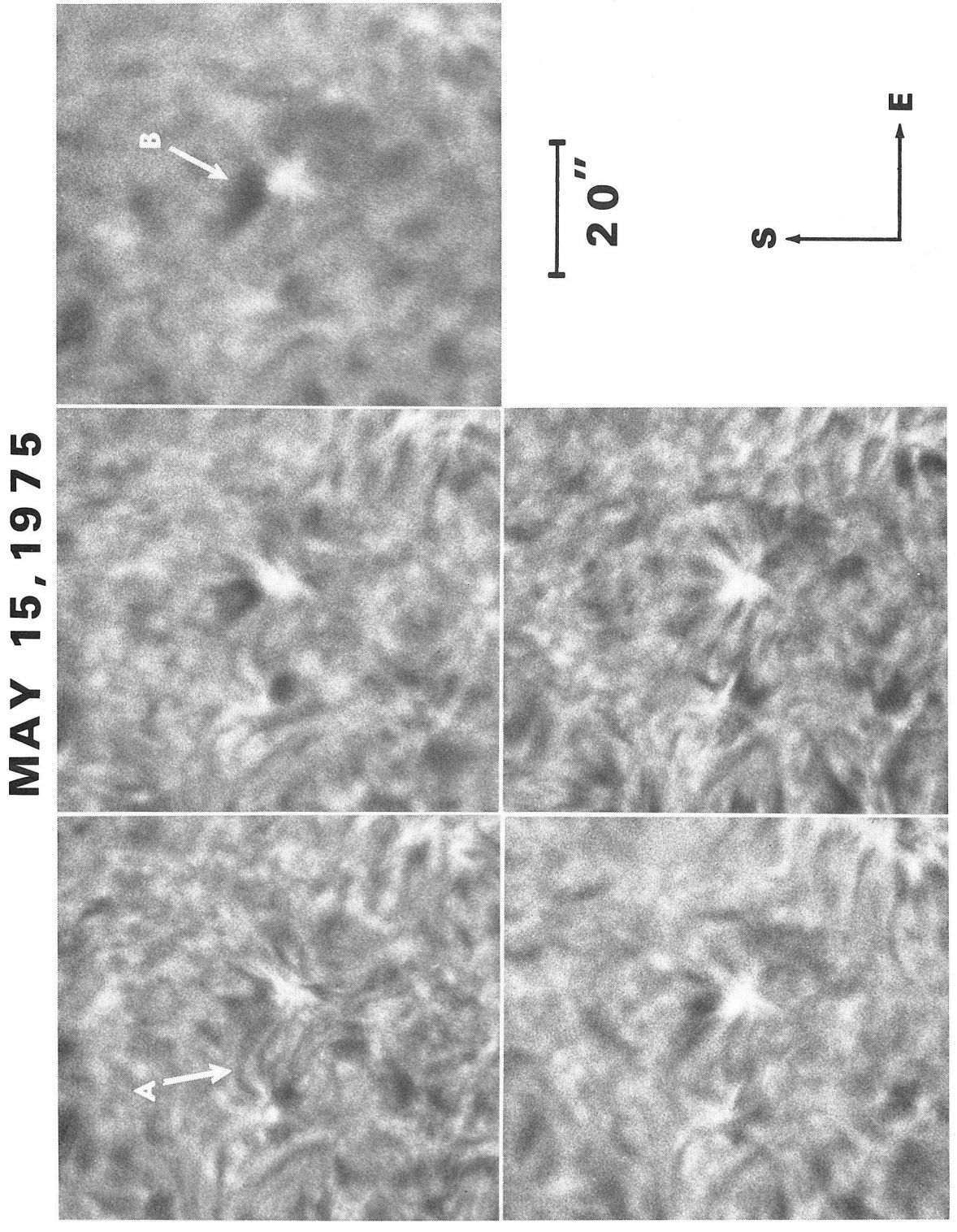

Figure 4

CHAPTER 4

POLAR FLARES WITH D_3 EMISSION: NOVEMBER 15, 1974

Appears as BBSO Preprint No. 0170

ABSTRACT

A series of flares showing He I D_3 in emission on the disk have been observed. Remarkably, the flare location was 79° south latitude. Comparison of the flare properties is made with calculations of thick target electron beam models, to estimate the flare energy.

the Big Bear Solar Observatory, with a Zeiss Universal Birefringent Filter, 0.19 Å FWHM at 5876 Å. A time lapse movie was made, with 10 second intervals between photographs. We also have full disk Hα filtergrams, at 20 second intervals, from the 22 cm telescope. Because the 25 cm is chromatic, its image scale varies with wavelength; the region of the D_3 events therefore was not contained within the field of its Hα camera. The 25 cm Hα film does show that the seeing blue circle at the time of the observations was approximately 2 arc seconds.

2.2 Flare Region

A region near the south pole was observed on November 15, 1974 from 2041 to 2204 UT. The heliographic location of the flares was 79° south, 50° east. Six episodes of D_3 activity were detected. At all other times no D_3 emission nor absorption was seen, with a contrast threshold of 2 to 3%. A series of deep exposures taken earlier on the 15th prove that the flare site was inside the south polar coronal hole. The normal D_3 limb band (Pope and Schoolman, 1975; Zirin, 1975) was seen at other positions around the limb, but was absent at the location of the flares.

No facular region is visible at the flare location on the Mt. Wilson daily continuum photograph or K-line spectroheliogram for the 15th. A search of these data as well as the Mt. Wilson magnetograms and the Big Bear full disk Hα

filtergrams shows no trace of activity during succeeding days as the site rotated onto the disk. The region producing the flares must have been small and short lived.

2.3 D_3 Morphology

The flare activity is summarized in Table 1 and illustrated in Figure 1. The first event, at 2050:38, appeared as a knot of emission just inside the limb, and was seen on only one movie frame. The second event, 2110:27, was also seen on only one frame, but the emission was weaker, and a vertical feature was visible extending above the limb. The third event was seen on two frames, at 2119:16 as an emission knot, and 10 seconds later as a vertical feature. The last three events were separate parts of complex activity during the time 2124:46 to 2126:46. The fourth event showed emission on six consecutive frames, with a vertical feature on the last one. There were then two frames with no detectable D_3, followed by the fifth event, lasting three frames, with a vertical feature during the second one. There was one more frame with no D_3, and then the sixth event, again an emission knot seen on only one frame. No further activity is seen after 2126:46.

The intensity evolution of the knots was even more rapid than this simple description indicates. We will show below that on the first photograph of each of the five events which appear as an emission knot, the knot had a peak

intensity which was remarkably constant. They were never seen with an intensity which was significantly lower. Since we observe five such onsets, each beginning not more than 10 seconds before they were photographed, the true risetime to peak intensity was probably much less than 10 seconds. The decay in intensity, in at least three cases, was equally abrupt.

All four appearances of vertical features are shown in the split frames of Figure 1. The vertical features extend 4 to 8" above the limb (Table 1). Assuming their base to be 3" inside the limb, they have total projected heights of 5 to 8 Mm. We cannot determine from the D_3 data whether they are surges or small loops. The failure to detect Hα (see Section 2.4) is more easily explained if the features are loops, and thus restricted in height. The occurrence of the features at the end of events, after a period of emission, suggests their appearance is causally related to the disappearance of emission.

2.4 Hα

Our Hα film shows no activity at the location and times of the D_3 events. No emission is seen on the disk, and no vertical features are seen extending above the limb. This suggests that any Hα emission present is either very weak or, more likely, occurs at depth in the chromosphere, and is obscured at this limb distance by higher lying material

along the line of sight. The latter explanation is not as convincing as one would like because the filter on the 22 cm telescope, being of Fabry-Perot design, transmits some light in the line wings, and brilliant Hα emission might be detected even when the line center is invisible. The vertical features would be indetectable if they were the same height in Hα as in D3, and did not have a large Hα contrast.

2.5 Rate of Occurrence

The events of November 15, 1974 were not only unusual, but unique. A search of Big Bear D_3 films from 1974 and 1975 revealed no other rapid emission or absorption events in quiet regions, either at the limb or on the disk. Considering the area and time coverage, an upper limit on the rate of such events can be set at 3 per day on the entire sun, during those years.

It is important to note that these flares are morphologically identical to events seen frequently in active regions. Small flare knots with 100% intensity modulation on 10 second time scales are observed in D_3 (LaBonte, in preparation) and higher Balmer lines (Zirin and Tanaka, 1973). Even at low as Hβ, flare knots are observed with risetimes, from invisibility to peak intensity, of less than 10 seconds. In active regions however, such events appear exclusively within, or in contact with, sunspots, or as the initial phase of a large flare. What makes the flares of

November 15, 1974 unique is the location of this type of event in the polar regions, where sunspot strength magnetic fields and large flares are absent.

2.6 Photometry

The intensities of the D_3 events have been measured, to help discriminate among different mechanisms for producing the emission. Examples of the intensity structure of the knots are shown in Figure 2. A strip 3.5" wide was scanned, (with data samples taken at 1" intervals), along a solar radius through the center of the knots (Figure 2a), then parallel to and centered 4" inside the limb (Figure 2b).

The radial profiles of nearby quiet regions were fitted to a limb darkening law (Pierce and Waddell, 1961)

$$I(\mu) = a_\lambda + b_\lambda \mu + c_\lambda [1 - \mu \ln(1 + \mu^{-1})], \quad \mu = \cos\theta \qquad (1)$$

smeared with a gaussian function of 1" width. θ is the central angle, and at 5876 Å, $a_\lambda = 0.771$, $b_\lambda = 0.394$, and $c_\lambda = 0.538$. The fit determines the characteristic curve of the film and calibrates the intensities in units of I_{DC}, the specific intensity of the continuum at disk center, at D_3. From Labs and Neckel (1968),

$$I_{DC} = 3.36 \times 10^6 \text{ ergs cm}^{-2} \text{ S}^{-1} \text{ ster}^{-1} \text{ Å}^{-1}.$$

The flare intensities in Figure 2a are not corrected for the effects of the filter and line profiles (see Section 2.7).

2.6.1 Intensity Structure

The radial structure of the flare knot (Figure 2a) changes with time, the largest variation occuring near the limb, where the knot sometimes protrudes above the limb, and and other times does not. The central part of the knot, between 3 and 6" from the limb, shows less variation and the peak intensity of the flare is contained in this region at all times. The peak intensity of the knot was remarkably constant, with a value of $0.448 \pm 0.008\ I_{DC}$; the standard error is not significantly different from that of the individual data points. This intensity was reached at all times in all events, except when a vertical feature was present at the end of an event. The peak intensity then had a value between 0.40 and $0.43\ I_{DC}$, and occurred between 2 and 3" from the limb. The vertical features themselves were fainter; the brightest one, at 2125:36, had an intensity of $0.20\ I_{DC}$.

No tangential shifts in the flare location can be seen, with a limit of 2 to 3" set by the absence of fiducial markers. The tangential contrast profiles in Figure 2b have therefore been centered on a single scale. The tangential profiles have much smaller relative variation than the radial profiles at the same times. A kernel of uniform intensity 5" in diameter, a steep falloff to 60% of peak contrast, and a triangular halo of 20" diameter are the

characteristics of the flare structure. Absence of large tangential differences in structure implies the radial variations are caused by changes in the vertical structure. The elongation of the flare knots in the tangential direction (for example, Figure 1, 2050:38 UT) also implies strong vertical stratification.

2.7 Corrected Intensities

Line center and line integral emission intensities can be derived from the observed flare intensity by correcting for the filter and line profiles. Unfortunately, the exact shape and wavelength position of the D_3 emission line are unknown. We will assume the line is gaussian, with 1/e - width of 0.4 Å, and with no wavelength shift with respect to the nonflare line. The assumed width is that found for D_3 in plages (LaBonte, 1977). There are no spectral observations of D_3 in small flares; in large flares the linewidth is larger than 0.4 Å (Jefferies et al., 1959; Smith, 1963). and may show self-reversal (Steshenko and Khokhlova, 1960; Kvicala et al., 1961) or multiple components (Krat and Sobolev, 1960). In impulsive flares, D_3 can have large redshifts (Ramsey et al., 1975). Values derived using our assumption may therefore easily be underestimates. Because the (assumed) linewidth is much larger than the filter width, the corrections are small for line center intensities, but large for line integral intensities.

To correct the line center intensities of Figure 2a, one uses

$$I_F^C = I_Q + C_I\ (I_F - I_Q) \quad ,$$

where I_Q, I_F are the observed quiet and flare intensities at a given radial position. For our choice of linewidth, and the known filter properties, $C_I = 1.22$.

As stated above, the peak flare knot intensity was nearly constant at all times. Corrected for line and filter profiles, the value is $I_p = 0.454\ I_{DC}$. This will be used to set a lower limit on the source function in the flares.

2.7.1 Optical Depth

A minimum line of sight optical depth can also be determined for the flare knots whenever they protrude above the limb. Assuming the flare optical depth τ and source function S are constant across the limb,

$$\tau = -\ln(\Delta I_{flare}/\Delta I_{quiet}) \qquad (2)$$

where ΔI is the change in intensity across the limb. Correcting the radial profiles of Figure 2a, we find $\tau(2125{:}16) = 1.4$, $\tau(2126{:}46) > 4$, and $S \simeq 0.41$ at both times. Since the flare knots vary most strongly at the limb, it is probable that the optical depth is larger in the more constant kernel, 2 to 7" inside the limb.

2.7.2 Total D_3 Emission

The total D_3 emission can be found, assuming an optically thick kernel, optically thin halo, and isotropic emission. The total varies with time, from 0.5 to 1.5 x 10^{24} ergs-s^{-1}, into 2π steradians; the net (emission minus absorption) toward the photosphere being approximately zero. The kernel contributes about 2/3 of the total.

3. COMPARISON WITH NORMAL POLAR ACTIVITY

Activity in the polar regions of the sun normally occurs as macrospicules. These are small events, generally surges or loop eruptions, occasionally with flare brightening. They are observed in extreme-ultraviolet (EUV) emission lines (Bohlin et al., 1975; Withbroe et al., 1976) and soft x-rays (Golub et al., 1974) as well as in the visible (Godoli and Mazzucconi, 1967; Ramsey and Mosher, 1976; Moore et al., 1977). Their properties as observed in Hα and D_3 are given by Ramsey et al. (1975) and LaBonte (1978a).

A typical macrospicule has the appearance of a vertical cylinder or loop approximately 10 Mm in height and 2 Mm in diameter, with a lifetime of about 10 minutes; all these parameters can differ by more than factors of 2 from event to event. Measured D_3 emission intensities are $\simeq 3 \times 10^{-3}$ I_{DC}; the D_3 emission is controlled by the radiation fields (coronal and photospheric) external to the macrospicule.

(Coronal EUV photons with $\lambda < 504\text{Å}$ photoionize He I to He II, which populates the metastable triplet terms by recombination; relative triplet populations are fixed by scattering of the photospheric continuum). Electron densities are $\approx 10^{10}$ cm^{-3}. Event total energies, which are largely work done against gravity, are a few times 10^{26} ergs.

The number of macrospicules seen increases greatly as the detection sensitivity is increased. Because this sensitivity differs in the various spectral regions, different rates of macrospicules occurrence are generally given. For example, $\approx$ 2000 macrospicules per day on the entire sun could be seen in Hα (LaBonte, 1978a), while only 50 to 100 produce detectable soft X-ray flares (Golub et al, 1974).

It is clear that the flares of November 15, 1974 are significantly different from the normal polar activity in their structure, evolution (timescales $t_F \approx 10^{-2}\ t_M$), rate of occurrence, and intensity of D_3 emission ($I_F \approx 10^2\ I_M$). Since D_3 emission strength empirically acts as an indicator of energy density, it is implied that events of much larger energy than have been previously recognized can occur in the polar regions. Indeed, the D_3 emission alone equalled the energy of a macrospicule, whose line emission is insignificant. We will attempt to determine the total energy of the flares. This will require knowledge of the mechanism producing the D_3 emission, and a model of the flares in which

this mechanism is causally related to the total energy.

4. FLARE MODELS

4.1 Radiative D_3 Excitation

The November 15 flares may just be "supermacrospicules"; abnormally dense, and perhaps, with high EUV self emission. D_3 would still be radiatively controlled. There are two reasons which lead us to consider this possibility. First, the peak intensity of the flares is quite constant at all times, which suggests that it may be limited by some process not directly connected with the flare, e.g., the photospheric continuum. Second, there are lines (from rare earth elements) which appear in emission, in the few arcseconds just inside the limb, even in the quiet sun, and are radiatively controlled (Canfield, 1969; 1971). The appearance of "emission" in the flares might be just an artifact of the continuum limb darkening. Although such processes would operate in D_3 in the quiet sun, the emission might be undetectable in the presence of scattered light and seeing due to the low line opacity. It can be shown, however, that D_3 must be collisionally excited. Scattering alone cannot explain the observed flare brightness.

Consider first the case of small vertical D_3 optical depth, so that each atom sees the surface unobscured. When the collisional rates are negligible, the source function

(S_o) is just equal to the mean intensity J. Considering only processes in the line, and using the limb darkening law of Equation 1, an atom near the surface will have

$$S_o = J_o = \frac{1}{4\pi} \int_0^1 2\pi\, I(\mu)\, d\mu = \tfrac{1}{2}a + \tfrac{1}{4}(b + c) = 0.35\ I_{DC}.$$

When the helium occurs in a thin horizontal layer, the observed intensity near the limb can be a large fraction of this value, as the line of sight optical depth is much larger than the vertical depth. This is the case in the quiet sun D_3 limb band (LaBonte, 1977).

A second process which can effect the source function in pure scattering is interlocking with (cycling through) other bound levels in the triplet system. (A third process, radiative cascade, or interlocking through the continuum, is unimportant here because the rates to and from the continuum are much smaller than those in the lines). It is this effect which controls the rare earth emission lines (Canfield, 1971). To investigate the impact of interlocking on D_3, a model triplet system was studied, with 7 bound terms (2S, 2P, 3S, 3P, 3D, 4, 5) and continuum. When all lines are optically thin, there is a 7% increase in S_o over the value obtained using only 2 levels, as electrons are cycled from the lower level of D_3(2P) to the upper (3D). This cycle raises the small depth value to $S_o = 0.37\ I_{DC}$.

This value for S_o is far short of the observed peak

flare intensities of 0.45 I_{DC}. Indeed, all of the flare emission more than 2" inside the limb, including the flare halo, is brighter than S_o. Random errors in the data are only $\approx +0.01\ I_{DC}$, and systematic error in the intensity scale is avoided by referring the intensities to the continuum. (There is no contamination from a nonflare D_3 line, since its central depth in a coronal hole must be < 0.2%). Further, the flares are not confined to a thin layer, but have some thickness; the line of sight optical depth should be only 2 to 3 times the vertical depth. Using the measured values, this implies a vertical depth of 0.5 to 1 or larger, and the source function would be reduced from the small optical depth case. We conclude that the observed D_3 intensity can only be produced in the presence of significant collisional excitation.

4.2 "Supermacrospicule" Model

One might still imagine that collisional excitation could occur in a sufficiently hot and dense "supermacrospicule", although a mechanism for producing such an object is unknown. A crude estimate of the consequences of this model can be made, in terms of the total energy of the flares. The observed intensity is approximately 25% larger than the pure scattering source function; the collisional excitation rate should thus be of order 25% of the

photoexcitation rate, ($S_{D_3} \propto \frac{N_{3D}}{N_{2_P}}$) or $N_e{}^c\, C_{ex} = 2 \times 10^5\,s^{-1}$, leaving aside optical depth effects. The excitation coefficient (C_{ex}) can be calculated (see Appendix for source), and a value for the electron density ($N_e{}^c$) as a function of temperature can be derived (Table 2).

The energy content is the ionization plus thermal energy times the volume, $N_e^c\,(R_H + 3\ kT)V$ (R_H = 1 Rydberg), and the flare kernel is taken to be a disk of 5" diameter and 2 Mm thickness, $V = 2 \times 10^{25}\ cm^3$. This energy must be provided not just once, but at least once per distinct event, or 6 times; this represents a firm lower limit on the energy for the flares, and corresponds to 20 to 200 times a macrospicule energy, depending upon the temperature. Now, both the recombination and optically thin radiative cooling times of plasmas with these temperatures and densities are very short, $\lesssim$ 1 second. Since the flare emission lasts for a total of about 100 seconds, an upper limit on the flare energy is thus 100 times the energy content, or 300 to 3000 times a macrospicule energy.

In fact the flares are certainly not optically thin at many important wavelengths, and the cooling rate (and effective recombination rate) will be reduced appropriately. However, there is some radiative loss (leaving aside any conductive or convective losses), so the energy must be replaced more than once per event. This very crude analysis

indicates that the flares must be considerably more energetic than normal polar activity, but is unsatisfactory in having a large range between the upper and lower limits. In addition, no judgment is possible in choosing which temperature-density regime is most appropriate, or, as is certainly the case, which mixture of temperatures and densities. (However, by demanding that the observed D_3 optical depth be obtained in the observed path length, very hot models can be ruled out; for example, a strong X-ray bright point flare, with very high density, few million degree plasma, and little or no cool material. In that case, the helium present is overwhelmingly He III, and the D_3 opacity is too small).

4.3 Thick Target Model

To set better limits on the flare energy observationally would require more complete spectral data, which is not available. However, if the basic processes by which the flare energy are released were known, along with the manner in which they determine the energy balance in the D_3 emitting region, model calculations of the physical system could be compared with the observed D_3 phenomena. We believe the character of the flare structure and evolution indicate a plausible model for the energy mechanisms.

In the D_3 region the heat source must be able to turn on and off in times less than 10 seconds. Yet, heating

must be provided continuously for periods as long as a minute. To cover the flare radius of 10" in 10 seconds, a propagation velocity of more than 700 km s^{-1} is necessary (unless one considers the entire flare to be one of a larger magnetic structure, which conflicts with the failure to observe Hα structures). If is difficult to understand how shocks (Nakagawa et al., 1973), thermal conduction (Shmeleva and Syrovatskii, 1973; see Brown's (1974) comments), plasma pinches (Colgate et al., 1977) or any of several other models could meet all these criteria.

However, the morphologic similarity to the August 1972 optical flashes (Zirin and Tanaka, 1973) suggests a similarity of physical processes. Those events were simultaneous with hard X-ray emission, also having short time scale intensity modulation, and the optical and X-ray observations were shown to be consistent with the thick target model of X-ray emission. A flux of kilo-electron-volt electrons is accelerated by magnetic reconnection processes (Baum and Bratenahl, 1976) at altitude, with X-ray and optical emissions produced as the electrons impact the denser chromosphere (Hudson 1972). Rise and decay times, event duration, and propagation velocity constraints are all met, as determined by observation of the properties of hard X-ray bursts (Kane, 1974). This is the model which we adopt. We will compare the observed D_3 properties of the November 15, 1974

flares to the predicted properties of model flares, constructed under the thick target assumption, with the intent of estimating the total flare energy and characteristics of the D_3 emitting region.

The validity of the thick target model in the particular case of the November 15, 1974 event cannot be tested directly, as no indicators of high energy electrons were observed. No hard X-ray, microwave, or Type III radio burst was reported. However, a small total energy, absence of sunspot strength magnetic fields, and apparently closed field configuration all would contribute to the inability to detect these flares.

Flare atmospheres for the thick target model have been calculated by Brown (1973). Errors in Brown's electron energy input and radiative loss equations have been pointed out by Lin and Hudson (1976) and Canfield (1974). Also, Brown considered longlived flares, allowing the density profile of the atmosphere to adjust to the increasing temperature; this is unimportant in shortlived flares (Bessey and Kuperus, 1970).

To solve these problems new models of shortlived thick target flares have been calculated (LaBonte, 1978b). Energy input by collisional degradation of the electron flux is balanced by thermal radiative losses from hydrogen and metals, with account taken of optical depth effects.

Equilibrium between heating and cooling determines the variation of temperature and hydrogen ionization with depth; the total density profile remains that of the preflare chromosphere, due to the short flare duration. In fact, the flare atmosphere is radiatively stable (capable of equilibrium) only up to some critical altitude. Above this level, decreasing density and increasing temperature (Cox and Tucker, 1969) reduces the radiative efficiency to the point that the electron energy input cannot be balanced, and the atmosphere must continually heat and expand into the corona.

For comparison with the observations, He I line emission from a set of these models was computed. The He I populations and radiation fields were determined, given the model temperature and density distributions. Several of the model results are shown in Table 3. Details of the helium calculations and additional results are given in the Appendix.

The flare models are characterized by F_{20}, the energy input to the chromosphere, in ergs cm^{-2}-s^{-1}, by electrons with energies $\geq$ 20 keV. Also listed is F_{rad}, the energy input to the entire radiatively stable part of the atmosphere. F_{rad} differs from F_{20} whenever the critical height for radiative stability differs from the penetration depth of 20 keV electrons. For most of the models, the critical height lies above the 20 keV depth, and $F_{rad} > F_{20}$, by the

inclusion of lower energy electrons. For all models used here, the predicted hard X-ray photon flux at Earth, $A\ E^{-\gamma}$ $(cm^2\text{-}s\text{-}keV)^{-1}$, has the same spectral index, $\gamma = 4$; the intensity $A = 1.45 \times 10^{-5} \times F_{20} \times (\text{area of flare}/10^{17}\ cm^2)$. In thick target, the differential electrons spectrum index is just $\gamma + 1$.

Table 3 gives, for both D_3 and the 10830Å line, the total line center optical depth of the flare, the value of the source function, S, at unit optical depth, in units of I_{DC}, and Q, the total line emission radiated outwards in ergs $cm^{-2}\text{-}s^{-1}$. Also listed are the temperature and density of the atmosphere at $\tau_{D_3} = 1$ (hydrogen is nearly totally ionized, $N_H = N_e$). For the $F_{20} = 1 \times 10^8$ flare, Q_{D_3} is scattered photospheric radiation; in the more energetic flares, the chromosphere radiates more energy back toward the photosphere ($\approx Q$) than it absorbs.

4.3.1. Flare Energy

For comparison with the observed line center D_3 intensity of 0.45 I_{DC} (Section 2.7), the value of the source function at $\tau = 1$ may be used, as the gradient of S is small, especially in the less energetic flares. It is seen that an energy flux of $F_{20} \simeq 3 \times 10^8$, or $F_{rad} \approx 3 \times 10^9$ ergs $cm^{-2}\text{-}s^{-1}$ is needed for agreement. Integrated over the flare kernel area ($\approx 10^{17}\ cm^2$) and duration (≈ 140 s), a total flare energy of $\approx 4 \times 10^{28}$ ergs is obtained. Heating of the

halo would make some additional, but not larger, contribution (Zirin and Tanaka, 1973). We thus estimate that the flares of November 15, 1974 had a total energy of 1-200 times that of a macrospicule.

Moore and Datlowe (1975), from analysis of soft X-ray and optical observations of the thermal phase of flares, give a scaling law for the total flare energy; $E_F \approx 10^{30}$ ergs x area in solar square degrees. An energy of $\approx 9 \times 10^{28}$ ergs is predicted for the November 15 kernel. Again, the validity of this law in this particular case is unknown. The available soft X-ray data, from the SMS-1 satellite, had a detection threshold of 3×10^{-3} ergs cm^{-2}-s^{-1} in the 1-8Å channel (Solar-Geophysical Data, 1975). Assuming the emitting volume at 10^7 K to be a 5" cube, emission at this intensity requires a thermal energy content of $\approx 5 \times 10^{28}$ ergs. The cooling time of such a volume is only $\approx$ 40 s (due to conduction), thus the energy content would have to be replaced 2 to 6 times during the whole sequence of events. This implies that only flares with total energies larger than either estimate (from modeling, or the Moore and Datlowe formula) of the November 15 energy were detectable in soft X-rays.

4.3.2 D_3 Emission

The total (upward) D_3 emission from the kernel is predicted to be $\approx 2 \times 10^{23}$ ergs-s^{-1}, but the linewidth in the

models is only 0.2Å rather than the 0.4Å we have adopted, because only thermal velocities were used in computing the line broadening. The observed value (Section 2.7.2) was $\approx 1 \times 10^{24}$ ergs-s^{-1}. The total D_3 emission over the flare lifetime, $\simeq 1.4 \times 10^{26}$ ergs, is of order 0.5% of the flare energy.

4.3.3 Other Properties

Both the electron heating time and the radiative cooling time (due mostly to hydrogen) of the D_3 emitting layer in the models are less than 10 seconds, confirming the ability of the thick target process to reproduce the rapid time evolution of the flares. The models also indicate that the appearance of the flares in emission was indeed an artifact of their nearness to the limb. If located at disk center, they would have appeared strongly in absorption, having substantial optical depth and $S < I_{DC}$. As stated in Section 2.5, no such rapid D_3 absorption events have been observed outside active regions.

It is of interest to compare, for example, the $F_{20} = 10^9$ thick target model to the $T = 2 \times 10^4$ "supermacrospicule" ("sms") model, as the temperature and electron density predicted for the D_3 region is the same in both. The "sms" D_3 layer is layer is $\approx$ 2000 km thick, while in the thick target, only $\approx$ 200 km; the "sms" should thus have a much larger D_3

optical depth (τ_{D_3} = 1 in ≈ 200 km). Now, the thick target layer already has S ≈ I_{DC} with $\tau \approx 1$. The larger optical depth of the "sms" would further the buildup of the radiation field, raising S even higher. A more accurate "sms" model at this temperature would thus have a reduced electron density or alternatively, have a "filling factor", that is, the "sms" would be composed of a group of dense substructures in a less dense matrix.

4.3.4 Vertical Structure

The thick target flare models clearly have severe limitations; in particular, the D_3 emitting region is a thin (≈ 200 km), low-lying (≈ 1400 km), plane-parallel layer, since the density structure of the models is determined by the preflare hydrostatic equilibrium. This conflicts with the observed flare thickness. Some of the observed thickness must be due to the heating of material previously elevated above its hydrostatic level; for example, ejected in spicules or arches.

An estimate can be made of the vertical extent such structures might contribute to an otherwise planar flare, by determining what part of them is radiatively stable against an electron flux of $F_{20} = 3 \times 10^8$ ergs cm^{-2}-s^{-1}, injected down the structure axis. Using Beckers' (1972) density model for spicules, the lowest 3 - 4 Mm are found to be stable. Beckers' model applies to objects 10 Mm in length,

which is common for horizontal fibrils or arches (which appear to form a family with spicules; Marsh, 1976), but is very rare for vertical spicules, whose average height is 5Mm. If a new model is adopted, using Beckers' densities at 1/2 his altitudes, only the lowest 500 km are radiatively stable against electron injection. It appears that the flare heating of fine structures elevated prior to the flare, could provide about 1 - 3 Mm of vertical "fuzz", partially explaining the observed flare thickness. (Note that this resembles a "supermacrospicule" composed of substructures).

4.3.5 Other Problems

Another problem of the thick target models is that, being static, they cannot explain the dynamic vertical features seen during several of the flares. Such objects are most likely produced by the disruption of the atmospheric density structure. Electron heating can cause thermal evaporation and/or shock compression of the chromosphere, and if the chromosphere were disturbed down to the level of D_3 emission, material ejection might become apparent. Timing is also a problem, as a vertical feature was seen after just 10 s in one case (event 2), but only after more than 50 s in another (event 4).

A third problem is the apparent constancy of the peak flare brightness. It would suggest that the electron flux was similarly constant (since $S \propto F_{20}$ at these flare

energies), for which there is no apparent reason. If the vertical features did represent the disruption of the D_3 layer, the reduced flare brightness at those times might be understood; however, the atmosphere would then have to reconstitute itself in less than 10 seconds (between events 5 and 6).

The thick target models have both strengths and weaknesses in trying to explain the flares of November 15, 1974. It probably should not be expected that any single, simple mechanism could explain all the details of such events. We note, however, that Canfield and Brown (private communication), by comparison of more detailed models with optical data of a flare, were able to predict within an order of magnitude, the hard X-ray flux (thus, electron energy input) actually observed for that same event.

5. DISCUSSION

The November 15, 1974 events apparently are the largest flares observed in the polar caps, latitude $\geq$ 60°. The relation of these events to other forms of solar activity depends upon the type of magnetic region in which they occurred, since very different predictions for the rate, solar cycle phase, and latitude of similar events can be made. We consider three possibilities.

5.1 Sunspot Region

Sunspot regions are those active regions which at some time produce spots. Regions with high latitudes are rare; between 1877 and 1956, only 23 regions were reported above 40°, or about 3 per sunspot cycle (compared with 4000 normal regions per cycle), and occurred 1.2 $\pm$ 1.2 years after sunspot minimum (Maunder, 1917; Hoge, 1943; Dodson, 1953, Waldmeier, 1957). The only spots in the polar caps were found by Maunder (1917), who reported four regions visible simultaneously between 63 and 72° south. (We cannot detect any of these regions on the Mt. Wilson daily continuum and K-line photographs).

No spots were seen in the flaring region, but spots (generally pores) in small regions appear and disappear quickly, and could have decayed before or grown after the short observing period. The flares occurred 1.4 years before sunspot minimum, nearly 1/4 of a cycle earlier than expected for a high latitude region. Given the infrequency of high latitude regions, polar flares would be very rare, perhaps once per century, and future events should be concentrated at low latitudes during spot maximum. We consider it highly improbable that the flaring region was a sunspot region, because of its high latitude and solar cycle phase.

5.2 Ephemeral Regions

Ephemeral regions are magnetic eruptions that never

produce spots, and are generally small and shortlived. They increase and decrease in numbers in phase with the spot cycle, but are 1000 times more numerous, and have a broader latitude distribution (Martin and Harvey, 1976; Glackin, 1973). Near spot minimum, the surface density of ephemeral regions is uniform from pole to equator (Harvey et al., 1975; Martin and Harvey, 1976). Macrospicules, the usual ephemeral region activity, show no variation in numbers at the poles through the cycle (Mosher, private communication).

The flares had a total energy of order $10^{28.6}$ ergs, which, by analogy with spot region flares, should be $< 10\%$ of the total magnetic energy of the region (Tanaka and Nakagawa, 1973; Tanaka, 1977). A typical ephemeral region, with 1 day lifetime, 10^{20} Mx total flux, and 10 Mm size, has (using the method of Wellck and Nakagawa, 1973) a total magnetic energy of $E_M \approx (4\pi)^{-1} \times (\text{unipolar flux})^2 \times (\text{unipolar area})^{-1/2} \approx 10^{28.7}$ ergs. Longer-lived ephemeral regions have larger fluxes, but, again by analogy with spot regions, flares should be more common in a region formed of multiple small dipoles, rather than a single large dipole. Martin and Harvey (1976) show examples of adjacent, small ephemeral regions. The rate of adjacent pairs of the larger regions can be calculated, given their size (10 Mm), lifetime (1 day) and surface density in late 1974 ($300\ (A_\odot - \text{day})^{-1}$). Assuming each region is randomly located on the surface, there

are $\approx 2\ (A_\odot - \text{day})^{-1}$ ephemeral region pairs, of which only some fraction should generate flares. This compares with the upper limit for polar flares of $3\ (A_\odot - \text{day})^{-1}$.

Complex magnetic structures can also be produced by ephemeral regions interacting with polar faculae, the unipolar magnetic areas which mark the dipole field of the sun. The numbers of polar faculae vary out of phase with the spot cycle, being largest at spot minimum (Sheeley, 1976), and the faculae form a distinct polar cap, being more numerous about 60° latitude than between 30 and 60° (Mosher, 1976). The Mt. Wilson daily photographs in 1975 and 1976 show the surface density of faculae increased in the ratio 1:4:7, ±25%, for latitudes 30-60°, 60-75°, and 75-90°, respectively. (Our average number of polar faculae in August 1975 agrees with Sheeley's). This is one fact which helps explain why the first observed event should be found so near the pole.

As with spot regions, ephemeral regions are numerous at low latitudes at spot maximum, and future events should be concentrated there. We believe that the flaring region was most probably a complex ephemeral region, because the broad latitude distribution of ephemeral regions makes the polar location more understandable.

5.3 Something Else

It may be that the polar location of the flare region was a necessary condition, and future observations would

show a distinct concentration at the poles. A new kind of solar active region would then be involved, with an unknown relation to the spot cycle. Given a single event, we cannot infer the existence of such structures; however, future observations should not avoid the poles just because low latitude events seem more probable.

6. SUMMARY

1) Flares with He I D_3 in emission on the disk have been observed in the polar region. The D_3 intensity shows 100% modulation in 10 s. D_3 optical depth is > 1. Total energy emitted in D_3 is $\approx 10^{26}$ ergs.

2) All these properties are much different from those of normal polar activity, macrospicules. The flare intensity is too large to be produced by radiative mechanisms, which operate in macrospicules. The existence of collisional excitation implies a flare energy much larger than that of a macrospicule.

3) Morphologic properties suggest that thick target electron bombardment was a plausible energy source (for the chromosphere). Calculation of the D_3 emission from thick target model flares, when compared with the observed line intensity, implies a total flare energy of order $10^{28.6}$ ergs.

4) The most probable site for the flares was a complex magnetic ephemeral region. Larger than average size

and/or eruption near pre-existing fields (perhaps another ephemeral region) appears necessary.

ACKNOWLEDGEMENTS

We thank Harold Zirin for helpful suggestions and Richard Canfield and Ronald Moore for useful discussions. We thank Robert Howard for the use of the Mt. Wilson data, and the observers of Big Bear Solar Observatory, Gene Longbrake, Jack Klemroth, and Peter Kupferman, for obtaining the data.

This work was supported by NASA under grant NGR 05 002 034 and NSF under grant ATM76-21132.

APPENDIX: Calculation of the Helium Emission

A.1 Method

The thick target models (LaBonte, 1978b) give the hydrogen and electron number densities and temperature as functions of height in a one-dimensional atmosphere. For this study, the populations of He I, II, III, and several terms within the He I atom, as well as the radiation fields of several He I lines were determined, given the models' structure. A helium to hydrogen number ratio of 0.1 was used. The contribution of helium ionization to the electron density was ignored. The electron velocity distribution was a Maxwellian at the model temperature. Collisional coefficients are taken from Benson and Kulander (1972), recombination coefficients from Burgess and Seaton (1960) and radiative parameters from Wiese et al. (1966).

Five bound terms are included in the model He I atom; 1S and 2P in the singlet spin system, and 2S, 2P, 3D in the triplet spin system. He II and III ground levels are also used. The D_3 (3^3D to 2^3P) and 10830Å (2^3P to 2^3S) lines are of principal interest; the 584Å (2^1P to 1^1S) line is also considered for information on the resonance lines and the excited singlet terms. Both the He I 504Å and He II 228Å Lyman continua are assumed in radiative detailed balance; this approximation works well for hydrogen (Pottasch and Thomas, 1959) and should work even better for helium, where

the larger ionization potentials further reduce the collisional coupling. All other continua are optically thin, with photoionization rates fixed by the photospheric radiation field.

Each line is computed using the two-level approximation, with only processes in the line determining the radiation field and relative populations of the upper and lower terms. Initial guesses for the number densities are used to calculate the rates; once the lines are solved, new absolute values of the densities are determined from the relative values through the solution of the ionization equilibrium. Iteration, solving alternately for the radiation and the populations, continues until convergence to a consistent solution.

The He II to He I and triplet to singlet population ratios are determined using a three level scheme, singlets, triplets, and continuum. The rates from each spin system are totals based on the previously calculated relative populations of the terms within the spin system. Once the total population of a spin system is found, it is apportioned according to the relative populations of the terms. This treatment is consistent with the two-level approximation used for the lines.

The He III to He II ratio is set by the balance of collisional ionization from the ground state and radiative

recombination to excited states. Collisional recombination is negligible, and radiative recombination to the ground state is ignored, given the assumption of detailed balance; recombination to excited states is effective, however, since the rate to the ground state through the Lyman lines (due to photon escape and absorption by He I), even considering the optical depth, is larger than the ionization rates from the excited states. The triplet lines are emitted in a region where the He II to He I ratio is $\approx$ 1, with errors in the He III to He II ratio not strongly affecting the results.

For the calculation of the radiation fields, an adaption of the probabilistic method (Athay, 1972) is used. In a one-dimensional atmosphere, for radiative transitions which scatter noncoherently, the mean intensity J is

$$J(N_m) - J(N) = \frac{1}{2} \; e^{u(N)} \int_N^{N_m} [P_c \; J] \; e^{-u(S)} dS, \qquad (A1)$$

with

$$u(S) = 1/2 \int_0^S (P_e + P_d) \; (1 + x^2) \; dW \quad . \qquad (A2)$$

The radiation anisotropy $x = 2H/J$, H the net flux. P_c, P_d, P_e are the probabilities per photon scattering that a photon is newly created, destroyed, or escapes from the atmosphere, respectively. The depth variable N is the mean number of scatterings for escape, just equal to P_e^{-1}.

For a Doppler broadened line,

$$P_e(\tau) = 1/2 \left[1 + 2\tau[\pi \ln(\tau + 1)]^{1/2}\right]^{-1} , \qquad (A3)$$

(Avrett and Hummer, 1965), with τ the line center optical depth to the surface. In the two-level approximation, with no overlapping continuum,

$$P_d = \frac{\varepsilon}{1 + \varepsilon} \qquad (A4)$$

with $\varepsilon = C_{UL}/A_{UL}$, the ratio of collisional to radiative deexcitation rates.

The term $[P_c\ J]$ in Equation A1 is the rate of photon creations. The contribution from collisional excitation is

$$[P_c\ J]_c = P_d\ B , \qquad (A5)$$

B the Planck function (Athay, 1972). For the triplet lines, the photospheric radiation also contributes,

$$[P_c\ J]_p = P_e(T)\ J_p , \qquad (A6)$$

J_p the photospheric mean intensity, and T the optical depth to the photosphere.

The boundary condition on the integral of Equation A1 is found from the differential form of that equation. At the point in the atmosphere which has the largest value of N, namely N_m, dJ/dN should be zero, and

$$J(N_m) = \frac{[P_c\ J]}{(P_c + P_d)\ (1 + x^2)} \qquad (A7)$$

In a semi-infinite atmosphere, x would also be zero at this point. For a thin chromosphere, $N = (P_e(\tau) + P_e(T))^{-1}$, since escape at either boundary is effective.

The probabilities are determined from the various number densities. The mean intensity is computed, then the line source function in the two-level approximation,

$$S = \frac{J + \varepsilon B}{1 + \varepsilon} \quad , \tag{A8}$$

and finally, the relative populations of the upper and lower terms, n_U/n_L, from

$$\frac{n_u}{n_L} = \frac{g_u}{g_L} \left[\frac{2\ h\nu^3}{c^2} \frac{1}{S} + 1 \right]^{-1} \tag{A9}$$

g_U, g_L the statistical weights, h Planck's constant, c the speed of light, ν the line frequency.

Once the iteration procedure has converged, giving a consistent set of densities and radiation fields, the total energy emitted in the line is just

$$Q = \int_o^\infty h\nu\ n_U\ A_{UL}\ P_e\ (\tau) \quad dh \quad . \tag{A10}$$

The line profile could also be computed,

$$I = \int_o^\infty S\ \phi_\nu\ e^{-\tau(\nu)}\ d_\tau \quad , \tag{A11}$$

ϕ_ν the emission profile, but as S for the triplet lines varies little in the models which best fit the November 15 flares, we use I(line center) $\simeq$ S. This approximation is

further strengthened by the foreshortening near the limb, which makes the line-of-sight optical depth larger than the vertical depth given in Table 3.

A.2 Consistency

The calculation assumes that equilibrium is reached within the timescale of the flares, $\approx$ 10 s, which requires all rates in the helium system be $\gtrsim (10\ s)^{-1}$ in the layer emitting D_3. This condition is satisfied by the models with $F_{20} \gtrsim 10^9$, but is violated by the $F_{20} = 10^8$ model, in the rates connecting the He I singlets with He II. At the particular energy that we have ascribed to the flares, the violations are factors of order 2. This failing may be one of the lesser problems in judging the applicability of the models.

The two-level approximation used assumes that the rates connecting the terms of a given line, in the line, are much larger than the rates through other levels; the continuum, or terms in either spin system, including those left out of the model atom. The term most affected by such interlocking is 3^3D. The net loss rate from 3^3D to 2^3S via 3^3P is the most important, and is $\simeq$ 25% of the D_3 A value. The total loss rates to all other levels is less than this amount. The use of this approximation, and the structure of the model atom appear valid to the accuracy of the calculation.

Only collisions with thermal electrons were included.

Zirin (1977) has suggested that direct excitation from the ground state by collisions with the nonthermal beam electrons is important to the hydrogen emission in thick target flares. This mechanism does not work for the He I triplet lines. The transition from the ground state to the triplet system is spin-forbidden, and it can only proceed as an exchange reaction, whose cross-section falls very rapidly with increasing incident electron energy (Morrison and Budge, 1967; Van Raan et al., 1974). For example, the cross-section to 3^3D at 20 keV is $< 10^{-8}\ \pi a_o^2 \approx 10^{-24}\ cm^2$; in the $F_{20} = 10^9$ flare, with a $\geq$ 20 keV electron flux of $3 \times 10^{16}\ cm^{-2}s^{-1}$, the excitation rate is $\approx 3 \times 10^{-8}\ s^{-1}$, compared with the thermal rate of $\approx 3 \times 10^{-4}\ s^{-1}$ from the ground state, and $\approx 5 \times 10^5\ s^{-1}$ from 2^3P. An additional effect, the breakdown of LS-coupling in high excited terms (Van Den Eynde and Weibes, 1972), which contributes to laboratory measurements of the cross-sections being anomolously large, is not important. The rate (Lin and Fowler, 1961) for transitions from singlets to triplets by this mechanism ($\approx 500\ s^{-1}$ at a He I density of $10^{12}\ cm^{-3}$) is small compared to the radiative and thermal collisional rates ($\approx 5 \times 10^4\ s^{-1}$ through the continuum in the $F_{20} = 10^9$ model) in the hot, ionized, illuminated flare chromosphere. Note that direct excitation of the singlet terms is permitted, the cross-sections are larger, and it may be that at some times and

places, direct excitation does affect the singlet line intensities in flares.

A.3 Results

Those properties of the calculations which directly apply to the study of the November 15, 1974 flares have already been discussed. There are additional results which are of interest to the general problem of helium emission from flares.

Flares with $F_{20} \lesssim 10^8$ have no true emission in the triplet lines, but simply scatter photospheric radiation. At higher energy densities, the chromosphere emits more than it absorbs, and the triplet lines contribute to cooling the flare.

In the models with $F_{20} \gtrsim 10^9$, the total energy emitted by He I is dominated by the triplet lines. Energy loss in the 584Å line is $\approx$ 5% of the loss in 10830 and D_3. The cause of this behavior is as follows; each collisional excitation to 2^1P produces one 20 eV photon. A collisional excitation to 2^3P (of which there are three times as many) cannot radiatively decay to the ground state, but returns only through slower collisional processes. While the electron resides in the triplets, it experiences repeated collisional excitations and radiative decays in the 1 and 2 eV lines, which are well coupled to the 2 eV thermal electrons. The total emission in the triplet lines turns out

to exceed the 584 flux.

In the same models, the total energy emitted by He I is $\approx$ 10% of that emitted by hydrogen. The 10830 line also happens to be $\approx$ 10% of Hα. Given the differences in the atomic systems and that the emissions come from different parts of the atmosphere, there is no simple reason why these relations hold.

REFERENCES

Athay, R.G.: 1972, Ap. J., 176, 659.

Avrett, E.H. and Hummer, D.G.: 1965, M.N.R.A.S., 130, 295.

Baum, P.J. and Bratenahl, A.: 1976, Solar Phys., 47, 331.

Beckers, J.M.: 1972, Ann. Rev. Astr. Ap., 10, 73.

Benson, R.S. and Kulander, J.L.: 1972, Solar Phys., 27, 471.

Bessey, R.J. and Kuperus, M.: 1970, Solar Phys., 12, 216.

Bohlin, J.D., Vogel, S.M., Purcell, J.D., Sheeley, N.R., Tousey, R., and Van Hoosier, M.E.: 1975, Ap. J., 197, L133.

Brown, J.C.: 1973, Solar Phys., 31, 143.

Brown, J.C.: 1974, Solar Phys., 36, 371.

Burgess, A. and Seaton, J.J.: 1960, M.N.R.A.S., 121, 471.

Canfield, R.C.: 1969, Ap. J., 157, 425.

Canfield, R.C.: 1971, Astr. and Ap., 10, 64.

Canfield, R.C.: 1974, Solar Phys., 34, 339.

Colgate, S.A., Audouze, J. and Fowler, W.A.: 1977, Ap. J., 213, 849.

Cox, D.P., and Tucker, W.H.: 1969, Ap. J., 157, 1157.

Dodson, H.W.: 1953, P.A.S.P., 65, 256.

Glackin, D.L.: 1973, P.A.S.P., 85, 241.

Godoli, G. and Mazzucconi, F.: 1967, Ap. J., 147, 1131.

Golub, L., Krieger, A.S., Silk, J.K., Timothy, A.F. and Vaiana, G.S.: 1974, Ap. J., 189, L93.

Harvey, K.L., Harvey, J.W., and Martin, S.F.: 1975, Solar Phys., 40, 87.

Hoge, E.R.: 1943, P.A.S.P., 55, 182.

Hudson, H.: 1972, Solar Phys., 24, 414.

Jefferies, J.T., Smith, E.v.P. and Smith, H.J.: 1959, Ap. J., 129, 146.

Kane, S.R.: 1974, in G. Newkirk (ed.), I.A.U. Symp. 57, 105.

Krat, V.A. and Sobolev, V.M.: 1960, Izv. Astron. Obs. Pulkovo, 21, 2.

Kvicala, J., Hrebik, F., Olmr, J., Svestka, Z. and Krivsky, L.: 1961, Bull. Astron, Inst. Czech., 12, 47.

LaBonte, B.J.: 1977, Solar Phys., 53, 369.

LaBonte, B.J.: 1978a, Big Bear Solar Obs. preprint 0171.

LaBonte, B.J.: 1978b, Big Bear Solar Obs. preprint 0173.

Labs, D. and Neckel, H.: 1968 Z. Ap., 69, 1.

Lin, C.C. and Fowler, R.G.: 1961, Ann. Phys., 15, 461.

Lin, R.P. and Hudson, H.S.: 1976, Solar Phys., 50, 153.

Marsh, K.A.: 1976, Solar Phys., 50, 37.

Martin, S.F. and Harvey, K.L.: 1976, A.F. Geophys. Lab Final Report, AFGL-TR-76-0255.

Maunder, Mrs. W.: 1917, M.N.R.A.S., 77, 621.

Michard, R.: 1959, Ann. d'Ap., 22, 887.

Moore, R.L. and Datlowe, D.W.: 1975, Solar Phys., 43, 189.

Moore, R.L., Tang, F., Golub. L. and Bohlin, J.D.: 1977, Big Bear Solar Obs. preprint 0162.

Morrison, D.J.T. and Budge, M.R.H.: 1967, Proc. Phys. Soc. London, 91, 565.

Mosher, J.: 1976, Ph.D. thesis, Calif. Inst. of Tech.

Nakagawa, Y., Wu, S.T. and Han, S.M.: 1973, Solar Phys., 30, 111.

Pierce, A.K. and Waddell, J.H.: 1961, Mem. R.A.S., 68, 69.

Pope, T. and Schoolman, S.: 1975, Solar Phys., 42, 471.

Pottasch, S.R. and Thomas, R.N.: 1959, Ap. J., 130, 941.

Ramsey, H.E. and Martin, S.F.: 1974, Lockheed Final Report, LMSC/D401258.

Ramsey, H.E. and Martin, S.F. and Harvey, K.L.: 1975, Lockheed Final Report, AFCRL-TR-75-0355.

Ramsey, H.E. and Mosher, J.: 1976, preprint.

Sheeley, N.R.: 1976, J.G.R., 81, 3462.

Shmeleva, O.P. and Syrovatskii, S.I.: 1973, Solar Phys., 33, 341.

Smith, E.v.P.: 1963, Ap. J., 137, 580.

Solar-Geophysical Data, 366 (Supl.), p13, Feb. 1975, U.S. Dept. of Comm. (Boulder, Col., USA 90302).

Steshenko, N.V. and Khokhlova, V.L.: 1960, Izv. Kryms. Astrofiz. Obs., 23, 322.

Svestka, Z., Kopecky, M. and Blaha, M.: 1962, Bull. Asstron. Inst. Czech, 13, 37.

Tanaka, K.: 1977, Big Bear Solar Obs. preprint 0168.

Tanaka, K. and Nakagawa, Y.: 1973, Solar Phys., 33, 187.

Van Den Eynde, R.K. and Wiebes, G.: 1972, Physica, 59, 401.

Van Raan, A.F.J., Moll, P.G. and Van Eck, J.: 1974, J.Phys. B, 7, 950.

Waldmeier, M.: 1957, Z. Ap., 43, 29.

Wellck, R.E., and Nakagawa, Y.: 1973, NCAR Technical Note NCAR-TN/STR-87.

Wiese, W.L., Smith, M.W. and Glennon, B.M.: 1966, Atomic Transition Probabilities, Vol. 1, (Wash. D.C., U.S. Dept. of Commerce).

Withbroe, G.L., Jaffe, D.T., Foukal, P.V., Huber, M.C.E., Noyes, R.W., Reeves, E.M., Schmahl, E.J., Timothy, J.G. and Vernazza, J.E.: 1976, Ap. J., 203, 528.

Zirin, H.: 1975, Ap. J., 199, L63.

Zirin, H.: 1977, Big Bear Solar Obs. preprint 0165.

Zirin, H. and Tanaka, K.: 1973, Solar Phys., 32, 173.

Table 1

NOVEMBER 15, 1974 D_3 FLARE HISTORY

Event Number	Time (UT)	Duration (seconds)	Vertical Extent Above Limb (arc seconds)
1	2050:38 only	< 20	-
2	2110:27 only	< 20	4.5
3	2119:16 to 2119:26	10 to 30	4.5
4	2124:46 to 2125:36	50 to 70	8.0
5	2126:06 to 2126:26	20 to 40	4.0
6	2126:46 only	< 20	-
	Total:	80 to 200	

Table 2

11/15/74 FLARE

"SUPERMACROSPICULE" MODEL

Temperature $T(^\circ K)$	1_{+4}	1.5_{+4}	2_{+4}	4_{+4}	6_{+4}
D3 collisional excitation coefficient $C_{ex}(cm^3\ s^{-1})$	1.5_{-8}	4.2_{-8}	7.1_{-8}	1.7_{-7}	2.5_{-7}
Electron density $N_e^c(cm^{-3})$	1_{+13}	5_{+12}	3_{+12}	1_{+12}	8_{+11}
Energy content $N_e^c V (R_H + 3kT)$ (ergs)	7_{+27}	3_{+27}	2_{+27}	8_{+26}	7_{+26}
Recombination time $(N_e^c \alpha_H)^{-1}$ (s)	0.2	0.5	0.9	2.0	3.0
Radiative cooling time $(R_H+3kT)/P\ N_e^c$ (s)	0.9	0.2	0.1	0.2	0.2

$1_{+10} \equiv 1 \times 10^{10}$.

Radiative cooling coefficient P from Cox and Tucker (1969).

Table 3

HELIUM TRIPLET EMISSION FROM THICK TARGET FLARE MODELS

Electron energy flux ($ergs\text{-}cm^{-2}\text{-}s^{-1}$)				
F_{20}	1_{+8}	1_{+9}	1_{+10}	1_{+11}
R_{rad}	1.2_{+9}	4.1_{+9}	1.9_{+10}	5.5_{+10}
D_3 line				
τ	.16	.99	4.7	14.
$S/I_{DC}(\tau=1)$	.28*	.68*	2.6	6.7
Q ($ergs\text{-}cm^{-2}\text{-}s^{-1}$)	6.4_{+5}	5.2_{+6}	2.8_{+7}	9.3_{+7}
10830 Å line				
τ	.86	2.4	7.0	18.
S	.89	2.3	4.8	6.8
Q	3.5	1.1_{+7}	2.3_{+7}	3.3_{+7}
Atmosphere at $\tau_{D_3}=1$				
Altitude (km)	1500*	1350*	1230	1150
Temperature (K)	2.0_{+4}*	1.9_{+4}*	1.9_{+4}	2.2_{+4}
Electron density (cm^{-3})	1.3_{+12}*	2.9_{+12}*	6.2_{+12}	9.9_{+12}

Optical depths (τ) and total line emissions (Q) are integrals vertically through the chromosphere.

Values marked * apply to the middle of the D_3 layer, since $\tau_D < 1$.

FIGURE CAPTIONS

Figure 1

Polar flares with D_3 emission, November 15, 1974. Times are given in UT. The flare site is at 79° south latitude. Frame at 2124 shows the region in the absence of activity. Six separate events are represented. The D_3 activity appears as a knot of emission inside the limb, with a vertical feature extending above the limb at four of the times shown. Frames at 2110, 2125:36 and 2126:16 are printed twice, to show detail on the disk and above the limb.

Figure 2

(a) Intensity profiles of D_3 emission knots, measured along a solar radius. Intensity scale is in units of I_{DC}, the specific intensity of the continuum at disk center. The limb is located at D=0. The three flare profiles are for times illustrated in Figure 1. Simultaneous profiles of nearby quiet areas are included for comparison.

(b) Contrast profiles of the same knots, measured parallel to the limb. The flares have a kernel of 5" diameter and a halo of 20" diameter. These tangential profiles are more nearly constant at different times than the radial profiles.

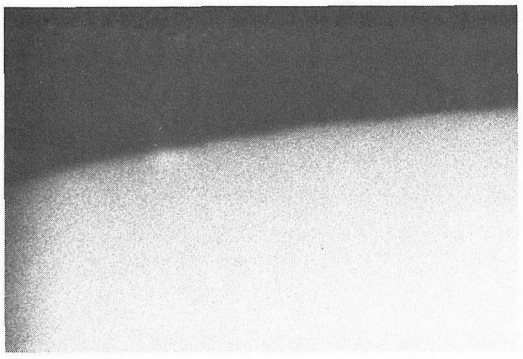

20 50:38

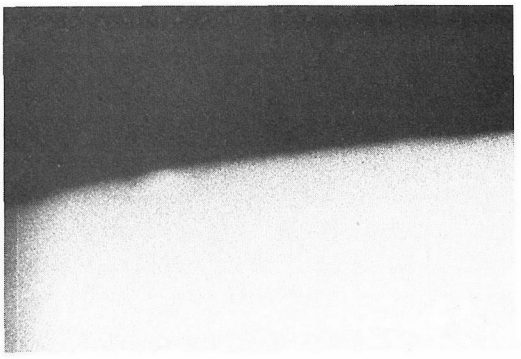

21 25:16

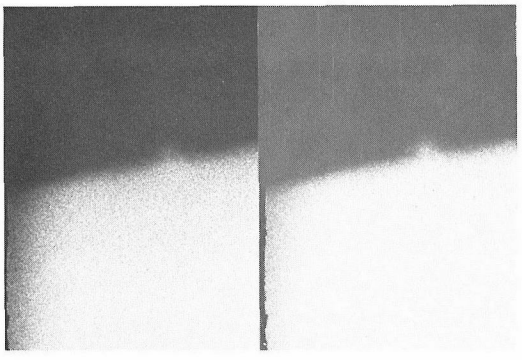

21 10:27

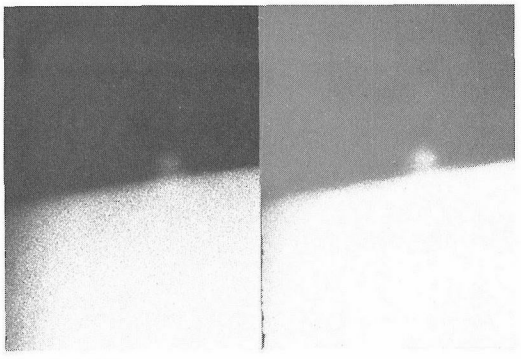

21 25:36

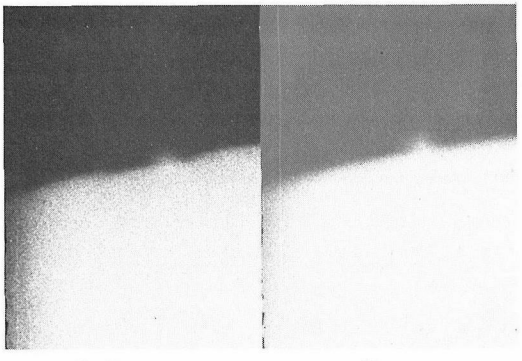

21 19:16 :26

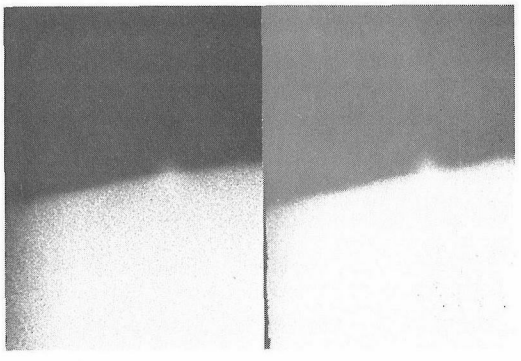

21 26:16

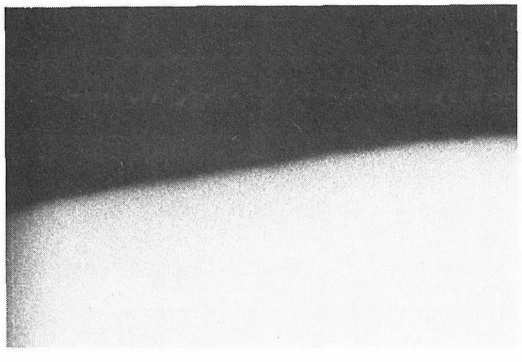

21 24:10

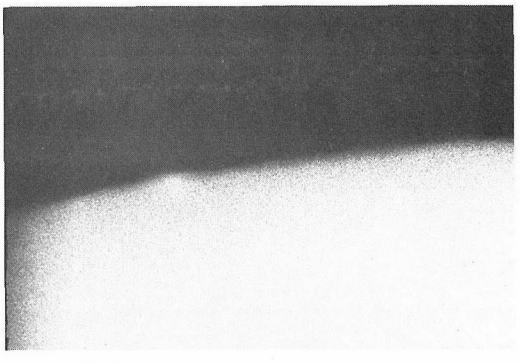

21 26:46

20″

Figure 1

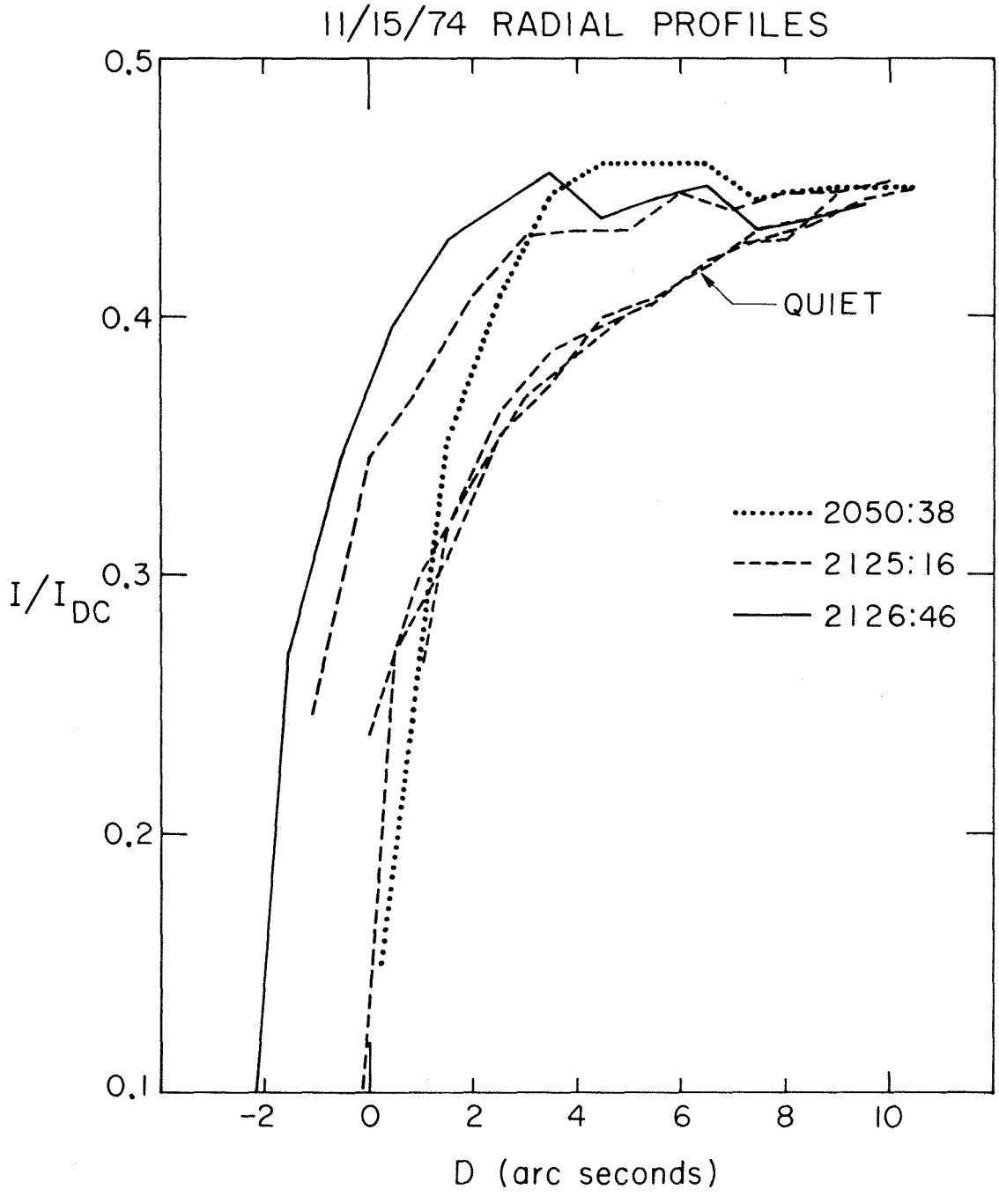
11/15/74 RADIAL PROFILES
0.5
0.4
0.3
0.2
0.1
I/I DC
QUIET
2050:38
2125:16
2126:46
-2
0
2
4
6
8
10
D (arc seconds)

Figure 2a

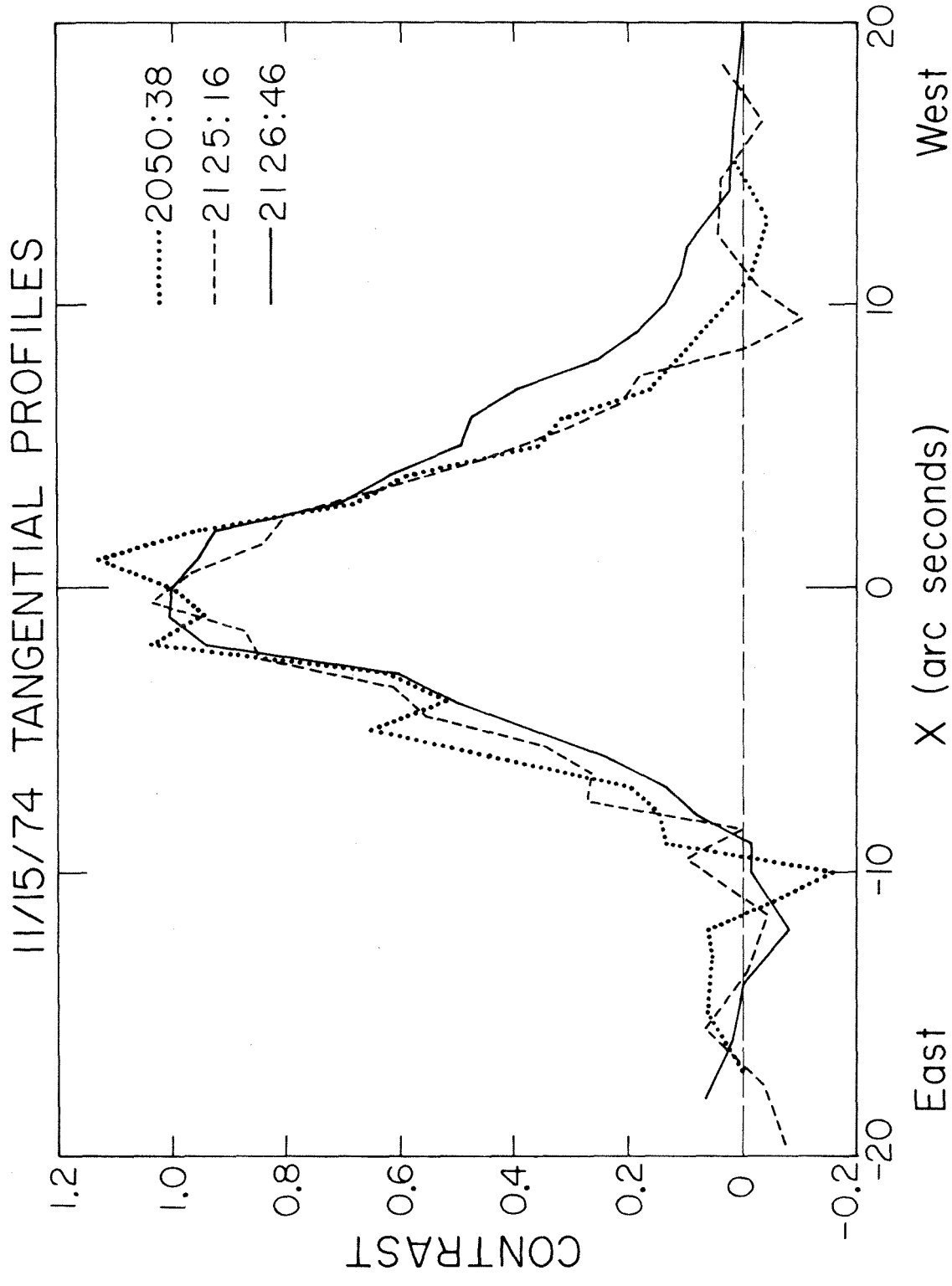
11/15/74 TANGENTIAL PROFILES
2050:38
2125:16
2126:46
CONTRAST
1.2
1.0
0.8
0.6
0.4
0.2
0
-0.2
-20
-10
0
10
20
East
X (arc seconds)
West

Figure 2b

CHAPTER 5

THICK TARGET MODELS OF IMPULSIVE CHROMOSPHERIC FLARES

Appears as BBSO Preprint No. 0173

ABSTRACT

The most impulsive flares show large amplitude intensity variations in times of order 10 s. An attempt is made to reproduce the properties of these events with a model in which the heating of a static chromosphere by a nonthermal electron beam is balanced by thermal radiation cooling. The computed results suggest that the assumed static equilibrium may be achieved in some parts of the flares, and indicate improvements necessary for more accurate models of this type of flare.

1. INTRODUCTION

Risetimes of solar flares vary from seconds (Zirin, 1977) to hours (Sheeley et al., 1975; Kahler, 1977). The intensities of the chromospheric flare phenomena appear to be inverse to the risetime. Flares with the most rapid evolution, those with prominent chromospheric impulsive phases, are of particular interest.

Observationally, impulsive flares produce the largest optical emission intensities and linewidths (Zirin and Tanaka, 1973). These reflect high electron densities, and the alteration of the chromosphere at great depths. Microwave, meterwave, and hard X-ray emissions indicate the presence of energetic nonthermal electron beams, and important nonequilibrium processes. In some flares, this nonthermal process may release an energy comparable to the total flare energy (Lin and Hudson, 1976).

In many models of flare plasma mechanisms, the impulsive phase occurs just as the flare is "triggered", the moment at which the quiescent plasma processes fail to relax the increasing stresses (Sturrock, 1968; Heyvaerts et al., 1977). The onset of plasma instabilities allows the dissipation of the stored energy in the flare. Study of the impulsive phenomena may reveal the nature of the flare instability, since the fastest evolving phenomena have presumably been least altered by propagation effects between

the flare instability and the observer.

Finally, the extreme-ultraviolet radiation flash from the impulsive flare produces the strongest unpredictable terrestrial effect, the sudden ionospheric disturbance (Donnelly, 1971). Other flare phenomena with terrestrial impact, such as particle fluxes or shock waves, propagate slower than the velocity of light, and can be anticipated once the flare is observed optically.

We report here on an attempt to model the properties of the chromosphere in one type of impulsive flare. The prominent characteristic of these events is rapid optical emission flashing in high excitation lines. Knots 1 to 5 arcseconds in extent exhibit 100% intensity modulation on 5 to 10 second time scales. These events have been observed in high Balmer lines (Zirin and Tanaka, 1973) and He I D_3 (LaBonte, 1978). In the one case where data are available, the optical emission is simultaneous with nonthermal hard X-ray emission, which also has large amplitude intensity modulation on few second time scales (Van Beek et al., 1973).

The simultaneity of nonthermal hard X-rays with the impulsive phase of optical flares is well established in the general phase (Vorpahl, 1972; Zirin, 1973). Correlated, rapid, low amplitude intensity fluctuations in X-rays and optical continuum emission have also been observed (Rust and Hegwer, 1975). The type of event we describe thus represents

the extreme, in terms of intensity modulation on short time scales, of flares with related optical and nonthermal X-ray emission.

As with most impulsive events, these flashes are not the entirety of the optical flare, but only one phase. However, an individual flare may have several impulsive knots, which in part accounts for events with long-lived nonthermal X-ray emission. A second type of long-lived nonthermal event to which our models may also apply is the case of a steady energy flux, with variation only in the position on the chromosphere which is bombarded. A point would be heated only briefly compared with the total duration of the X-ray emission. This type of event produces a "wave" of optical emission (Zirin and Tanaka, 1973; Machado and Rust, 1974).

The interpretation we apply to these events has been suggested for the general case (Hudson, 1972; Syrovatskii and Shmeleva, 1972). A beam of nonthermal electrons, accelerated in the corona, moves downward, impacting and heating the chromosphere. X-ray emission is produced by thick target bremsstrahlung, optical emission by thermal radiation. The rapid intensity modulation of the emitted radiation is a response to variation in the electron beam flux.

The model calculations begin with a one-dimensional,

hydrostatic quiet chromosphere. It is assumed that in the flare a steady state atomic equilibrium is reached, with the electron heating in each volume balanced by thermal radiative cooling, thus determining the temperature and ionization structure. The density distribution is assumed not to relax in response to the increased temperatures in the brief duration of the flare.

Three topics are of interest. First, it must be determined whether the flare chromosphere can in fact reach a radiative equilibrium state (yet hydrodynamic effects be ignored), or if time dependent calculations are required. Second, if such an equilibrium can be achieved, it is necessary to see whether the models predict observed X-ray and optical emission intensities. Lin and Hudson (1976) and Zirin (1977) have suggested that nonthermal processes are important contributors to optical emissions. Third, the actual model results must be displayed for comparison with time dependent or nonthermal calculations. The equilibrium case may be a useful approximation, even if not strictly valid. Because the models must be calculated numerically, these points will be addressed in inverted order.

Note that Brown (1973) has computed thick target flare models; however, Lin and Hudson (1976) and Canfield (1974a) have pointed out errors in the heating and cooling equations used. In addition, Brown considered longlived flares,

allowing the density distribution to relax to the flare temperatures, a process unlikely to be important in short-lived flashes (Bessey and Kuperus, 1970).

2. MODEL PHYSICS

In this section, the physical basis of the models is described.

2.1 Preflare Atmospheric Structure

The model of Vernazza et al. (1973) is used to represent the preflare chromosphere. While the chromosphere is actually inhomogeneous at high altitude, the densities in structures such as spicules and prominences are $\lesssim 10^{11}$ cm^{-3} (Beckers, 1972; Heasley et al., 1974); to produce emission in the high excitation lines observed in the flashes requires higher densities, $\gtrsim 10^{12}$ cm^{-3} (e.g., Kulander, 1976). At the lower altitudes corresponding to the higher densities, a one dimensional, hydrostatic model may be a reasonable approximation.

Any magnetic field present is assumed to be constant with height and vertical. The electron beam is directed vertically downward, with the integral density (cm^{-2}) traversed by the beam at any height just the vertical integral of the volume density, $N(H) = \int_H^\infty n(h)dh$ Since the structure of the magnetic field is not well determined at the heights of interest, this is a useful approximation. Increasing field strength with depth (field line convergence) would concentrate and/or mirror the beam particles; nonvertical direction would increase N(H).

The quiet chromosphere's elevated temperature is maintained by some form of energy input, presumably a form of wave dissipation. We assume this heating is not increased in the flare. The nonflare heating per unit volume, G_Q, is taken to be equal to the radiative cooling calculated for the quiet atmosphere by the same methods used for the flares (Section 2.3). This nonflare term must be included in order to retrieve the quiet model temperature at depths in the flares for which electron heating is small.

Height is measured upward from the level $\tau_{5000\ \mathring{A}} = 1$ in the photosphere. The lower boundary for the flare models is 500 km, the height of the quiet temperature minimum. The top of the quiet model (the transition zone height) is 2400 km. We assume the mass above that height is zero, which is effectively true for the electron energies of interest.

2.2 Nonthermal Electron Heating

Hard X-ray (photon energies $\gtrsim$ 10 keV) flare spectra are very nearly power laws, $f(h\nu) = A(h\nu)^{-\gamma}$ photons-$(cm^2$-s-keV$)^{-1}$, with $h\nu$ the photon energy in keV. Most flares have spectral indices in the range $3 \lesssim \gamma \lesssim 5$; at Earth, peak values of f(20) range from the threshold of $\simeq 0.1$ up to $\simeq 400$, with the number of flares having $f(20) \geq f_o$ proportional to f_o^{-1} (Datlowe, 1974; Lin and Hudson, 1976).

The nonthermal spectrum is usually characterized at 20 keV as it is clearly evident at that energy. At low energies, it is covered by thermal emission from the 10^7 K (1 keV) coronal flare plasma. In a few favorable cases, the power law has been observed down to 3 to 5 keV (Kahler and Kreplin, 1971; Peterson et al., 1973). In no case has the power law been reported to flatten at an energy above the thermal emission, although it must turn over at some low energy. At high energies, $\simeq$ 100 keV, the power law is often observed to steepen, with an increase in spectral index of order 0.5 to 2 (Kane and Anderson, 1970; Frost and Dennis, 1971; Van Beek et al., 1973).

To relate the X-ray spectrum to the electron beam heating, we use the formulae of Lin and Hudson (1976). The X-ray spectrum can be inverted in the thick target case to determine the differential electron beam spectrum,

$$\frac{dn_e}{d\varepsilon} \propto \varepsilon^{-\gamma-1} \quad \text{electrons-keV}^{-1}\text{-s}^{-1},$$

ε the electron energy in keV. This in turn can be integrated to give the total energy in nonthermal electrons,

$$E_t(\varepsilon_L) = \int_{\varepsilon_L}^{\infty} \frac{dn_e}{d\varepsilon}\, \varepsilon\, d\varepsilon = 9.4 \times 10^{24}\, b(\gamma)\, A \frac{\varepsilon_L^{-\gamma+1}}{\gamma-1} \text{ ergs-s}^{-1}, \tag{1}$$

with $b(\gamma) = \gamma^2(\gamma-1)^2\, \beta(\gamma-\frac{1}{2},\frac{3}{2}) \simeq 2(\gamma-1)^2$, and β the complete beta function. The lower limit on the integration, ε_L, is

necessary to keep the total energy finite. Generally, one uses $\mathcal{E}_L = 20$ keV.

The total nonthermal energy is an integral of the nonthermal flux over the flare area,

$$E_{20} = \int_{\text{flare}} F_{20}\, da \ . \tag{2}$$

There are no spatially resolved hard X-ray observations to show the partitioning of the nonthermal flux, but distributing observed nonthermal energies over flare areas, the typical range of F_{20} is found to be $10^8 \lesssim F_{20} \lesssim 10^{11}$ ergs-cm^{-2}-s^{-1}. Our models are one dimensional and can be parameterized by the flux F_{20}. We will compute a grid of twelve models, with $F_{20} = 10^8$, 10^9, 10^{10}, 10^{11} ergs-cm^{-2}-s^{-1}, and $\gamma = 3, 4, 5$.

Energy deposition by the electron beam falls off with depth in the atmosphere. The energy gained by a volume at integral density N(cm^{-2}) is,

$$G_F(N) = 1.1 \times 10^{18}\ (\gamma-1)\ 20^{\gamma-1}\ F_{20}\ \beta\left(\frac{\gamma+1}{2}, \frac{1}{3}\right) \times$$

$$(1.1 \times 10^{-17} N)^{-\left(\frac{\gamma+1}{2}\right)}\ [X(N) + 0.55]\ n(N)\ \text{ergs-cm}^{-3}\text{-s}^{-1}, \tag{3}$$

with X the fractional ionization, n the total particle (ions plus neutrals) volume density. The quantity

$$\mathcal{E}_N = (1.1 \times 10^{-17}\ N)^{\frac{1}{2}}\ \text{keV} \tag{4}$$

is often referred to as the electron energy whose range is N.

Equation 3 does not assume a low energy cutoff in the electron spectrum. If such a cutoff exists, with $\frac{dn_e}{d\mathcal{E}} = 0$ for $\mathcal{E} < \mathcal{E}_c$, the equation remains valid for $\mathcal{E}_N > \mathcal{E}_c$, but, for $\mathcal{E}_N < \mathcal{E}_c$, the complete beta function $\beta(\frac{\gamma+1}{2}, \frac{1}{3})$ is replaced by the incomplete beta function, $\beta_z(\frac{\gamma+1}{2}, \frac{1}{3})$, $z = (\mathcal{E}_N/\mathcal{E}_c)^2$. We will use equation 3 as written. The lack of observations weighs against including an arbitrary low energy cutoff to the power law spectrum. In fact, other considerations will determine a lowest energy which contributes to the part of the flare in radiative equilibrium (Section 2.3.3). Inclusion of a high energy steepening will not turn out to be important (Section 4.1).

Instability of the electron beam is not considered; the most important problem, the need for a return current, apparently is resolved in a few seconds without major disruption of the beam (Knight and Sturrock, 1977).

2.3 Thermal Radiative Cooling

The thermal radiative cooling of a plasma has been tabulated by Cox and Tucker (1969) for the case in which the atmosphere is optically thin at all wavelengths. Unfortunately, the flare chromosphere is optically thick in many important transitions. This is obvious for

resonance transitions of abundant species (H, He, C, O, etc.) as well as subordinate lines which are deep in the quiet chromosphere (Balmer series); in dense parts of the flare, even higher ionization stages will be numerous enough to have deep lines. The computation of several transitions for each of the important species would be complex and probably not justified given the simplicity in handling other physical processes. Our solution will be to compute the hydrogen system explicitly, as it should be a major contributor to cooling, its ionization sets the electron density for the whole flare, and its emissions are observed in the optical flashes. Cooling from metals will be included by correcting the optically thin values in a way consistent with the effects of optical depth.

2.3.1 Hydrogen

Lyman α and Hα are assumed to dominate the cooling from atomic hydrogen (Canfield, 1974a) and are the only transitions included in the model. The model hydrogen atom thus has three bound levels. Since other transitions are ignored, these lines are computed in the two level approximation, with the excitation described by the source function S,

$$S = \frac{J + \epsilon B}{1 + \epsilon} , \qquad (5)$$

where J is the frequency averaged mean intensity, B the

Planck function, and $\epsilon = C_{UL}/A_{UL}$, the ratio of collisional to radiative deexcitation rates.

Line emission cools a volume by the amount

$$dQ = n_U \, A_{UL} \, h\nu \, \rho \tag{6}$$

with n_U the upper level number density, $h\nu$ the photon energy, and

$$\rho = 1 - \frac{J}{S} = \epsilon \left(\frac{B}{S} - 1\right) \tag{7}$$

is the net radiative bracket (Canfield, 1974b). In an optically thin line, no intensity is built up by scattering, and $\rho = 1$; in a deep line, $\rho << 1$ as most of the emitted photons are promptly reabsorbed and do not decrease the energy of the gas.

The ionization is set by radiative and collisional processes in the optically thin Balmer and Paschen continua, plus collisions in the Lyman continuum, which is assumed in radiative detailed balance. Bound level population ratios are set by the lines,

$$\frac{n_U}{n_L} = \frac{g_U}{g_L} \left[\frac{2h\nu^3}{c^2} \, \frac{1}{S} + 1 \right]^{-1} , \tag{8}$$

with g the statistical weight, c the speed of light. The sum of all bound and free densities equals the total hydrogen density, n_H.

The problem with an optically thick line is the

calculation of J, which depends on the emission and absorption (thus, n_U, n_L) throughout the atmosphere. We use the probabilistic method (Athay, 1972a), with many of the details from Canfield (1974a, b). [Note that there are several errors in the programs of Canfield (1974c); when corrected, the probabilistic method is more accurate than Canfield (1974b) shows.] P_c, P_d, P_e are, respectively, the probabilities per scattering that a photon is created, destroyed, or escapes from the atmosphere. The mean number of scatterings before escape is $N_s = P_e^{-1}$. From Athay,

$$P_c = P_d \, B/J \; ; \tag{9a}$$

$$P_d = \frac{\epsilon}{1 + \epsilon} \; ; \tag{9b}$$

$$P_e = \frac{1}{2 + \tau[\pi \ln(\tau + e)]^{\frac{1}{2}}} + \frac{a}{2 + \pi^{\frac{3}{4}} \, \tau^{\frac{1}{2}}} \; ; \tag{9c}$$

where τ is the line center optical depth and a the ratio of damping to Doppler linewidths. Doppler broadening by thermal and preflare turbulent velocities is included in computing the optical depth. Then,

$$J(N_s) = J(N_T) - (2N_s)^{\frac{1}{2}} \exp(t_s^2) \int_{t_s}^{t_T} P_d^{\frac{1}{2}} \, B \exp(-t_j^2) \, dt_j \tag{10}$$

with $t_k = (P_d \, N_k/2)^{\frac{1}{2}}$. For a boundary condition we use $J(N_T) = B(N_T)$, where N_T is effectively a thermalization

depth, defined by $P_d(N_T) = P_e(N_T)$. These equations assume noncoherent scattering.

The densities (which determine the probabilities) and radiation fields are computed alternately until a consistent solution is obtained. The cooling is then calculated. From each finished model the actual observable emission is also computed,

$$E = \int n_U A_{UL} h\nu P_e \, dh. \qquad (11)$$

It is expected that $E \sim Q$, but the distribution of dE and dQ differ since $\rho \sim P_e$ only at depth (where most of the cooling occurs) (Athay, 1972b).

Although not included in the cooling, the H9 (3835 Å) emission is calculated for the finished models with the same methods, for comparison with observations (Section 5.3). For this line, the two level approximation may not be as accurate. The net emission in the Balmer and Paschen continua is also determined for the models (Section 5.4). The He I line emission from the models is given by LaBonte (1978).

One other important contributor to cooling by hydrogen, especially at low temperatures, is H^- continuum emission (Brown, 1973). Using the form suggested by Osterbrock (1961) with the cross-section from Allen (1963),

$$dQ(H^-) = 4\sigma \; T^3(T-T_{min}) \; p_e \; (1-X) \; n_H \; 8x10^{-26} \left(\frac{5000}{T}\right)^3 \qquad (12)$$

with σ the Stefan-Boltzmann constant, T_{min} the photospheric boundary temperature, p_e the electron pressure.

2.3.2 Metals

Metals cool the high temperature part of the flare. At the transition zone between the flare chromosphere and corona, the optical depth in all chromospheric transitions is clearly zero. The region just below this level has the lowest densities, highest temperatures and temperature gradients of the flare chromosphere, thus distributing its small total mass over several ionizations stages, and maintaining low optical depth. In contrast, the lower layers of the flare chromosphere with high densities, low temperatures and temperature gradients, have all their mass in the neutral atoms, whose lines are optically deep. A single correction factor applied to the optically thin emission must thus be $\simeq\rho$ at depth but $\simeq 1$ at the surface. P_e meets these requirements. Our relation for the metals cooling is

$$dQ(\text{metals}) = dE \; (\tau=0) \; P_e(\tau_{metals}) \qquad (13)$$

with the thin emission from Cox and Tucker (1969), approximately

$$dE(\tau=0) = 4.4 \times 10^{-36} \; T^{2.9} \; n_e^2 \; ; \quad T \lesssim 7.6 \times 10^4 K. \qquad (14)$$

The correction for optical depth is most important at low temperatures, and the value of τ_{metals} should apply to the species which contribute to the cooling at those temperatures; principally O I and C I. Since these atoms have first excitation and ionization potentials nearly equal those of hydrogen, we use

$$\tau_{metals} = A_{metals} \; \tau_{Lyman\ \alpha} \qquad (15)$$

with $A_{metals} = 10^{-3}$ the relative abundance by number.

Equations (13) and (15) represent the main effects of optical depth. One factor not allowed for is the increase in n_U above its optically thin value due to scattering, so the cooling by metals may be underestimated. This issue will be discussed in Section 4.2.2.

2.3.3 Explosion Level

Equation (14) is valid up to 76 000 K; from 76 000 to ≈260 000 K, dE is nearly constant, and above 260 000 K, decreases with temperature (Cox and Tucker, 1969). Thus for T≳300 000 K, the atmosphere is thermally unstable, and heats to coronal temperatures. With the cooling rate constant between 76 000 and 260 000 K, the lower temperature can be taken as the onset of instability, with no increase in cooling available to match increased heating. This is an

upper limit to the temperature of the part of the flare in radiative equilibrium. Higher parts of the atmosphere "explode" or free expand into the corona (Lin and Hudson, 1976).

By equating the maximum cooling rate with the electron heating, a value for the column density at the explosion level can be found, and thus $\mathcal{E}_x$, the lowest energy electron which participates in the radiatively stable flare. This in turn gives the total energy flux in the radiative flare,

$$F_{rad} = F_{20} \left(\frac{\mathcal{E}_x}{20} \right)^{1-\gamma} \tag{16}$$

If the number density n is exponentially decreasing with height, as in an isothermal hydrostatic gas, and nearly so in the model atmosphere, then

$$F_{rad} \propto F_{20}^{\left(\gamma \frac{4}{\gamma+3}\right)} \quad . \tag{17}$$

While F_{20} changes by 10^3, F_{rad} changes by only ≈50 (for $\gamma=4$).

Because the cooling rate is constant between 76 000 and 260 000 K, the material is indifferent to exactly what its temperature is within that range. At the top of the radiatively stable flare, all temperatures between 1 and 3×10^5 K should be equally represented.

2.4 Solution Procedure

Equilibrium is assumed, so at each height the sum of radiative cooling losses due to HI, H^- and metals (L) must equal the sum of heating gains due to electrons and nonflare processes (G). With the total density fixed and the ionization determined simultaneously with the cooling, only the temperature distribution needs to be adjusted to obtain a solution.

An iterative scheme is used. The flare explosion level is found and an initial guess made at the temperature distribution using that point as a boundary condition. The heating and cooling for that distribution are computed, and the temperature distribution changed to make the ratio of heating to cooling closer to 1. The magnitude of the temperature correction at each step is found from the quantity $(G-L)(dL/dT)^{-1}$, with dL/dT the change in cooling rate per change in temperature between two successive temperature distributions. (Only the cooling is used because the heating is insensitive to temperature.) Each temperature distribution is smoothed to remove unphysical spikes or local inversions. Numerical tests show this procedure is convergent and stable. In the final models, the heating and cooling are equal within 5% at each point, on average.

3. MODEL RESULTS

This section presents the numerical results of the calculations. As we have noted, strict consistency of the results and the physical assumptions is not guaranteed in advance, because of the numerical nature of the computation. Questions of validity are discussed in Section 4.

3.1 Temperature

Figure 1a,b,c shows the temperature profiles for the γ=3, 4, 5 models, respectively. Curves are labeled by the value of $\log(F_{20})$. The initial quiet model is labeled Q.

Obviously, for larger F_{20} the heating of the chromosphere extends deeper. For example, in the γ=4 models, as F_{20} increases from 10^{8} to 10^{11}, the explosion level moves inward from a density $\simeq 3\times10^{11}$ to $\simeq 3\times10^{12}$ cm^{-3}. The minimum electron energy penetrating to this level, ε_x, increases from 9 to 24 keV, and the total energy flux dumped into the radiative region below the explosion level increases from $\simeq 10^{9}$ ($F_{rad} \simeq 10\ F_{20}$) to $\simeq 5\times10^{10}$ ($F_{rad} \simeq \frac{1}{2}F_{20}$). Since the values of ε_x are within the observed range of the hard X-ray power law spectrum, no significant extrapolation of that spectrum to lower energies is needed to produce the radiative flare.

Another expected result is that the temperature gradient varies directly with γ. For a given value of F_{20}, a high γ

beam has a larger fraction of low energy electrons, which heat near the surface; a low γ beam has a larger fraction of high energy electrons, which heat at depth. Near 500 km, the γ=3 models have temperatures nearly those of γ=5 models with 100 times larger F_{20}. The more intense γ=3 beams appear capable of penetrating below the temperature into the photosphere; this is not in fact correct (Section 4.1).

The only notable structure to the temperature profiles is the appearance of a bump (temperature excess) near 1000 km and 15 000 K, in the models with large F_{20}. The bump, when present, is the region where the cooling changes from metals dominated to hydrogen dominated. Its size and presence depends strongly on the value of the metals cooling. The bump is a response of the models to the weak dependence of the hydrogen losses on F_{20} (Section 3.5).

3.2 Energy Balance

Figure 2a,b shows the energy balance for the central models of our grid (γ=4, $F_{20} = 10^9, 10^{10}$). These illustrate the features seen in all the models. Note that the 10^{10} model has a temperature bump, while the 10^9 does not.

As expected, metals cool the highest, hottest part of the flare, T$\geq$14 - 20 000 K over all models. Hydrogen lines cool the middle part, and H^- the lowest, coolest part. More interesting is the result that in the region cooled by hydrogen lines, Hα dominates. Lyα cooling peaks higher, in

the region controlled by metals.

The thickness of the layer cooled by the hydrogen lines varies inversely with F_{20}. It is $\gtrsim$500 km at $F_{20} = 10^{8}$, but $\lesssim$100 km at $F_{20} = 10^{11}$. The difference is provided by the metals cooling extending to greater depth, and the rapid increase in H^- emission. In addition, Hα and Lyα are saturated, in the sense that their volume cooling dQ varies little, around 10 ergs $cm^{-3}s^{-1}$. The H^- and metals cooling show much larger ranges. This saturation produces the bump in the temperature profiles, as higher temperatures are needed to maintain the cooling at depth.

The total contribution of hydrogen to the flare cooling is small. The ratio of Q(metals)/Q(H) ranges from $\simeq$10 at $F_{20} = 10^{8}$ to $\simeq$30 at $F_{20} = 10^{11}$. Essentially all the energy output is in metals emission. This is a response to the exponential form of the energy input. Fully half of the total flux F_{rad} is dumped in the top 50 to 100 km of the radiative flare, where it is balanced by emission at temperatures of 50 to 76 000 K (up to 300 000 K).

3.3 Electron Density

Figure 3a,b,c shows the electron density distribution for the γ=3, 4, 5 models, respectively. In each case, total ionization extends down to some depth, below which the electron density drops off rapidly. The peak value of n_e

increases with F_{20}. At a given F_{20}, a high γ model has a lower peak n_e and a steeper drop off than a low γ model. The maximum values of n_e range from $3x10^{12}$ to $\simeq 1x10^{14}$ cm^{-3}, but have validity problems (Section 4.1).

3.4 Hydrogen Level 2 Density

Figure 4 shows the hydrogen level n=2 density distribution. The height of peak n=2 density coincides with that of the peak n_e. As such, it shares the validity problems of n_e.

The peak n_2 density is 1 to 300 km below the maximum Hα volume cooling, and 2 to 500 km below the Lyα maximum; the larger separations occur at larger F_{20}. Column integral values of n_2 range from $3x10^{14}$ to $3x10^{16}$ cm^{-2} (Hα optical depths $\simeq 10^2$ to 10^4). Halfwidth of the n_2 density ranges from 75 to $\simeq$200 km, being thinner for larger F_{20}.

3.5 Self-Consistent Emission

Tabel 1 gives the H^-, Hα and Lyα emission (ergs $cm^{-2}s^{-1}$) for the models. As these radiations were computed self-consistently with the models, they should be accurate if the assumptions are valid.

Although necessary for the energy balance, the H^- emission is negligible. The contrast of the H^- continuum is $\lesssim$1% in the visible, even for the strongest models. Even this small emission is probably not present, however

(Section 4.1).

The line emission is concentrated near $\tau=1$, even though the cooling is deeper; the photons diffuse to the surface to escape. We only consider the total line emission because the line profiles for this type of static model are strongly self-reversed (Canfield, 1974a). However, macroscopic turbulent velocities only a factor of 2 to 3 larger than the model thermal velocities would smooth out the profiles into better agreement with observations. This extra broadening would alter the line optical depth scales, but not greatly affect the computed cooling; $\tau \propto v^{-1}$, while the line cooling is typically spread over a range of 100 in τ.

Hα emission only increases by a factor of 5 between the $F_{20} = 10^{8}$ and 10^{11} models, and is independent of γ. The Hα equivalent width ranges from 5 to 25 $\mathring{A}$ of the nearby continuum. The Lyα to Hα energy ratio varies from $\simeq$1 in the 10^{8} models to $\simeq$2 in the 10^{11} models. Because neither Hα nor Lyα vary greatly among the models, they might also be insensitive to changes in the model physics; for example, order of magnitude changes in the metals cooling. This has been shown in numerical tests.

3.6 Other Emission

Table 2 gives the H9 (3835 $\mathring{A}$), Balmer continuum, and Paschen continuum emissions, computed from the final models.

The calculations of these transitions were not included in the model cooling, as they were assumed to emit much less than Hα or Lyα.

H9, unlike Hα, varies greatly in response to F_{20}. The H9 emission increases by ≃400 as F_{20} goes from 10^8 to 10^{11}. There is also a strong γ dependence, with H9 emission 10 times larger at γ=3 than γ=5, at fixed F_{20}. The H9 emission is much less than Hα in the weak models, but nearly equal in the strong models. The optical depth ranges from 0.7 to 70 with F_{20}; since τ<1 in the weak models, the emission computed is possibly in error.

As with H9, the Balmer and Paschen continua emissions vary strongly with F_{20} and γ. In the weak models each continuum emits less than Hα, but in the strong models, emits much more; the Balmer continuum emission in the strongest models nearly equals the total energy flux F_{rad}. However, the recombination continua are emitted at the electron density maximum, and vary as n_e^2. They are thus very sensitive to the problems with the maximum electron density (Section 4.1).

The He I 584 Å, 10830 Å and 5876 Å (D_3) emission from a set of these models has been computed by LaBonte (1978). Those transitions do not affect the results described in this study. Like H9, the helium lines are very sensitive to F_{20}.

4. SELF-CONSISTENCY

In this section we test the model results for consistency with the initial assumptions.

4.1 Heating

At depth in the atmosphere, the energy flux deposited by the electron beam is too small to heat the atmosphere to the computed equilibrium state in the short duration of the flares. Brown (1973) assumed the equilibration time to be $t_T = nkt/G_F$, the time to heat the gas to the equilibrium temperature, but this is not correct in these models. A much stronger limit is the time required to ionize the gas, $t_I = n_e R_H/G_F$, R_H a Rydberg. Because the models are fully ionized to fairly low temperatures, $\simeq 10^4$K, $n_e R_H > nkT$ from near the explosion level to below the electron density maximum. This constraint sets a stronger limit on the depth of flare heating than either the requirement of temperature equilibrium or the effect of a high energy cutoff in the electron beam spectrum.

For the models, t_I is largest at the electron density maximum, (n_e^{max}), and varies between 40 and 120 seconds. These times are much larger than the 10 s characteristic time of the events. However,

$$t_I \propto N^{-\left(\frac{\gamma+1}{2}\right)} \propto n^{-\left(\frac{\gamma+1}{2}\right)},$$

and the condition $t_I \lesssim 10$ s is achieved by moving to a density a factor of 2 or 3 lower than n_e^{max}, at about 100 km higher altitude. This suggests the flare models (temperature and density profiles) should be truncated at about 100 km above the computed n_e^{max}.

The effect on the emitted radiation of removing the lowest part of the models varies for the different transitions. Lyα and Hα will be only slightly affected since they are produced well above n_e^{max}. Even H9 may only be altered by a factor of 2 or 3. The continua are greatly changed. H^- is produced entirely below n_e^{max}, and would be effectively reduced to zero. The recombination continua, being proportional to n_e^2, would decrease by about an order of magnitude; this is an improvement from the standpoint of consistency, given the large computed values.

For all higher altitudes in the radiative flare, the energy input is sufficient to heat and ionize the chromosphere to the computed equilibrium. Above the explosion level, the product of heating and flare duration will set the temperature, with radiative cooling negligible.

4.2 Cooling

4.2.1 Atomic Equilibrium

For the radiative equilibrium to be actually achieved, the ionization fraction and level populations must

reach the equilibrium values in the flare duration. This requires all important atomic rates to be $>(10\ s)^{-1}$. In general the slowest rates, which control the equilibration time, are the first excitation rate, $C_{12} \propto n_e \exp(-h\nu/kT)$ (e.g., Lyα collisional excitation) and radiative recombination, $R_k \propto n_e z^2 T^{-\frac{1}{2}}$.

For the hydrogen system, the time constraint is met by all models in the region of Hα and Lyα cooling. At depth both C_{12} and R_k are reduced below the limit by the decreasing electron density and temperature. In the weak models, R_k also fails at altitude, because of the decreasing density; a reduction in the neutral fraction, thus optical depth, is indicated at high temperature in the weak models. C_{12} remains above the limit at altitude as the temperature dependence outweighs the density decrease.

The metals (in all ionization stages) have C_{12} about equal to hydrogen, and should also meet the equilibrium condition. In addition, the charge dependence of R_k implies that the higher ionization stages, important to high temperature cooling, will also equilibrate.

4.2.2 Optical Depth Correction for Metals

The approximation used to correct for the optical depth of the metal lines can be tested by applying the same procedure to hydrogen and comparing with the properly

computed results. For this test we compare the peak value of the Lyα cooling, at T = 20 to 30 000 K, with the values predicted using first, the optically thin formula only, and second, the optically thin value corrected by P_e(Lyα). Subordinate lines contribute little to the hydrogen cooling at this temperature.

The result of this test is that our corrected form is better than the uncorrected optically thin form. The optically thin case predicts emission which is 25 to 200 times larger than the exact result; the error increases with F_{20}. The corrected form predicts emission 5 to 40 times smaller than the exact result; the error decreases with increasing F_{20}. The worst corrected case is nearly as good as the best thin case. However, while the corrected form is a useful order of magnitude estimator, it is clear that a more exact calculation of the metals must be done in any improved model.

4.2.3 Balmer Decrement

In computing the models it was assumed that the cooling due to atomic hydrogen was dominated by the leading lines Lyα and Hα. In the weak models this is a good approximation, but the subsequent calculation of the H9 line and the recombination continua shows this is incorrect in the strong models. (Brown's [1973] models were similar to our weak models, therefore Canfield [1974a] found Hα and Lyα dominant.)

Even allowing for the reduction in emission suggested in Section 4.2.1, the continua contribute more than the lines. Further, the H9 values suggest a small Balmer decrement, with many lines comparable in intensity to Hα. (The H9 calculation may itself be incorrect, if the two level approximation fails; the upper level can decay through other transitions with lower optical depth, and is more closely coupled to the continuum than the lower levels.) In the strong models, the hydrogen cooling may be underestimated by an order of magnitude. More cooling would give lower temperatures and ionization than the computed models.

The onset of much higher cooling at large energy fluxes would in effect produce a saturation of the atmosphere. Beyond some critical energy flux, perhaps $F_{20} \gtrsim 10^{10}$, only small increases in temperature and ionization would be needed to greatly increase the cooling and balance the flare heating. The already weak dependence of the Hα and Lyα emission on F_{20} would be further reduced, while the higher excitation lines would be very sensitive to large values of F_{20}.

4.3 Atmospheric Stability

The chromospheric density distribution was assumed not to relax to a new hydrostatic form consistent with the flare temperatures in the flare duration. In the models this is true. The absolute value of the pressure gradient

$\lesssim$3 times the preflare hydrostatic gradient. Mass accelerations are thus $\lesssim$3 times gravity, with velocities and displacements negligible in 10 s ($\lesssim$8 km s^{-1}, $\lesssim$14 km).

A more serious problem occurs at the flare explosion level. The temperature of the gas just above that point increases continually, because the electron heating exceeds the radiative cooling. In 10 s, temperatures of 1 to 4×10^7K are reached ($dT \simeq dt\ G_F/2nk$). With the density continuous through this level but the temperature discontinuous, a pressure jump of order 100 is formed, generating a shock wave. Of course, the shock actually forms in a few seconds, with an initially lower amplitude.

An instability at this level is unavoidable, because the heating is independent of temperature while the radiative cooling is a decreasing function of temperature. For hydrostatic equilibrium the 10^7K material should be 100 times less dense than the 10^5K gas, but for radiative balance against the heating, the 10^7K gas must be $\simeq$10 times more dense than the 10^5K gas (Cox and Tucker, 1969). These conditions cannot be met simultaneously. Once the temperature rises above 10^5K, further heating is unchecked, leading to pressure instability. The instability is not resolved in a finite time, and gas motions must continue as long as the electron heating. The idea that a long-lived electron heated flare can be considered relaxed (Brown, 1973) is

wrong; indeed, the hydrodynamic effects should be larger, having time to fully develop. Other types of long-lived flare heating which are temperature sensitive, for example conduction, apparently do permit static solutions (Moore and Fung, 1972; Shmeleva and Syrovatskii, 1973).

The shock moving into the chromosphere is compressive, with the density behind $\gtrsim 4$ times the ambient. Once the density of the 10^7K gas is 10 times its initial value, radiation can balance the heating. Therefore, when the shock penetrates only a factor $\lesssim 2.5$ in density, about 200 km, the heating is balanced and the temperature stabilized. Further penetration (density increase) would lower the temperature, and since the cooling coefficient at all temperatures from $10^4 < T < 10^7$K is larger than that at 10^7K, the gas would cool catastrophically toward the lower temperature, with a time scale of a few seconds. Some residual of the shock would certainly continue deeper, in the form of bulk motions, turbulence, or perhaps heating. An interesting alternative model to ours would be one in which the chromosphere is not heated directly by the electron beam, but indirectly by the shocks it produces; the large energy fluxes dumped at the top being convected downward in shocks.

One further problem is that the rate of temperature increase varies as $N^{-\left(\frac{\gamma+1}{2}\right)}$,

thus rapidly increasing with height as long as the power law electron spectrum continues to lower energies. These hotter layers will dump more energy into gas motions. The extent of the chromospheric disruption will thus depend on the low energy electron spectrum. Until direct measurements are made, this will remain a fundamental uncertainty in the models.

5. COMPARISON WITH OBSERVATIONS

Although the models are inconsistent at the top and bottom, in the middle layers where the hydrogen line emission is produced they may be valid. It is of interest to compare the model predictions with observations as a further test of validity. One problem is the limited data on rapid flashes, or even the normal flash phase of flares; comparison in some cases may not be appropriate. Generally, data are available only for large flares, therefore certain properties cannot be accurately tested, for example, the weak dependence of Hα and Lyα emission on F_{20}.

5.1 Lyα to Hα Ratio

The Lyα to Hα energy ratio is predicted to be 1 to 2. Zirin (1978) has pointed out that this ratio is of order 1 in flares, although the data are sparse. Because this ratio

varies so little in the models, it is conceivable that it can be shown analytically to reduce to a combination of atomic constants; we have not been able to do so.

5.2 Hα

The Hα equivalent widths predicted, 5 to 25 Å are too large by a factor of 2 or 3. The largest observed flash phase equivalent widths are 10 to 15 Å (Svestka, 1976). In small events, widths or order 1 or 2 Å are indicated (Zirin, 1977). The Hα optical depths (and integral values of n_2) are in the range of observed flares, but will be reduced by the various model problems by a factor of 2 or 3.

5.3 H9

The predicted H9 emission may also be too large. The H9 emission in the August 4, 1972 1840 UT and 2140 UT events was $\simeq 6 \times 10^7$ and $1 - 2 \times 10^7$ ergs $cm^{-2} s^{-1}$ respectively (Zirin and Tanaka, 1973); the emitting areas $\simeq 2 \times 10^{17}$ and 5×10^{17} cm^2. The observed X-ray emission, converted to thick target electrons, implied $E_{20} = 5.4 \times 10^{28}$ and 1.4×10^{28} ergs s^{-1}, with $\gamma = 2.8$ and 2.5 (Lin and Hudson, 1976). If the electron flux is assumed to be confined to the H9 emission area, then $F_{20} = 2.7 \times 10^{11}$ and 2.8×10^{10} ergs $cm^{-2} s^{-1}$ are required. Using the $\gamma = 3$ models, the predicted H9 emission is 3×10^8 and 1×10^8 ergs $cm^{-2} s^{-1}$, much larger than observed.

However, it is clear that some of the nonthermal flux must be heating the much larger total flare area. For example, the Hα kernel alone has an area 25 times that of the H9 flashes in the 1840 UT flare. Given the high sensitivity of H9 to F_{20}, an alternate assumption could be made, that nearly all the nonthermal electrons are dumped outside the H9 area. The H9 area would then have F_{20} enhanced by only a factor of perhaps 3 above the flare average, rather than orders of magnitude. This would bring the predicted emission down closer to the observed values.

5.4 Continuum

The continuum emissions are strongly affected by the disequilibrium in the lower part of the models. (Note that with the factor of 2 or 3 reduction needed to correct this problem, the maximum electron densities in the models are in the observed range; Svestka [1976]). Considering this problem, the H^- continuum should be absent, and the hydrogen recombination continua emissions $\lesssim 0.1$ the values in Table 2. The recombination continua are emitted at a temperature of 15 000 K. The Paschen continuum should be nearly flat, with only $\simeq$15% decrease in energy flux per Å between the Paschen and Balmer limits, and the Balmer jump about a factor of 16 in the same units.

The continuum emission in the August 7, 1972 1520 UT flare had two components: a group of knots, and a wave

(Machado and Rust, 1974; Rust and Hegwer, 1975). In the knots, emission at 4950 Å was 3 - 6×10^6 ergs cm^{-2} s^{-1} $Å^{-1}$, and a factor of 2 to 4 less at 5900 Å (brighter knots were bluer). In the wave, emission was 1.5×10^6 ergs cm^{-2} s^{-1} $Å^{-1}$ at 4950 and 5900 Å; between 4300 and 3700 Å there was a factor of 2 increase in intensity; and a Balmer jump of $\lesssim 2.5 \times 10^6$ ergs cm^{-2} s^{-1} $Å^{-1}$ was possible but not positively indicated. Areas were 6×10^{17} and 2×10^{17} cm^2. If all the X-rays were thick target and all the nonthermal electrons dumped in the continuum emission areas, then $F_{20} = 3.7 \times 10^{11}$ and 1.1×10^{11} ergs cm^{-2} s^{-1}, with $\gamma = 2.3$ (Lin and Hudson, 1976). Using the $\gamma=3$ models, Paschen emission of $\lesssim 5 \times 10^5$ and $\lesssim 1.6 \times 10^5$ ergs $cm^{-2} s^{-1} Å^{-1}$ is predicted. The Balmer jump in the wave would be $\lesssim 2 \times 10^6$ ergs $cm^{-2} s^{-1} Å^{-1}$.

These results show that most or all of the observed continuum must be produced by some process other than hydrogen recombination. The predicted recombination spectrum is too faint and red. The knots are even bluer than an H^- continuum, which would have the additional problem of being unable to rapidly vary in intensity (Rust and Hegwer, 1975), due to the long time needed to heat the layers emitting H^-.

5.5 Metals

All the models predict that the ratio of metals

emission at $\simeq 10^5$ K to hydrogen emission is 10, even (or, especially) considering hydrodynamic disruption. Many of the important lines at 10^5 K are in the wavelength range 300 to 1400 Å (Moore, 1976), so a comparison of Lyα to the other lines in this region should give a rough measure of the metals to hydrogen ratio. Older data on large flares (Hall and Hinteregger, 1969; Donnelly and Hall, 1973), with low time resolution and no spatial resolution, showed this ratio to be $\simeq 1$, with Lyα about equal to the sum of the metals emission. However, the data presented by Emslie and Noyes (1978) show that in small (5"), rapid (lifetimes 20 - 60 s) flash flares, several metal lines each equal to Lyα emission (see also Noyes et al., 1975). Thus the ratio of metals to hydrogen is $\gtrsim 4$, and considering the other metal lines not measured, the ratio could be $\gtrsim 10$, as predicted.

6. SUMMARY

We have attempted to model flares with rapid intensity fluctuation. The model balances nonthermal electron heating with thermal radiative cooling in a hydrostatic chromosphere.

The computed models show the initial assumptions are not correct throughout. The actual flare chromosphere cannot be static at high altitude (insufficient cooling) and does not reach thermal equilibrium at depth (insufficient heating). The middle layers, approximately where the

hydrogen emission is produced, may be valid, though. The timings and emissions in the middle layers are close enough to the required values that an equilibrium region cannot be ruled out, given the model simplicity.

A time dependent calculation is needed to prove the existence and extent of an equilibrium layer. Both the atmospheric structure and atomic equilibrium (ionization and excitation) must be time-variable. This calculation would also indicate whether the chromospheric heating is actually provided directly by the electron beam as assumed, or by the downward mixing of hot material by shocks.

Model-insensitive parameters such as the Lyα/Hα and metals/hydrogen emission ratios are correctly predicted. The Balmer lines Hα and H9 are brighter than observed; they would be reduced in a more exact model to give better agreement. Nonthermal line emission appears unnecessary in this type of flare. The predicted continuum emission is less than the observed, and the difference in spectral shapes suggests other emission processes produce the observed continuum.

In any improved model the radiative cooling should be computed more accurately. The assumption that Lyα and Hα dominate the hydrogen cooling is true only in weak models; other lines and continua contribute in the strong models. The metals emission for each species should be computed by the same technique used for hydrogen, rather than using

approximate forms.

The necessary improvements in the model will introduce great complexity. A more productive next step therefore may be to improve the observational data on rapid flash flares, which is currently quite limited. Such rapid flares are reasonably frequent; of 50 He I D_3 events observed at Big Bear Solar Observatory in 1974 and 1975, 3 showed emission areas evolving in times $\lesssim$10 s. A serious observing program would set exact standards for future models. Some questions would remain unanswered; spatially resolved hard X-ray spectra are needed to determine the actual intensity and distribution of thick target electrons in flares.

We thank R. Moore for useful discussions, and R. Canfield for other discussions on radiative cooling.

This research was supported by NASA under grant NASA NGR 05 002 034 and NSF under grant ATM76-21132.

REFERENCES

Allen, C.W.: 1963, Astrophysical Quantities, Athlone Press, London.

Athay, R.G.: 1972a, Ap.J. 176, 659.

Athay, R.G.: 1972b, Radiation Transport in Spectral Lines, Reidel Publishing Co., Dordrecht, Holland.

Beckers, J.M.: 1972, Ann. Rev. Ay. Ap., 10, 73.

Bessey, R.J. and Kuperus, M.: 1970, Solar Phys. 12, 216.

Brown, J.C.: 1973, Solar Phys. 31, 143.

Canfield, R.C.: 1974a, Solar Phys., 34, 339.

Canfield, R.C.: 1974b, Ap.J. 194, 483.

Canfield, R.C.: 1974c, AFCRL-TR-74-0158, Env. Res. Paper No. 47.

Cox, D.P. and Tucker, W.H.: 1969, Ap.J. 157, 1157.

Datlowe, D.W.: 1974, in Solar γ-, X- and EUV Radiation, S.R. Kane (ed.), IAU Symp. 68, Reidel Publishing Co., Dordrecht, Holland.

Donnelly, R.F.: 1971, Solar Phys., 20, 188.

Donnelly, R.F., and Hall, L.A.: 1973, Solar Phys. 31, 411.

Emslie, A.G. and Noyes, R.W.: 1978, Center for Astrophys. preprint 897.

Frost, K.J. and Dennis, B.R.: 1971, Ap.J., 165, 655.

Hall, L.A. and Hinteregger, H.E.: 1969, in Solar Flares and Space Research, C. de Jager and Z. Svestka (eds.), COSPAR 11, 81, Reidel Publishing Co., Dordrecht, Holland.

Heasley, J.N., Mihalas, D. and Poland, A.I.: 1974, Ap. J. 192, 181.

Heyvaerts, J., Priest, E.R. and Rust, D.M.: 1977, Ap.J. 216, 123.

Hudson, H.S.: 1972, Solar Phys. 24, 414.

Kahler, S.W.: 1977, Ap.J. 214, 891.

Kahler, S.W. and Kreplin, R.W.: 1971, Ap.J. 168, 531.

Kane, S.R. and Anderson, K.A.: 1970, Ap.J. 162, 1003.

Knight, J. and Sturrock, P.A.: 1977, Ap.J. 218, 306.

Kulander, J.L.: 1976, Solar Phys. 48, 287.

LaBonte, B.J.: 1978, Big Bear Solar Obs. Preprint #0170.

Lin, R.P. and Hudson, H.S.: 1976, Solar Phys. 50, 153.

Machado, M.E. and Rust, D.M.: 1974, Solar Phys. 38, 499.

Moore, R.L.: 1976, Big Bear Solar Obs. Preprint #0158.

Moore, R.L. and Fung, P.C.W.: 1972, Solar Phys. 23, 78.

Noyes, R.W., Foukal, P.V., Huber, M.C.E., Reeves, E.M., Schmahl, E.J., Timothy, J.G., Vernazza, J.E. and Withbroe, G.L.: 1975, in Solar γ-, X- and EUV Radiation, S.R. Kane (ed.), IAU Symp. 68, Reidel Publishing Co., Dordrecht, Holland.

Osterbrock, D.E.: 1961, Ap.J. 134, 437.

Peterson, L.E., Datlowe, D.W. and McKenzie, D.L.: 1973 in High Energy Phenomena on the Sun, R. Ramaty and R.C. Stone (eds.), NASA SP342, 132.

Rust, D.M. and Hegwer, F.: 1975, Solar Phys. 40, 141.

Sheeley, N.R., Bohlin, J.D., Brueckner, G.E., Purcell, J.D., Scherrer, V.E., Tousey, R., Smith J.B., Speich, D.M., Tandberg-Hanssen, E., Wilson, R.M., DeLoach, A.C., Hoover, R.B., and McGuire, J.P.: 1975, Solar Phys. 45, 377.

Shmeleva, O.P. and Syrovatskii, S.I.: 1973, Solar Phys. 33, 341.

Sturrock, P.A.: 1968, in Structure and Development of Solar Active Regions, K.O. Kiepenheuer (ed.), IAU Symp. 35, 471, Reidel Publishing Co., Dordrecht, Holland.

Svestka, Z.: 1976, Solar Flares, Reidel Publishing Co., Dordrecht, Holland.

Syrovatskii, S.I. and Shmeleva, O.P.: 1972, Sov.A.J. 16, 273.

Van Beek, H.F., Hoyng, P. and Stevens, G.A.: 1973, in Collected Data Reports on August 1972 Solar Terrestrial Events, World Data Center A, Report UAG 28, Part II, 319.

Vernazza, J.E., Avrett, E.H. and Loeser, R.: 1973, Ap.J. 184, 605.

Vorpahl, J.A.: 1972, Solar Phys. 26, 397.

Zirin, H.: 1973, Vistas in Astron. 16, 1.

Zirin, H.: 1977, Big Bear Solar Obs. Preprint # 0165.

Zirin, H.: 1978, Big Bear Solar Obs. Preprint # 0172.

Zirin, H. and Tanaka, K.: 1973, Solar Phys. 32, 173.

Table 1

EMISSIONS INCLUDED IN COOLING

	Lyα			Hα			H^-		
F_{20}	γ = 3	4	5	3	4	5	3	4	5
10^8	4.4_7	5.1_7	5.6_7	4.5_7	4.4_7	4.2_7	3.4_6	1.7_6	1.2_6
10^9	1.3_8	1.3_8	1.2_8	1.1_8	9.8_7	8.7_7	2.5_7	8.2_6	4.2_6
10^{10}	2.9_8	2.6_8	2.4_8	1.8_8	1.6_8	1.4_8	1.7_8	4.5_7	1.8_7
10^{11}	6.3_8	4.9_8	4.0_8	2.7_8	2.3_8	2.1_8	7.9_8	2.1_8	7.9_7

All quantities are in ergs cm^{-2} s^{-1}.

$2_8 \equiv 2 \times 10^8$.

Table 2

EMISSIONS COMPUTED FROM FINAL MODELS

	H9			Paschen Continuum			Balmer Continuum		
F_{20}	$\gamma = 3$	4	5	3	4	5	3	4	5
10^8	2.8_5	2.4_5	2.0_5	9_6	6_6	4_6	3_7	2_7	1.4_7
10^9	3.9_6	1.0_6	6.3_5	2_8	6_7	3_7	7_8	2_8	1_8
10^{10}	7.2_7	1.2_7	4.2_6	2_9	6_8	2.4_8	6_9	2_9	8_8
10^{11}	2.0_8	9.6_7	2.5_7	9_9	6_9	9_8	3_{10}	2_{10}	3_9

All quantities are in ergs cm^{-2} s^{-1}.

$2_8 \equiv 2 \times 10^8$.

FIGURE CAPTIONS

Figure 1

Temperature profiles of the flare models. The initial quiet chromosphere is labeled Q. The flares are labeled with $\log(F_{20})$, F_{20} the energy flux in non-thermal electrons >20 keV. Height is measured from $\tau_{5000\ \mathring{A}} = 1$ in the continuum. Parts a, b, c of the figure give the models for γ=3, 4, 5 respectively, with γ the power law index of the hard X-ray spectrum emitted by the flare.

Figure 2

Energy balance for representative flare models. The energy input (ergs $cm^{-3}s^{-1}$) by the nonthermal electrons is balanced at each point by the thermal radiation cooling by metals, H^- continuum, and the Hα and Lyα lines of hydrogen.

(a) $F_{20}=10^9$ ergs $cm^{-3}s^{-1}$, γ=4

(b) $F_{20}=10^{10}$ ergs $cm^{-3}s^{-1}$, γ=4.

Figure 3

Electron density profiles of the flare models. Curves are labeled as in Figure 1. The flares are totally ionized above the electron density maximum. Parts a, b, c are for γ=3, 4, 5 respectively.

Figure 4

Hydrogen level n=2 density profiles of the flare models. Curves are labeled as in Figure 1. The n_2 maxima coincide with those of n_e. Parts a, b, c are for γ=3, 4, 5 respectively.

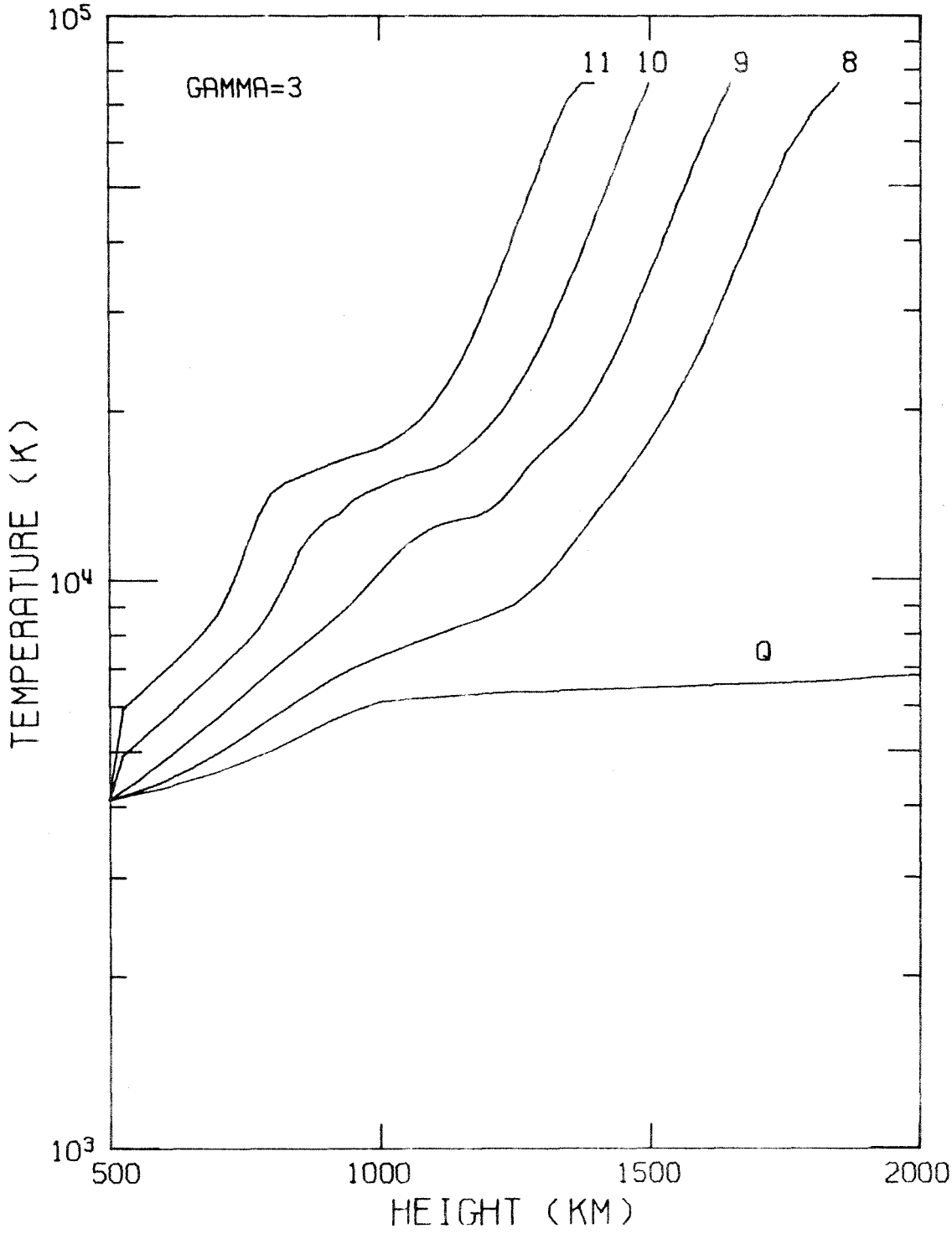
GAMMA=3
11
10
9
8
Q
TEMPERATURE (K)
HEIGHT (KM)
10^5
10^4
10^3
500
1000
1500
2000

Figure 1a

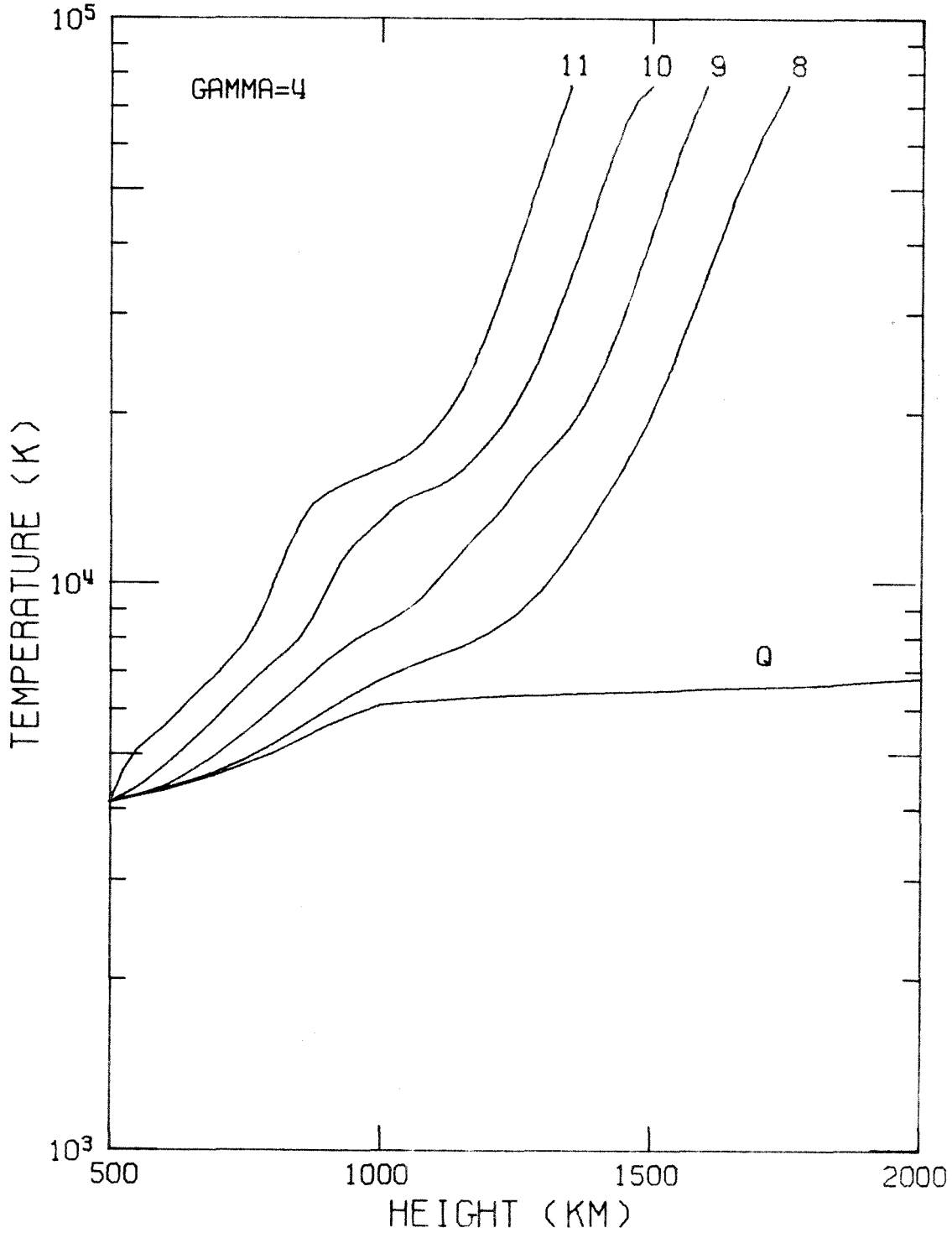
10^5
10^4
10^3
GAMMA=4
11
10
9
8
Q
TEMPERATURE (K)
500
1000
1500
2000
HEIGHT (KM)

Figure 1b

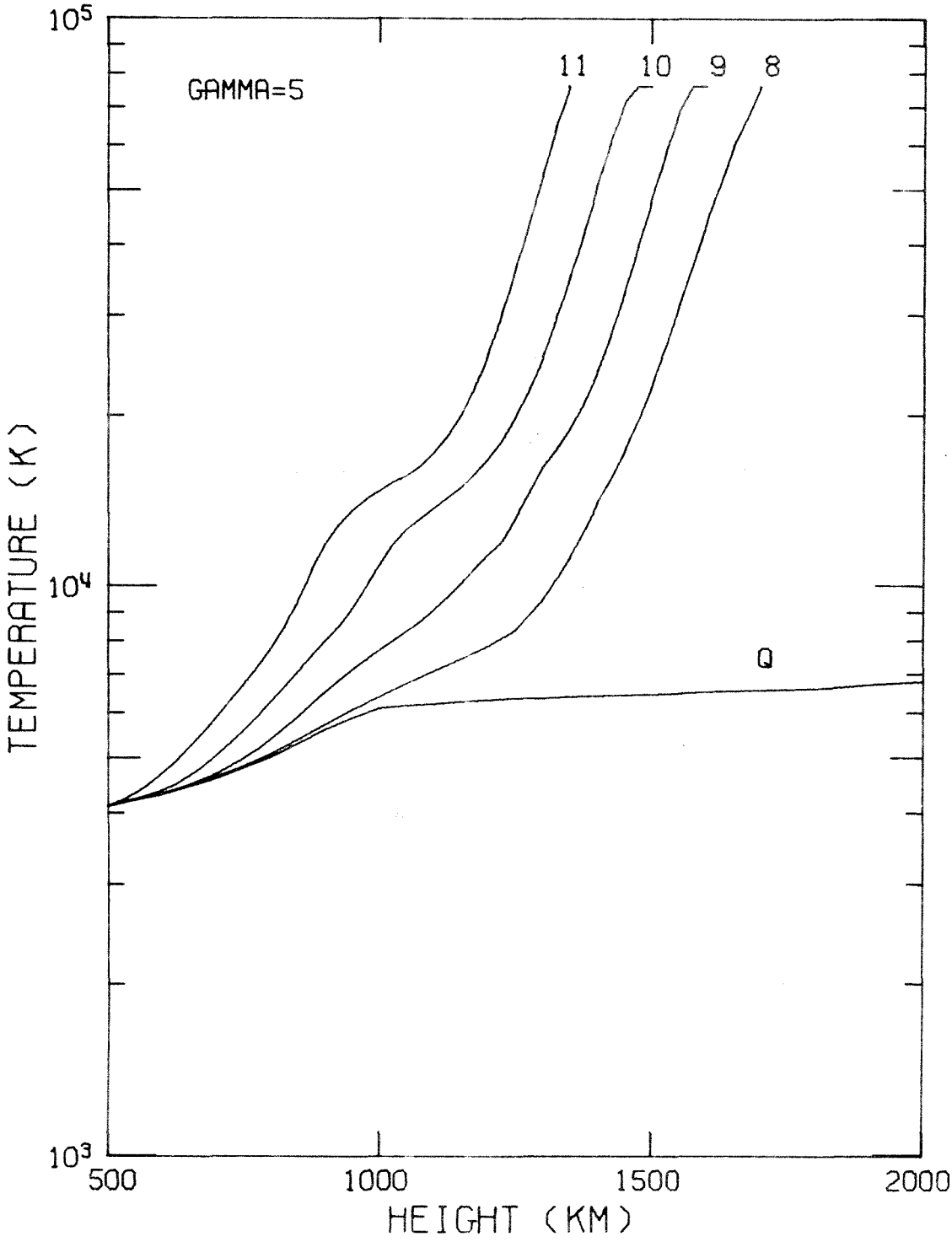
GAMMA=5
11
10
9
8
Q
TEMPERATURE (K)
10^5
10^4
10^3
500
1000
1500
2000
HEIGHT (KM)

Figure 1c

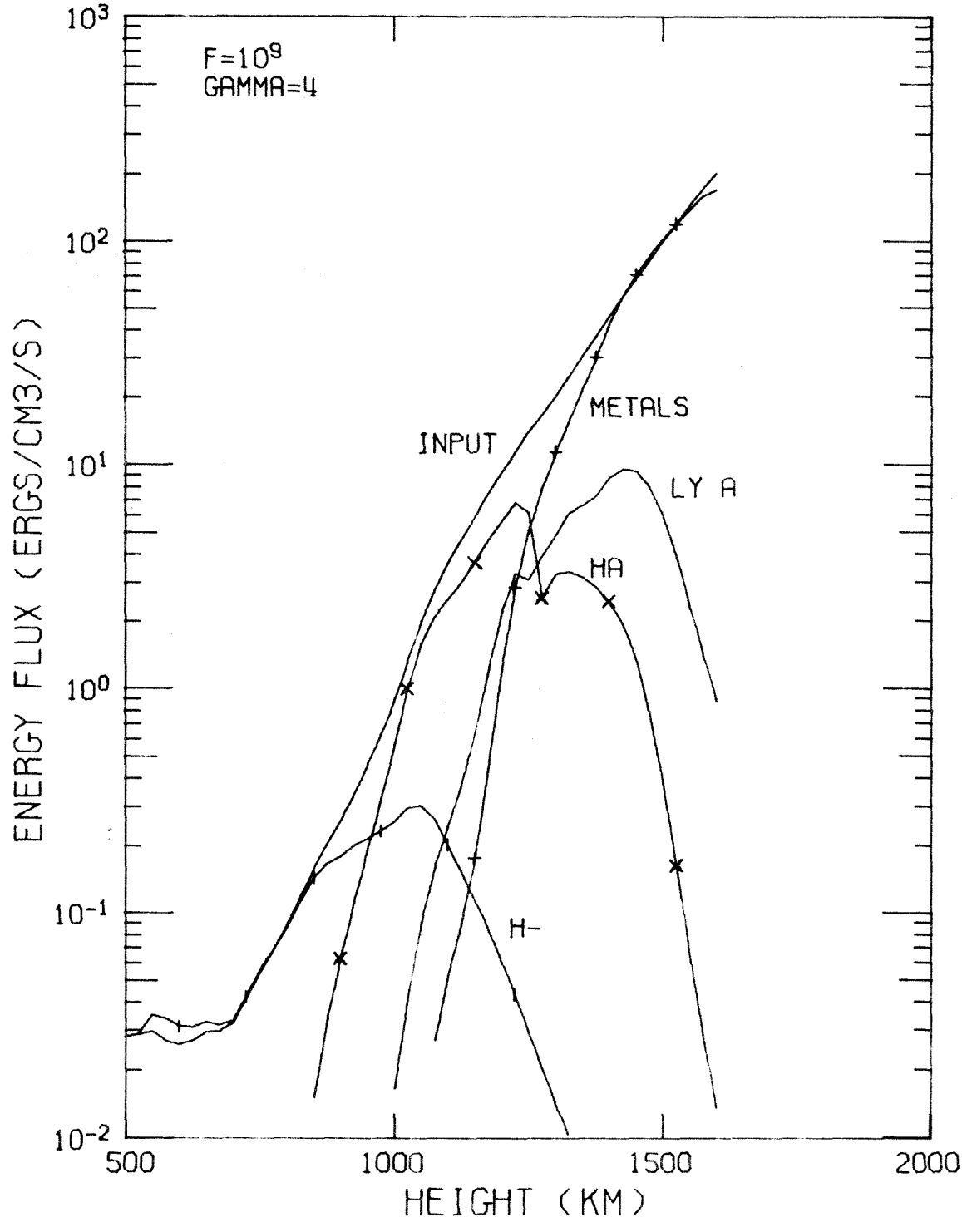
F=10^9
GAMMA=4
INPUT
METALS
LY A
HA
H-
ENERGY FLUX (ERGS/CM3/S)
HEIGHT (KM)
10^3
10^2
10^1
10^0
10^-1
10^-2
500
1000
1500
2000

Figure 2a

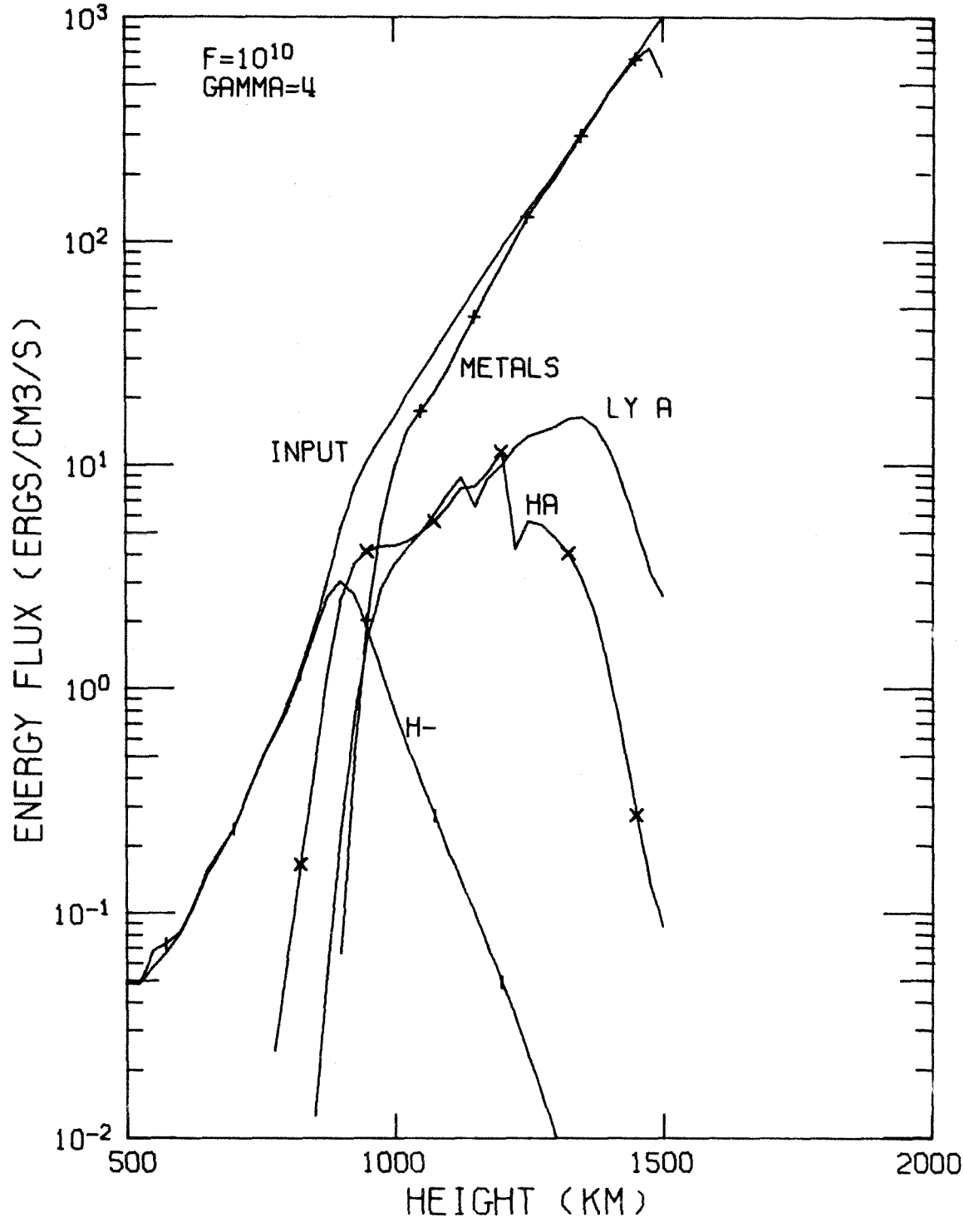
F=10^10
GAMMA=4
METALS
LY A
INPUT
HA
H-
ENERGY FLUX (ERGS/CM3/S)
HEIGHT (KM)
10^3
10^2
10^1
10^0
10^-1
10^-2
500
1000
1500
2000

Figure 2b

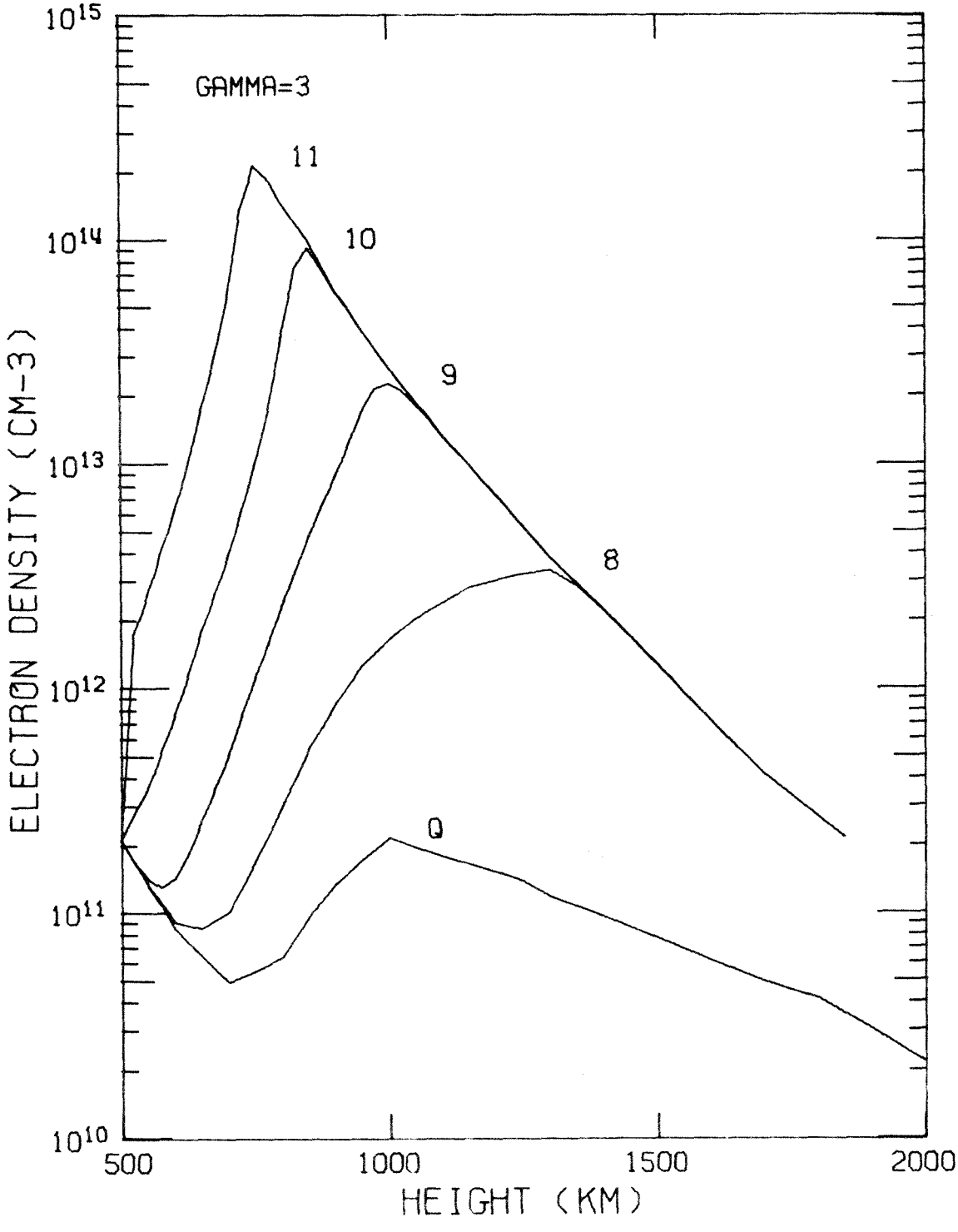
GAMMA=3
11
10
9
8
Q
ELECTRON DENSITY (CM-3)
HEIGHT (KM)
10^15
10^14
10^13
10^12
10^11
10^10
500
1000
1500
2000

Figure 3a

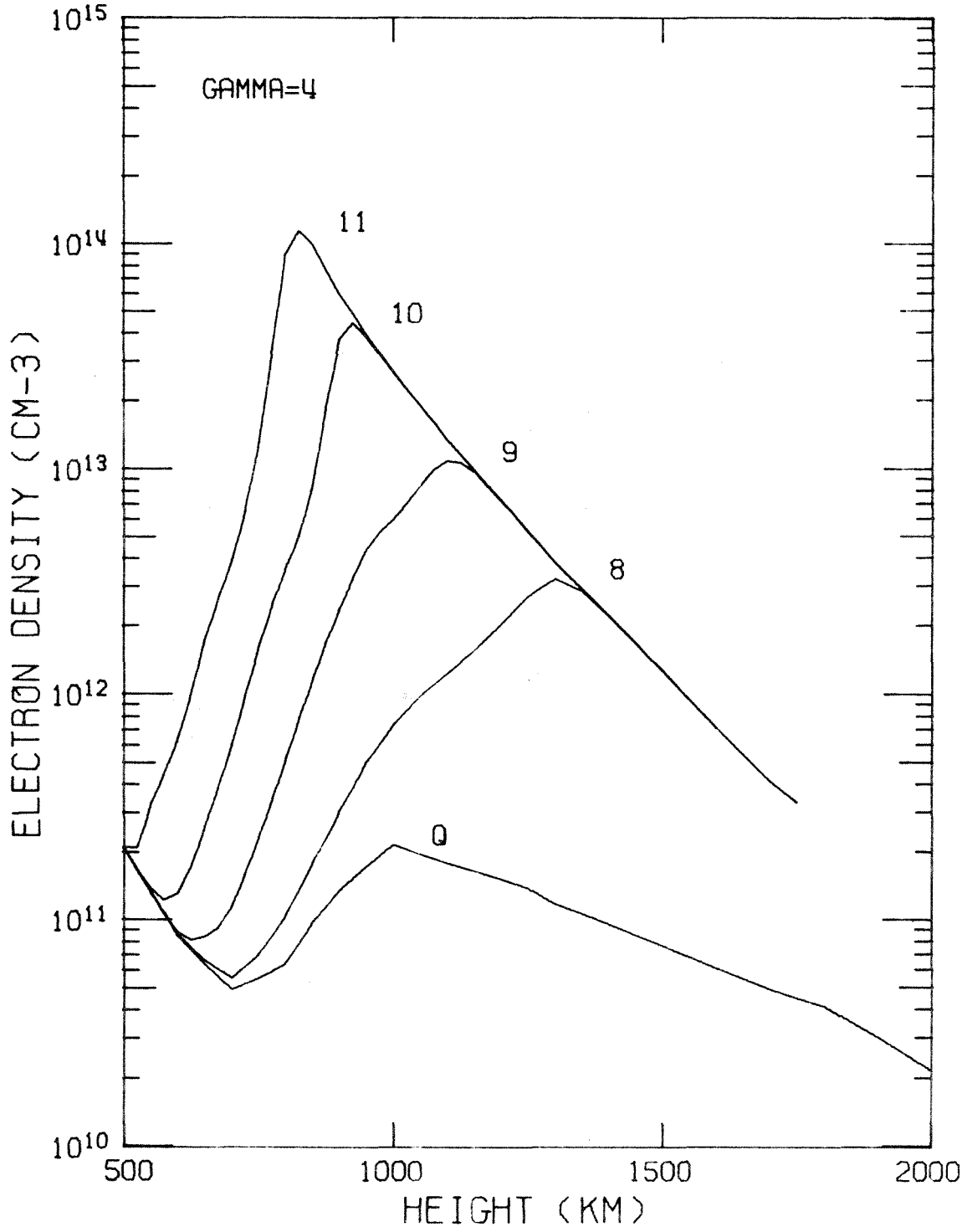
GAMMA=4
11
10
9
8
Q
ELECTRON DENSITY (CM-3)
HEIGHT (KM)
10^15
10^14
10^13
10^12
10^11
10^10
500
1000
1500
2000

Figure 3b

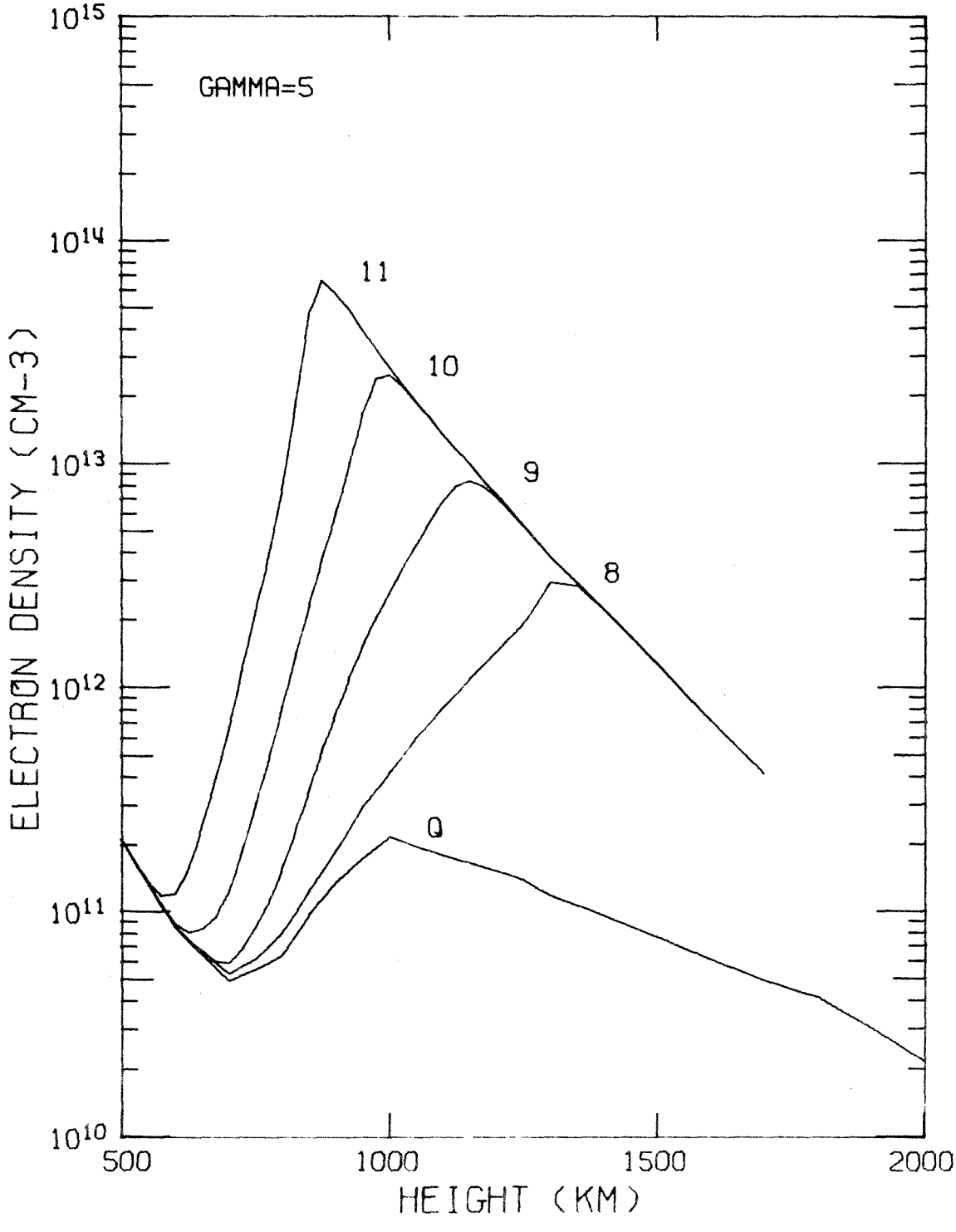
GAMMA=5
11
10
9
8
0
ELECTRON DENSITY (CM-3)
HEIGHT (KM)
10^{15}
10^{14}
10^{13}
10^{12}
10^{11}
10^{10}
500
1000
1500
2000

Figure 3c

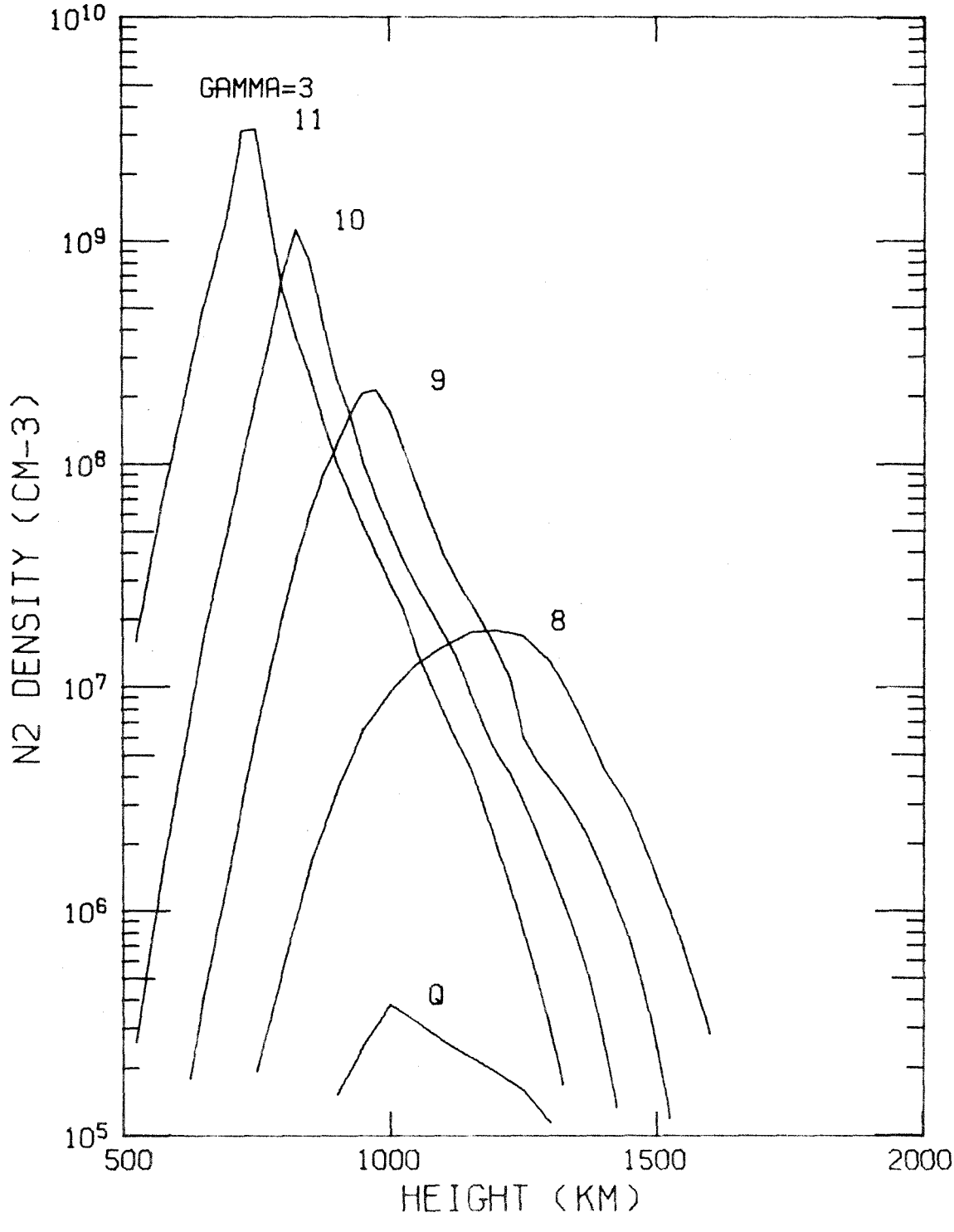
GAMMA=3
11
10
9
8
Q
N2 DENSITY (CM-3)
HEIGHT (KM)
10^10
10^9
10^8
10^7
10^6
10^5
500
1000
1500
2000

Figure 4a

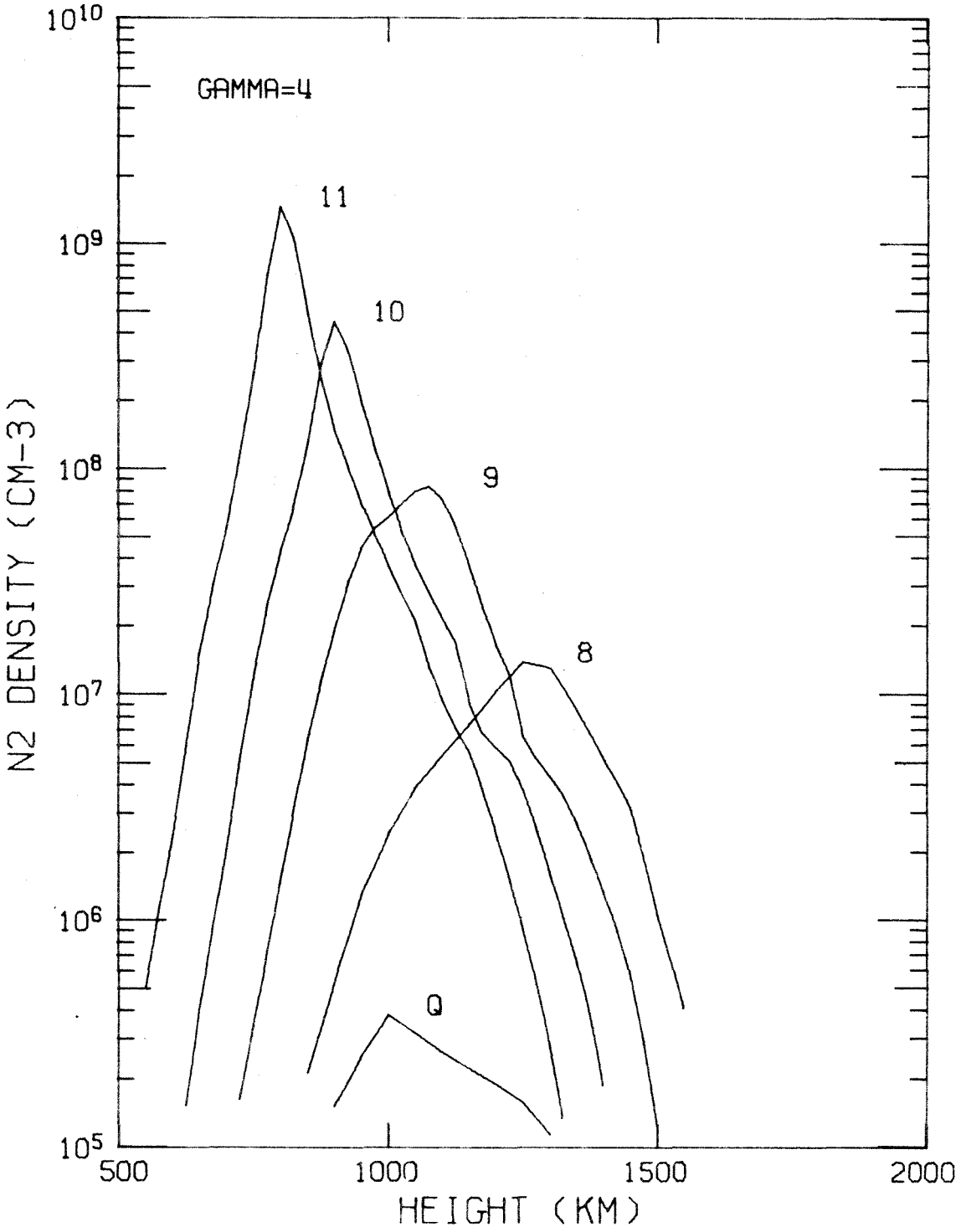
GAMMA=4
11
10
9
8
Q
N2 DENSITY (CM-3)
HEIGHT (KM)
10^10
10^9
10^8
10^7
10^6
10^5
500
1000
1500
2000

Figure 4b

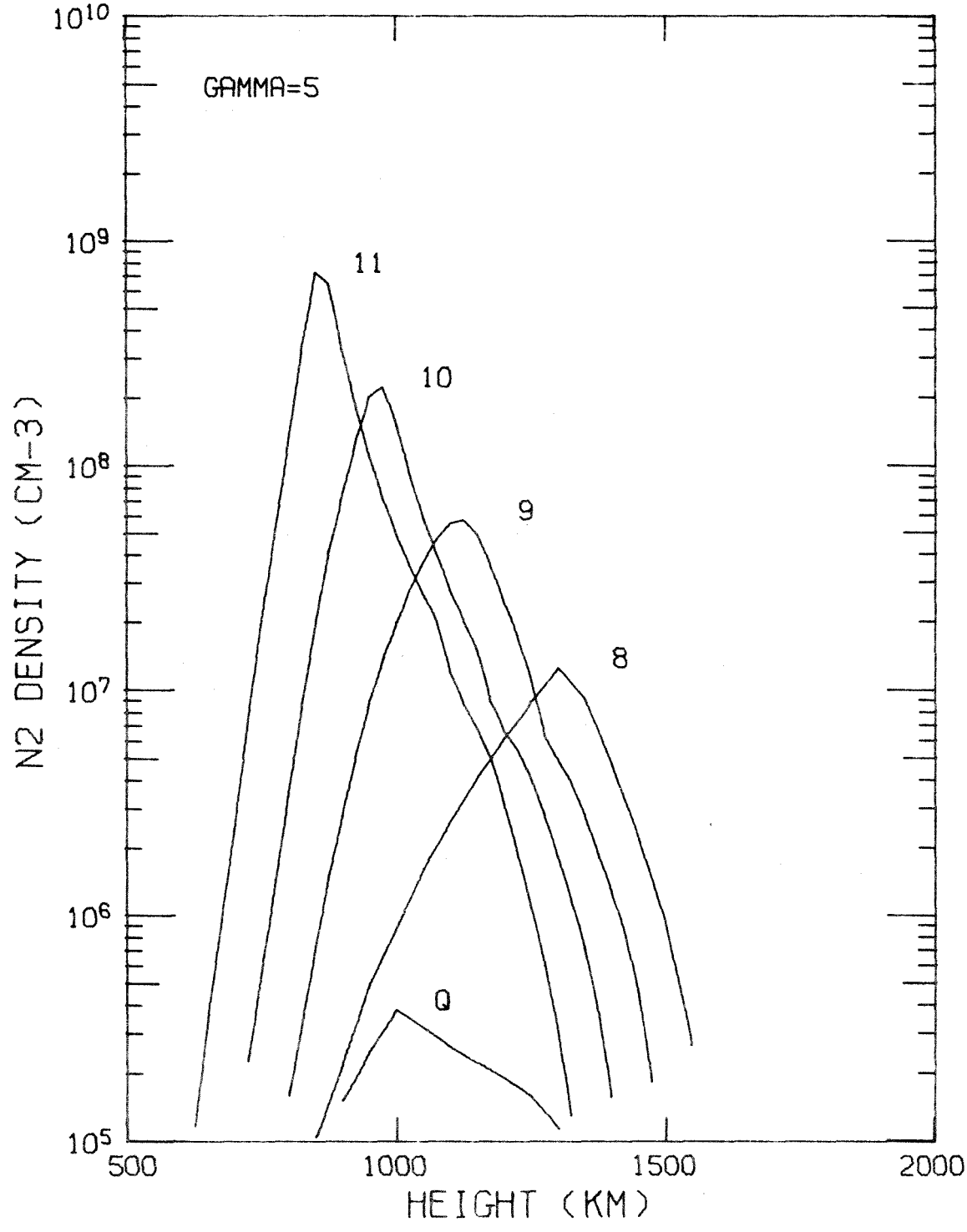
GAMMA=5
11
10
9
8
Q
N2 DENSITY (CM-3)
HEIGHT (KM)
10^10
10^9
10^8
10^7
10^6
10^5
500
1000
1500
2000

Figure 4c